EXPERIMENTAL INVESTIGATIONS OF SHOCK WAVES UNDERGOING
SUDDEN EXPANSION IN A CONFINED CHAMBER

By

GREGG LAWRENCE ABATE

A DISSERTATION PRESENTED TO THE GRADUATE SCHOOL
OF THE UNIVERSITY OF FLORIDA IN PARTIAL FULFILLMENT
OF THE REQUIREMENTS FOR THE DEGREE OF
DOCTOR OF PHILOSOPHY

UNIVERSITY OF FLORIDA

1999

For my family

TABLE OF CONTENTS

LIST OF FIGURES

LIST OF TABLES

EXPERIMENTAL INVESTIGATIONS OF SHOCK WAVES UNDERGOING
SUDDEN EXPANSION IN A CONFINED CHAMBER

By

GREGG LAWRENCE ABATE

December 1999

Chairman: Dr. Wei Shyy
Major Department: Aerospace Engineering, Mechanics and Engineering Science

An experimental apparatus has been designed and constructed to study the
evolution of shock waves undergoing a sudden expansion while in a confined chamber.
Time-accurate flowfield visualization data in the form of a circular cut-off Schlieren
imagery of the shock waves undergoing the sudden area expansion in air have been
gathered and studied at Mach numbers of 1.5, 2.0, and 3.0. The information was
collected from a square shock tube with sudden expansion in one direction. Detailed,
time-accurate measurements of the shock wave and vortex core location are presented as
well as wall pressure data. In addition, a study of the evolving flow structure through the
time-accurate flowfield imagery is also presented. The results of these experiments are
compared to previous computational fluid dynamics data of shock waves exiting both a
circular opening and a rectangular opening. Two-dimensional numerical simulations
specific to the Mach 1.5 and 2.0 initial conditions and geometry are compared to the

experimental data as well. The direct comparisons of the current work and previous numerical efforts provide insight into differences between sudden two-dimensional and three-dimensional shock wave expansions. The data gathered from this effort further elucidates key modeling questions by providing time-accurate flow visualization and pressure data of a shock wave undergoing a sudden expansion in a confined chamber.

CHAPTER 1
INTRODUCTION AND LITERATURE REVIEW

The interaction of shock waves with vortices is one of the fundamental topics in shock wave dynamics. This problem has been studied in the past in connection with aerodynamic noise generation in high-speed turbulent flows. Better understanding of this fluid dynamic phenomenon is essential since the mechanism is closely linked with the randomization of turbulent flows and the dissipation of the mean flow kinetic energy. Shock waves and their interaction with vortical flows play an important role in compressible turbulence. The nonlinearities and strong interactions between these two dissipative structures pose further complications. Experimental studies carried out with state-of-the-art diagnostic tools are capable of increasing the fundamental understanding of the fluid dynamic mechanisms at work. Ideally, experimental studies should be designed and closely linked with numerical studies so that results will help elucidate key fundamental fluid dynamic questions.

The sudden area expansion of a shock wave within a confined domain is composed of many interesting fluid dynamic phenomena. These include shock wave reflections, vorticity production, shock-vortex interaction, energy exchange between shock and turbulence, and shock focusing (Chang and Kim, 1995). These phenomena are highly transient and occur at time scales ranging from microseconds to milliseconds. Accurate prediction and modeling of these phenomena is important for design applications. This thesis presents a focused look at sudden shock wave expansion within

a confined chamber and the interaction of that shock wave with other fluid dynamic features.

1.1 Background

A useful tool in the study of turbulent mixing, compressibility, and chemical kinetics is the shock tube. Shock tubes have become standard tools for studying chemical kinetics at high temperatures (Williams, 1985, Gaydon and Hurle, 1963, and Bradley, 1962). The shock tube is a device in which a plane shock wave is produced by the sudden expansion of a high pressure gas into a low pressure gas. A simple form of a shock tube is shown in Figure 1.1a. Here the low pressure side (p_1), known as the driven gas, is shown on the right and the high pressure reservoir (p_4), known as the driver gas, is shown on the left.

The high and low pressure gases are separated by a diaphragm which bursts at time t_o. A compression wave is formed in the low pressure section which rapidly forms into a shock wave. At the same time an expansion wave travels into the high pressure section. This expansion wave is sometimes referred to as an expansion fan where the pressure falls smoothly as opposed to the shock where the pressure rise is sudden. Figure 1.1b shows an x-t diagram for this process. For a particular time, t_1, shown by a dashed line in Figure 1.1b, we show the pressure and temperature distributions in the tube in Figures 1.1c and 1.1d respectively.

The shock tube is a valuable tool in the study of physical and chemical gas processes at high temperature since the experimental gas is brought almost instantly to a known and controlled pressure, p_2, and temperature, T_2, immediately behind the shock.

The experimental gas is then held at this steady temperature and pressure for a few hundred microseconds and then suddenly cooled. It is now possible to study the experimental gas with optical or other diagnostic means as it is being swept past a viewing window.
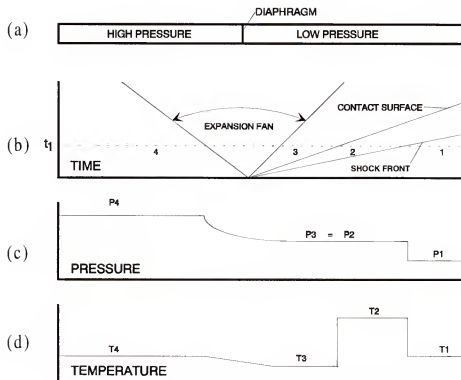
Figure 1.1 Diagram of simple shock tube operation

The use of a shock tube in the study of high temperature gas reactions is advantageous since the heating of the gas occurs rapidly (much less than a microsecond). There are also no wall effects so that the fundamental processes can be studied at selected temperatures and conditions without interference or without reactions occurring at intermediate temperatures. Very high temperatures can also be obtained in a shock tube whereas it is seldom possible to go above 1500K in conventional experiments.

Detonations are formed by the pressure pulse from the expanding gas that, in turn, serves to propagate the detonation. In a number of experiments the shock tube has been used to study the initiation and propagation of detonations (Teodorczyk et al., 1989, Liu et al., 1986, Jones et al., 1995, and Oran et al., 1993). Spontaneous ignition of gas mixtures occurs at various temperatures after finite induction periods. With shock tube ignition (shock induced combustion) it is possible to study ignition with much shorter induction periods.

As seen, the shock tube offers great possibilities in the study of high temperature chemical research. The most severe limitation is the short flow times which are on the order of only a few hundred microseconds.

The derivation of shock tube relations (i.e., the equations that relate the gas on one side of the moving shock to the other) are straightforward (Anderson, 1990, Gaydon and Hurle, 1963, and Bradley, 1962) and will not be derived here. Presented here are, however, the relations that describe the flow properties in a shock tube for ideal gases based on initial conditions. We will see that one can tailor the conditions for the experiment with the proper selection of initial conditions.

The most important relation is the pressure ratio across the shock (p_2/p_1) to the pressure ratio on the driver and driven gases (p_4/p_1) and is given by the following (Anderson, 1990):

$$\frac{p_4}{p_1} = \frac{p_2}{p_1}\left\{1 - \frac{(\gamma_4 - 1)(a_1/a_4)(p_2/p_1 - 1)}{\sqrt{2\gamma_1[2\gamma_1 + (\gamma_1 + 1)(p_2/p_1 - 1)]}}\right\}^{-2\gamma_4/(\gamma_4 - 1)} . \qquad (1.1)$$

Here γ is the ratio of specific heats, a is the speed of sound, subscript "1" quantities refer to the driven gas, subscript "4" quantities refer to the driver gas, and subscript "2" quantities refer to the gas immediately behind the shock.

Note here that the pressure ratio across the shock is given as a function of the initial conditions (p_1, p_4, T_1, and T_4) and physical properties (γ_1 and γ_4) of the gases. Note that the speed of sound is given by $a^2 = \gamma RT$ (where R is the specific gas constant). Due to the complexity of this equation, the easiest method to solve it is to specify the initial conditions and iterate values of p_2/p_1 until the correct value of p_4/p_1 is found.

Once the pressure ratio across the shock is found, the conditions behind the shock are found via normal shock relations as follows (Anderson, 1990):

The Mach number of the shock is given by

$$M_s = \sqrt{\frac{\gamma+1}{2\gamma}\left(\frac{p_2}{p_1}-1\right)+1}. \tag{1.2}$$

The temperature ratio across the shock is given by

$$\frac{T_2}{T_1} = \frac{p_2}{p_1}\left(\frac{\dfrac{\gamma+1}{\gamma-1}+\dfrac{p_2}{p_1}}{1+\dfrac{\gamma+1}{\gamma-1}\dfrac{p_2}{p_1}}\right) \tag{1.3}$$

The density ratio across the shock is given by

$$\frac{\rho_2}{\rho_1} = \frac{1+\dfrac{\gamma+1}{\gamma-1}\left(\dfrac{p_2}{p_1}\right)}{\dfrac{\gamma+1}{\gamma-1}+\dfrac{p_2}{p_1}}. \tag{1.4}$$

The velocity induced upon the fluid behind the shock is given by

$$u_p = \frac{a_1}{\gamma}\left(\frac{p_2}{p_1} - 1\right)\left(\frac{\dfrac{2\gamma}{\gamma+1}}{\dfrac{\gamma-1}{\gamma+1} + \dfrac{p_2}{p_1}}\right)^{\!\!1/2}. \tag{1.5}$$

Note that for equations 1.2-1.5, γ is that of the driven gas (i.e., γ_1).

The shock strength that is attainable within a shock tube is given via equation 1.1. Bradley (1962) states that the optimum conditions for producing strong shocks entail using the lowest possible molecular weight and γ-value for the driver gas and as high a molecular weight as is practical for the experimental gas. The value of γ_1 will have little effect since all γ-values for gases lie in the range 1.0-1.67. Therefore, the most suitable driver gases are hydrogen and helium, of which the latter is to be preferred if burning at the interface is liable to interfere with the observations.

For most practical applications, the maximum shock strength attainable is about Mach 7 for helium driver gas and nitrogen as the test gas. Keep in mind this is for an ideal gas where effects of dissociation and ionization are neglected. Heating the driver gas can also increase the shock strength.

Additional tailoring of the shock in the tube is possible through the use of multiple diaphragms and area variations. In practice, a single diaphragm will not always burst at exactly the same pressure. This can be a problem in detailed experiments. Instead, a double diaphragm is used so that each diaphragm bursts at about half the working pressure ($p_4 - p_1$). Changes in area after the diaphragm have burst can increase the strength of the shock by about 50% (Bradley, 1962).

1.2 Literature Reviews

A major interest in the present phase of research is the interaction between turbulence and compressibility in flowfields subjected to mixing limitations. State-of-the-art numerical models are currently being applied to fluid dynamic problems in these areas. These involve experimental data to support such models similar to data that will be produced in this research. Experiments will be conducted with inert gases to investigate the turbulent/mixing/compressibility phenomena of a sudden shock wave expansion.

Although the shock tube is ideally suited for investigations of chemical processes induced in the fluid by the shock wave, the shock tube can offer tremendous insight into inert fluid dynamic structure as well.

1.2.1 Shock Waves Undergoing Sudden Area Expansion

The gas dynamic phenomenon associated with a sudden area expansion consists of highly transient or "unsteady" flow and diffraction that gives rise to turbulent/compressible/vortical flow. If the initial flow undergoing the expansion is supersonic and is preceded by a shock wave, additional phenomena such as diffraction and reflection of the shock as well as blast jet formation will occur. Should the expansion region be confined, that is the sudden area expansion is finite, mutual interaction of all the aforementioned phenomena can occur. These interactions can occur at time scales ranging from micoseconds to milliseconds.

Recent investigations of this type of gas dynamic flow, given by Jiang et al. (1997), present experimental and numerical simulations of a circular shock tube

generated flow undergoing a sudden expansion. Figure 1.2 highlights the salient flow features of such a sudden expansion. Here it is seen that as the initial shock wave travels down the shock tube (Figure 1.2a) it will undergo a sudden area expansion into a confined area (Figure 1.2b-d), the flowfield gives rise to two important features. First, there is a "starting jet" which is characterized by the formation of a vortex ring, Mach disk, and shear layer. Second, this precursor shock reflects off the confining walls of the expansion chamber and interacts with the starting jet flowfield. It is clearly seen in Figure 1.2 that this reflected shock splits once it interacts with the primary vortex ring which gives rise to secondary shock waves.

a) Incident shock approaching sudden area change

b) Initial expansion of shock wave and formation of vortices

c) reflection of shock wave off confining wall

d) Interaction of reflected shock wave with vortex
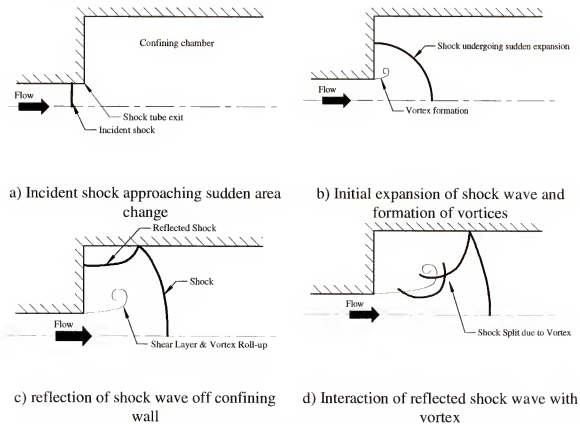
Figure 1.2 Schematic of shock/vortex/shear layer interaction during sudden expansion of a shock wave in a confined chamber

This shock/vortex/shear layer interaction is also shown in Figure 1.2. Here the reflected shock splits when it interacts with the primary vortex ring. It was also observed by Jiang et al. (1997) that once the reflected shock wave passes through the developing shear layer that the shear layer splits, is moved into the jet flow, and is convected downstream. This allows another shear layer to form from the jet exit forming another weaker vortex ring. This is referred to as shear layer splitting and is largely an inviscid phenomenon.

Another phenomenon noted by Jiang et al. (1997) is the shock/shear layer interactions. It is noted that a vortex ring in the shear layer induced a shock wave and the shock wave separated the vortex ring from the shear layer. This is most often noted in strongly expanded free jets.

Much of the recent work in area expansion flows has been done numerically. This is easily understood since computing power has increased through the years and, perhaps more importantly, flow visualization is achieved much more easily from numerical results (Yates, 1992).

Chang and Kim (1995) present numerical results for shock tube simulations coupled with an area expansion. Here, the Euler equations for a circular shock tube undergoing a sudden expansion are modeled for Mach numbers of 1.5 and 2.0. This paper points out that although blast flow fields generated by an open ended shock tube are fairly well understood, there are relatively few reports concerning the flow fields generated in a tube of sudden expansion. Chang and Kim (1995) indicate that it is clear that the complex transient flow structures associated with the blast waves and its jet require careful treatment of the physical discontinuities and sharp gradients.

The results of this work indicate that the flow structure is very much influenced by the incident shock strength. When the shock is ejected into an expansion tube, the flow structure becomes much more complicated due to the nonlinear interaction of the many flow elements confined in a limited flow passage. They are the blast wave in transmission, its reflected shocks, barrel shock, jet shock, embedded shocklets, slipstream, and isolated vortex rings creating strongly rotational flow environment. There have been few papers dealing with shock wave in the expansion tube associated with blast simulators and no paper has shown the detailed time dependent flow structures affected by the tube wall (Chang and Kim, 1995). Chang and Kim (1995) present some excellent time dependent results of the pressure and density fields for this flowfield but lack any experimental data to help substantiate.

1.2.2 Key Flow Field Aspects

A shock wave traveling down a one-dimensional tube and then undergoing a sudden area change (i.e., a confined sudden expansion) gives rise to many interesting flow features. As was diagrammed in Figure 1.2, the essential elements of this occurrence involve the reflection of the shock wave off the confining chamber and its subsequent interaction with the evolving flowfield. A key feature involves the interaction of the reflected shock with the vortex roll-up due to the flow emanating from the sudden area change (i.e., from the starting jet). This formation of the vortex ring and subsequent interaction with the reflected shock wave were also shown in Figure 1.2.

1.2.2.1 Viscous Dissipation

Direct numerical simulations of compressible flowfields by Sarkar et al. (1991) and Zeman (1990) it was concluded that the effects of compressibility on turbulent

structure was dissipate. Compressibility introduces an extra amount of dissipation due to turbulent fluctuations which is due to the non-divergent nature of the velocity fluctuations. This can be seen by examining the rate of dissipation of turbulent kinetic energy (TKE) which is given as

$$\rho \varepsilon = \overline{\frac{\partial u_i''}{\partial x_j} \sigma_{ij}''} \tag{1.6}$$

where the overbar represents Reynolds average and the ($''$) represents a Favre averaged quantity (see e.g., Shyy et al., 1998). The fluctuating component of the viscous stresses is defined as

$$\overline{\sigma_{ij}''} = 2\mu \overline{s_{ij}} + \lambda \overline{u_{k,k}''} \delta_{ij}; \qquad s_{ij} = \frac{1}{2}\left(\overline{u_{i,j}''} + \overline{u_{j,i}''}\right) \tag{1.7}$$

where μ is the molecular viscosity, λ is the bulk viscosity, the comma denotes derivative, and δ_{ij} is the Kronecker delta. Assuming the fluctuations in molecular viscosity are negligible, equation 1.6 becomes

$$\rho \varepsilon = 2\mu \left(\overline{s_{ij} s_{ij}}\right) - \frac{2}{3}\mu \left(\overline{u_{k,k}'' u_{k,k}''}\right) \tag{1.8}$$

The dilatation of the velocity fluctuations is defined as

$$d'' = \frac{\partial u_k''}{\partial x_k} \tag{1.9}$$

and the fluctuating vorticity vector is defined as

$$\omega_p'' = \left(u_{i,j}'' - u_{j,i}''\right) \tag{1.10}$$

For homogeneous turbulent flows, equations 1.9 and 1.10 can de combined with equation 1.8 to yield

$$\rho\varepsilon = \mu\left(\overline{\omega_p'' \omega_p''} - \frac{4}{3}\overline{d'' d''}\right) \tag{1.11}$$

for the dissipation rate of TKE in turbulent compressible flows (Shyy et al., 1998). This equation represents the sum of a "solenoidal" dissipation rate (the first term on the right side of equation 1.11) and a "dilatational dissipation" rate (the second term).

For incompressible flows, energy cascade to the viscous dissipation scale is via the mechanism of vortex-vortex interaction and is represented in the first term of equation 1.11 (Lee, 1997). The solenoidal dissipation mechanism is associated with incompressible flows since the velocity divergence of the second term of equation 1.11 vanishes. The second term in equation 1.11 is associated with the velocity divergence and is referred to as the "dilatational dissipation" term. This term is associated with compressibility effects.

Lee (1997) points out that for high-speed turbulent flow, both the solenoidal and dilatational dissipative mechanisms are present. Shock waves and highly concentrated vortical regions are present in the flow. Hence, shock-shock, vortex-vortex, and shock-vortex interactions will play an important role in the energy dissipation mechanism.

1.2.2.2 Shock/Vortex Interaction

Although there is a wealth of information on shock/vortex interaction (Kao et al., 1996, Chatterjee, 1999, and Dosanjh and Weeks, 1965), this specific case of a confined expansion of a shock wave is a unique sub-set. Ellzey et al. (1995) performed some numerical studies on the interaction of a planar shock wave and vortex very similar to the

resulting flow of Jiang (1997). This work is entirely numerical and the interaction of shocks and vortices of various strengths was studied. Figure 1.3 present a schematic of shock structure during interaction with a vortex. Here it is seen that as the vortex encounters the shock wave, the shock is "diffracted" due to the presence of the vortex and, ultimately, splits.

a) incident shock   b) shock-vortex interaction   c) shock splitting
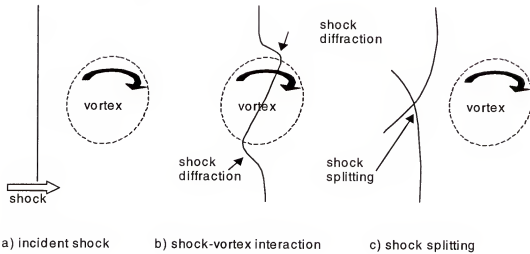
Figure 1.3 Structure of shock-vortex interaction

Although the work of Ellzey et al. (1995) is useful in understanding the aspects of shock/vortex interaction, there are subtle differences with the flow field resulting from a shock wave undergoing a sudden expansion and reflecting off a solid confining boundary and interacting with the vortex core. Also, the definition of "strong" and "weak" shock wave and "strong" and "weak" vortex needs to be considered. Ellzey et al. (1995) discuss the qualitative differences between a "strong" and "weak" vortex while interacting with a "strong" and "weak" shock. These definitions are merely relative and do not give a clear transition of shock/vortex interaction structure as a function of Mach number and/or

vortex strength. For example, Ellzey et al. (1995) quantify a "strong" shock as being Mach 1.5 and a "weak" shock as Mach 1.05.

The production of vorticity via the sudden expansion is also of interest. The formation of the "starting jet" gives rise to a vortex core above and below the orifice. In the case of a three dimensional expansion, a vortex ring would be formed. The production of vorticity is closely tied to the baroclinic torque ($\nabla p \times \nabla \rho$) in the vorticity transport equation; the modeling and understanding of which is currently not completely refined.

Another useful flow condition would be for the case of a shock wave traveling through a combustible mixture. As was stated previously, the shock wave can be used to initiate reactions within a mixture. Given sufficient length, this reaction will form a detonation wave and attain the CJ velocity of the mixture. However, for short lengths of geometry and especially for sudden expansion, the mechanisms for causing reactions will be very closely tied to the geometry and flow conditions. A shock-initiated reaction undergoing a sudden expansion has not been found in any references. This clearly is an area for further investigation, however, diagnostics for determination of reactions, etc., will be highly limited.

Of additional interest would be the linkage of the vorticity production and chemical reaction mechanisms. Riley and McMurtry (1996) cite that the baroclinic torque and thermal expansion due to reactions produce changes in the vortex structure. Miyauchi et al. (1995) and Valentino et al. (1998) also note this in their research as well.

1.3 Scope of Present Research

The preceding sections justify the use of a shock tube to study the fluid dynamic phenomena. As was seen, the sudden area expansion of a shock wave within a confined domain is composed of many interesting flow features. These include shock wave reflections, vorticity production, shock-vortex interaction, energy exchange between shock and turbulence, and shock focusing (Chang and Kim, 1995). The current research will expand upon these works and will offer new insight into the flowfield features and interactions. The following sections will focus in on current research of shock waves undergoing sudden expansion. A summary table of these works will be presented along with the objectives for the research of this work to clearly show the contribution of this effort.

Abe and Takayama (1990), Chang and Kim (1995), and Jiang et al. (1997) have investigated the fluid dynamic details of a shock or blast wave undergoing a sudden change in area. Some of the aforementioned phenomena associated with this sudden change are similar to that of an open-ended shock tube (e.g., vorticity production) whilst certain features are unique to a confined area expansion (e.g., shock-vortex interaction). These papers have used interferometry to compare experimental and numerical results. In all these references, a circular shock tube was studied both numerically and experimentally.

Figure 1.2 illustrated the salient flow features of such a sudden expansion within a confined region. Here is shown a shock wave that has undergone a sudden cross-section area expansion in a confined region. The flowfield gives rise to two important features

once the shock wave has undergone the sudden expansion. First, there is a "starting jet" which is characterized by the formation of a vortex ring, Mach disk, and shear layer. Second, this precursor shock reflects off the confining walls of the expansion chamber and interacts with the starting jet flowfield. Shock-vortex interaction occurs when the expanding shock wave that undergoes the sudden area expansion reflects off the confining wall and interacts with the vortex core that is produced at the sudden area change. This reflected shock splits once it interacts with the primary vortex ring, which gives rise to secondary shock waves.

Jiang et al. (1997) note that once the reflected shock wave passes through the developing shear layer, the shear layer splits. The split shear layer is then moved into the jet flow and convected downstream. This allows another shear layer to form from the jet exit forming another weaker vortex ring. This is referred to as shear layer splitting and is largely an inviscid phenomenon.

In highly compressible flows, an important vorticity production mechanism arises from the baroclinic torque, $\nabla p \times \nabla \rho$ (Krishnamurty, 1996, Valentino et al., 1998, Shyy and Krishnamurty, 1997, and Shyy et al., 1998). That is, vorticity is generated from the misalignment of the pressure and density gradients. Behind a curved shock caused by the geometric expansion, the pressure and density gradients are not parallel to each other, which, as given in the baroclinic torque term, can establish a vortex structure. As seen in Figure 1.2, the generation of a vortex "core" occurs as the fluid starts to exit from the sudden area expansion. It should be noted that the vorticity generation mechanism is inviscid and, consequently, the vortex and shear layer structures can be produced without

the influence of viscosity. Of course, as the flow further develops, the viscous effects become more influential and the baroclinic term will then interact with the viscous terms.

The aforementioned phenomena, vorticity production, shock-vortex interaction, shear layer development, etc. are important aspects for fluid mixing. Better understanding of the implications of mixing, especially for reactive flowfields, is crucial for modeling and understanding. The motivation for the current research stems from this need.

Current experimental research in this area are presented in Table 1.2. Here are seen basically two types of research on shock waves that undergo sudden expansion. The first type is sudden shock wave expansion into an unconfined region (Abe and Takayama, 1990, Yu and Grönig, 1996, and Jiang et al., 1999). The second type is sudden shock wave expansion into a confined region (Chang and Kim, 1995, Pantow et al., 1996, and Jiang et al., 1997). Here we note that for sudden shock wave expanding into an unconfined region only one paper discusses vortex tracking (Abe and Takayama, 1990) and only one paper gathers pressure data (Yu and Grönig, 1996). All of the papers on shock expansion in an unconfined region present time-accurate experimental flow visualization although it is only 2-3 frames. The work of Abe and Takayama (1990) and Jiang et al. (1999) use interferograms for the flow visualization while Yu and Grönig (1996) employ a color Schlieren system. An advantage of a color Schlieren system is that density gradients can be observed in all directions (Kleine and Grönig, 1991). In all three of these cases, however, the imagery is a two-dimensional integration of the flowfield that is highly three-dimensional.

Table 1.2 Review of current research on sudden shock wave expansion

Reference	Experimental	Numerical	Confined expansion? (ratio)	Cross-section shape (size)	Shock strength	Shock/Vortex Interaction addressed?	Shock reflection addressed	Vortex tracking?	Pressure Measurements?	Time accurate experimental results (frames)	Experimental flow visualization method	Comments
Abe & Takayama (1990)	✓	✓	no	circular (25mm)	1.5				✓	✓	interferogram	2-D visualization of 3-D flowfield, pressure along centerline
Yu & Göring (1996)	✓	✓	no	circular (56mm)	3.5			✓	✓	✓	2-D color Schlieren	
Jiang, Onodera, & Takayama (1999)	✓	✓	no	square (40mm)	1.29, 1.5		✓		✓	✓	interferogram	
Chang & Kim (1995)		✓	yes (3:1)	circular	1.5, 2.0	✓					Schlieren w/ vertical knife-edge	
Panow, Fischer, & Kranzel (1996)	✓	✓		rectangular	detonation wave	✓				✓	interferogram	
Jiang, Takayama, Babinsky, & Meguro (1997)	✓	✓	yes (3:1 & 2:1)	circular (25mm)	1.3, 1.5	✓				✓	interferogram	Aspheric lens used to minimize 3-D effects
Current work	✓	✓	yes (4:1)	Square (25mm)	1.5, 2.0, 3.0	✓	✓	✓	✓	✓	Schlieren via circular cut-off	Expansion occurs in one direction only; 2-D expansion, 8 frames of experimental data

Table 1.2 summarizes recent papers addressing the various aspects of the present topic, namely, a shock wave that expands into a confined region. Of these efforts, the work of Chang and Kim (1995) is entirely numerical while the work of Jiang et al. (1997) is numerical and experimental. Pantow et al. (1996) detail the sudden expansion of a detonation wave that travels down a rectangular tube into a confined region and use a knife-edge Schlieren system for flow visualization. None of these efforts present detailed quantitative data of major flowfield features that evolve in time. That is, there is no tracking of the vortex core as it is convected through the flowfield. Jiang et al. (1997) employ an aspheric lens to visualize the three-dimensional expansion with an interferometric optical system. The aspheric lens collimates the light beams that pass through the test region allowing for easy comparison with numerical data. An interferometer is an excellent tool for quantitative measurement of the subject flowfield. However, Schlieren flow visualization, although qualitative, can offer greater insight into the fluid dynamic structure.

In this work, experimental flow visualization and wall pressure data are gathered in a specifically designed shock expansion device. A unique distinction in the present work is that the cross section of the shock tube at the sudden expansion is square rather than circular. That is, the shock tube is allowed to suddenly expand in one direction only. Optical windows bound the exit of the square shock tube on opposite sides. The area is allowed to suddenly expand on the other two sides only. This allows for a nearly two-dimensional expansion of the shock to facilitate experimental observation and the comparison to numerical and analytical results.

The goal of this research is to provide new information about the fluid dynamic field using state-of-the-art instrumentation and techniques. Unlike most transducers (e.g., pressure or temperature) which can measure only one specific parameter, optical records can provide several measurement parameters simultaneously. Time resolved records provide additional insight with its ability to be viewed in sequence much like a movie that is a sequential viewing of individual pictures. This added feature is essential to determine the development of fluid dynamic features such as vortices and shear layers. Additionally, the time-accurate flow visualization system allows examination of events that occur at microsecond intervals to be viewed at much slower rates for human eye examination. Use of state-of-the-art digital cameras allows for immediate inspection of the recorded data as well as the ability to analyze the data digitally.

1.4 Summary

The use of a shock tube is ideally suited for the study of fluid dynamic phenomena. A shock tube generates a shock wave that uniformly and instantaneously increases the fluid to elevated temperature and pressure levels. A shock that is traveling down a shock tube and undergoes a sudden expansion gives rise to many fluid dynamic phenomena such as vorticity production, shear layer production, and compressibility effects. The confinement of this expanding shock gives rise to additional fluid dynamic phenomena such as shock reflection, mixing, and shock/vortex interaction. Collectively, all of these phenomena are of interest in the modeling of fluid flow via numerical methods. Accurate models are required to simulate complex flowfields.

The current research will expand upon existing experimental and computational data for shock waves that undergo sudden expansion. The distinction of the current work is that the shock will expand from a square tube and is allowed to only expand in two-dimensions. This will help alleviate the problem of three-dimensionality in the resulting flow visualization data. The current work will allow for the detailed study of shock/vortex interaction, shock reflection, will provide time-accurate flowfield visualization data, and will provide wall pressure data of the confining chamber as the shock undergoes expansion. This work plan is more comprehensive and complete than current work in the literature.

CHAPTER 2
EXPERIMENTAL APPARATUS

This chapter presents the design methodology for the development and construction of the shock tube expansion device (STED) on which this research is based. The experimental device described herein will be designed for and closely coupled with numerical modeling development. Both experimental and theoretical efforts are being pursued to address the various issues related to fluid dynamic aspects of sudden shock wave expansion. The experiments to be conducted in this device are designed to help elucidate some key modeling questions by providing flow visualization, wall pressure data, and flow structure development.

2.1 Device Concept and Design

The design of the shock tube expansion device in support of this research is based upon the operation of a shock tube. In a shock tube, as outlined in Section 1.1.1, a high-pressure reservoir will be allowed to rapidly expand into a tube of lower pressure, thus creating the shock. Careful selection of gases and initial conditions can tailor the shock to desired levels. At the exit of this low-pressure tube is the shock expansion chamber where flow visualization and detailed measurement will take place. The gas ultimately expels into a "catch tank" so as to contain the final products of the experiment.

2.1.1 Design Objectives

The following objectives were established during the design on this shock tube expansion device. The ultimate goal is to provide for time accurate flowfield visualizations within the device that provide the necessary insight as described earlier.

The device operation objectives are as follows:

- Size Requirements: The requirement that determined the size for this device is the optical diagnostic system. The ideal location is within a laboratory environment, and as such, placed size requirements on the device.

- Instrumentation: This device takes advantage of state-of-the-art laser based optical diagnostics as well as conventional pressure transducers. The design of the device accommodates these existing systems.

- Performance: The type of experiments to be conducted and the use of the data collected is known a priori. This determines the device performance requirements; i.e., what strength of shock is required, et cetera.

- Observation window: The device has windows on the chamber of sufficient size to allow optical access.

- Easy to Use: The device is simple to operate and allows for parametric studies. It is also able to provide repeatability at desired conditions. The time required to set up for and conduct experiments must be of reasonable duration as well.

- Extension of Prior Work: The device needs to extend the knowledge of prior researchers. As such, the experiments to be conducted should be a logical progression from prior efforts.

- Easy to Build: The device was constructed with material that is readily available and easily fabricated in a standard machine shop.

2.1.2 Design Methodology

The heart of the shock tube expansion device is the shock tube itself. The shock tube needed to be of sufficient size and be capable of producing shocks of sufficient strength to satisfy the aforementioned research goals. Figure 1.1 presented a schematic of shock tube operation. Here it was seen that a high-pressure driver gas is separated from a

low-pressure driven gas by a diaphragm. Once the diaphragm ruptures, a shock is created that travels into the low-pressure driven gas, and an expansion fan propagates into the high-pressure driver gas. A "contact surface", which is the interface between the driver gas and driven gas, propagates into the low-pressure section as well.

Based upon the research goals, it was determined that a shock strength of Mach 1.5-3.0 is required with dry air as a test gas. In order to maximize shock tube performance, one needs to use a light gas in the driver section of the tube and a relatively heavy gas in the driven section (Anderson, 1990). Gases readily available within the laboratory for this use are helium, argon, dry air, and nitrogen.

Anderson (1990) provides a method for calculating shock tube performance given the initial conditions within the tube. The equations were detailed in Section 1.1.2.1 and will not be repeated here. However, we will go through these equations to achieve a set of initial conditions to generate the required shocks of interest; namely Mach 1.5, 2.0, and 3.0.

To achieve a Mach 3 shock in dry air, it is necessary to use helium as a driver gas. The design of the shock tube expansion device requires that the driven and driver gases are very close to room temperature, 296K. From the shock tube relations presented in Section 1.1.2.1, it was readily determined that the driver gas of helium at 4.826×10^6 Pa (700 psi) will produce a Mach 3.0 shock in dry air at a pressure of 1.014×10^6 Pa (14.7 psi).

In a similar manner, shock with Mach numbers of 2.0 and 1.5 could be easily produced in the shock tube expansion device as well. Table 2.1 presents the gases and conditions necessary to produce the desired shocks in the shock tube expansion device.

Here, W is the velocity of the shock wave in the driven gas and u_p is the velocity of the gas behind the shock as well as that of the contact surface.

Table 2.1 Shock tube expansion device initial conditions and shock properties for desired shock strengths

Driver Gas/ Pressure (Pa)	Driven Gas/ Pressure (Pa)	p_4/p_1	p_2/p_1 via eq. 1.1	M_s	W (m/s)	u_p (m/s)
Argon/4.137E6	Air/4.137E5	10	2.434	1.493	514.9	236.6
Nitrogen/3.447E6	Air/1.014E5	34	4.577	2.016	692.3	450.0
Helium/4.826E6	Air/1.014E5	47.6	10.71	3.053	1053	795.7

2.1.3 Design Parameters

The selection of the shock tube cross section size and shape plays a major role. Gaydon and Hurle (1963) indicate that a shock tube diameter of 25 to 100 millimeters with a length of 40 to 100 diameters is optimal. For strength considerations, a round tube is best with the smaller diameters being strongest. The flow within the shock tube is "cleaner" with a round cross section. However for optical flow visualization a cross section with parallel walls is best.

Based upon these guidelines and the ultimate goal of this research, the following design choices were made for the shock tube:

- The shock tube itself is 25 mm in diameter. This affords the greatest strength, the minimal length, and the optimum flow condition.

- The shock tube is about 1 meter in length. The high pressure driver section is approximately one half this length.

- At the entrance to the chamber, the circular cross-section transitions to a 25 mm by 25 mm square cross-section over 100 mm. This is followed by a 38 mm long extension of the square cross-section before the sudden expansion.

- The chamber of the shock tube expansion device is 25 mm wide by 100 mm high and is 275 mm in length. Optical flow visualization occurs only in the first 150 mm.

- The windows of the chamber of the shock tube expansion device restrict expansion of the flow in one dimension.

- The window material is fused quartz to minimize optical interference.

2.1.4 Device Support Systems

There are a number of sub-systems that are needed to support the operation of the shock tube expansion device. These include methods to initiate the experiment, gas handling, and instrumentation. The following sections outline these and other critical sub-systems in detail.

2.1.4.1 Initiation

It is a requirement that the initiation of the experiment be at a prescribed condition and that this condition be repeatable. The optimum method for initiating a shock tube experiment is with a burst diaphragm (Gaydon and Hurle, 1963), usually of metal alloy. However, even under extremely close machining processes and tolerances, it is not always possible to produce diaphragms that burst at one prescribed pressure. Also, if one wanted to vary the initial pressure for the experiment, a multitude of diaphragms would be necessary.

A simple but effective solution to this problem is to use a double diaphragm system (Bradley, 1962). Such a double diaphragm system, as shown in Figure 2.1, incorporates two burst diaphragms that form an intermediate pressure section between the high and low pressure sections of the shock tube. The pressure within the intermediate section is approximately one half of the pressure in the high-pressure section. In such a configuration, each diaphragm sees only half of the total pressure differential from the

high to low pressure sections. Thus, the diaphragms used in this system need only be strong enough to withstand half of the total pressure differential.
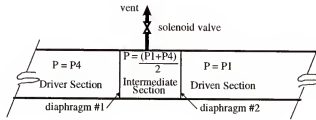
Figure 2.1 Schematic of double diaphragm system to initiate experiments within the shock tube expansion device

Upon experiment initiation, the intermediate pressure section is vented via solenoid valve for a short period of time causing the pressure difference across diaphragm #1 to increase ultimately causing the diaphragm to burst. The full force of the increased pressure differential is then brought to bear on diaphragm #2 causing it to burst moments later. This versatile arrangement allows for specific tailoring of shock strength and experiment initiation.

2.1.4.2 Gas Handling

Another important consideration in the design of this shock tube expansion device was the separation of gas within the shock tube and gas within the chamber. The reasons for separating these gases until the arrival of the shock wave will be seen in the following sections. Suffice it to say we need some system to physically separate the two gases until the shock arrives at the chamber. A simple method would be another diaphragm. However, the implementation of this would be difficult in practice since it would require the disassembly of the chamber for each experiment. A simple mechanical device to separate the two gases that caused little if any disturbance to the gases while it was

opened would be desirable. One such method uses a ball valve. A ball valve allows unrestricted flow when in the open position. However, opening the valve takes a finite amount of time and any pressure differential across the valve will cause some gas flow. The solution would be to have zero pressure differential across the valve, which is readily accomplished. Also, an electrically driven ball valve would open the valve smoothly. Once open, the ball valve's electrical assembly signals the double diaphragm system to initiate the experiment, thereby minimizing the time the gases interact through the valve before the shock is produced and enters the chamber.

As previously mentioned the shock tube expansion device uses helium and nitrogen in the production of the shocks but also needs a system to introduce the test gases into the chamber (e.g., hydrogen and air). Additionally, prior to the experiment, we need to evacuate the air within the device, and we also need to vent the products after the experiment is over. A gas handling system to easily and efficiently conduct these tasks as well as initialize the shock tube for the experiments was needed. Figure 2.2 shows the schematic of the gas handling system designed for the shock tube expansion device.

2.1.4.3 Electrical System

A schematic of the electrical system of the shock tube expansion device is shown in Figure 2.3. The electrical system for this shock tube expansion device came about mainly because of the need for the electrical operation of the ball and solenoid valves plus the ability to remotely initiate the experiment. Electrical service was also needed at the control panel for panel meters and indicator lights. Additionally, a remote fire control box, which consists of a key-lock "Arming" switch and toggle "Fire" switch, is used to initiate the experiments from a safe distance and is also part of the electrical system.
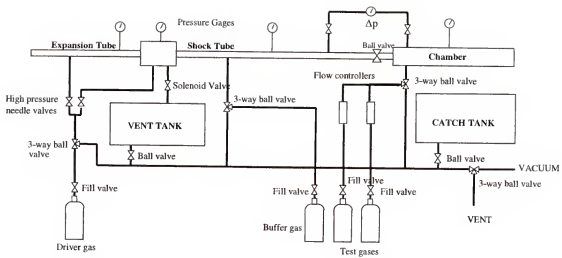
Figure 2.2 Schematic of gas handling system for shock tube expansion device
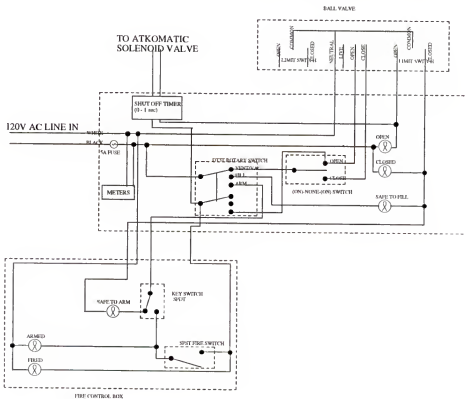
Figure 2.3 Electrical system schematic for shock tube expansion device

2.1.4.4 Plumbing

The plumbing system is necessary to deliver the necessary gas to all the components of the shock tube expansion device. The system needed to be able to evacuate all components of the shock tube expansion device via vacuum pump. Turning three-way valves then enable the system to be filled with the desired gas to specified pressures. Once the experiment is complete, the three-way valves are then set to vent the test gases to the laboratory. Needless to say, stainless steel tubing and components make up the system with all components rated to 34.5×10^6 Pa (5,000 psi).

2.1.4.5 Control Panel

The control panel of the shock tube expansion device is depicted in Figure 2.4. The control panel houses all the valves and LED readouts for pressure and temperature that allow safe operation of the device. The are also indicator lights on the panel to indicate the position of the ball valve and that the high pressure section is safe to fill. The
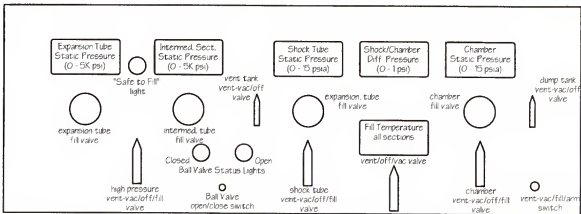
Figure 2.4 Control panel schematic for shock tube expansion device

panel is arrayed with digital indicators for static pressure and temperature in all sections of the device. The fill valves are located by these read-outs for precise filling of the test gases.

2.1.4.6 Instrumentation

There are two data instrumentation systems in this shock tube expansion device. The first is a system of dynamic pressure transducers to measure the actual shock properties and the second is an optical flow visualization system.

The pressure instrumentation system consists of four dynamic pressure transducers. Two of these dynamic pressure transducers are installed in the shock tube and two are installed in the expansion chamber. The function of these instruments is to measure the actual shock performance. This is accomplished by measuring the shock arrival time between the two transducers within the shock tube and, given the distance between the two transducers, the shock speed can be determined. This can be coupled with the magnitude of the pressure rise across the traveling shock (also measured by the transducers). Not only can shock speed be determined but the strength of the shock at the two locations can be compared to assess shock strength loss in the shock tube. The placement of the transducer within the shock expansion chamber will allow assessment of shock magnitude during the expansion process. This non-intrusive process will be an excellent means to compare with results of numerical data.

Flow visualization is a major objective of our research and provides time accurate density visualization of the flowfield. Recently, advances in instrumentation and techniques have occurred which allow for more detailed information within the flowfield. For example, high-speed framing cameras are now available that can be coupled to a

traditional shadowgraph or Schlieren optical system. Furthermore, advances in optical measurement techniques have increased the sensitivity of density visualization approaches (Anderson, 1995 and Anderson et al., 1995). Chapter 3 of this work will detail the optical visualization system in greater depth.

2.1.5 Complete Device

A photograph of the complete shock tube expansion device assembly is depicted in Figure 2.5 and is shown schematically in Figure 2.6. The shock tube expansion device is approximately 4 feet high and 8 feet in length. Here all features of the design are shown. Note that the dump tank and catch tank provide a mounting assembly for the shock tube and chamber. This also minimizes the overall length of the shock tube expansion device. The shock tube expansion device incorporates wheels to facilitate easy repositioning of the device with in the laboratory. Figure 2.7 is a schematic of the entrance of the expansion chamber and Figure 2.8 is an isometric schematic of the shock tube expansion device entrance.

The operation of the shock tube expansion device proceeds as follows: The complete device is assembled with the proper diaphragms. The rotary switch is set to the "Vent/Vacuum" position which allows for control over the ball valve but prevents operation of the solenoid valve. The entire device is evacuated via vacuum pump by proper settings of the control valves. The operator ensures the fire control switch is open and removes the key from the key switch on the fire control box. The rotary switch is then set to the "Fill" position which electrically isolates the ball valve and provides a green "Safe to Fill" light that signifies the device is ready to be filled. The device is now ready for gas fill. The chamber and shock tube are filled first to the desired low pressure.
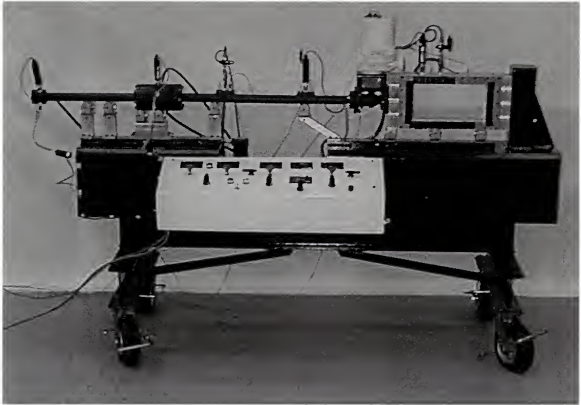
Figure 2.5 Photograph of the shock tube expansion device
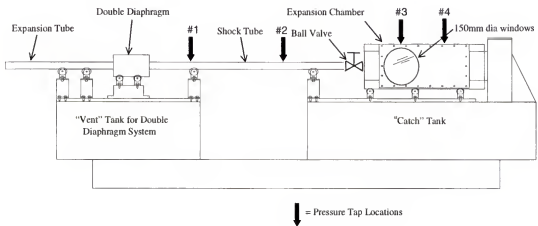
Figure 2.6 Schematic of the shock tube expansion device
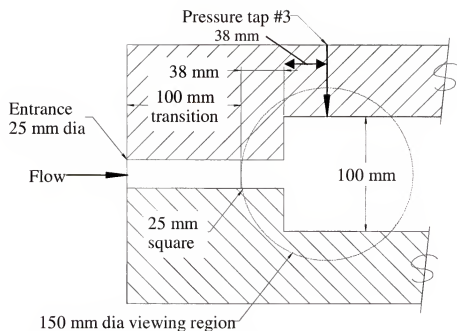
Figure 2.7 Schematic view of expansion chamber of the shock tube expansion device
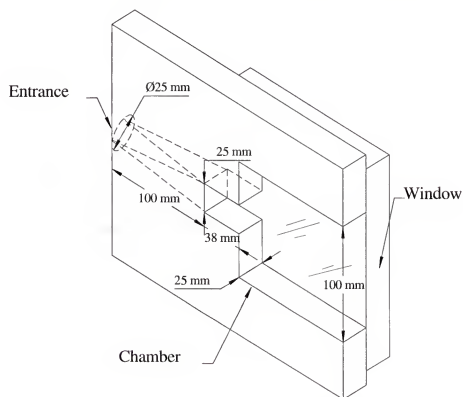
Figure 2.8 Isometric view of expansion chamber of the shock tube expansion device

A differential pressure transducer helps ensure both the shock tube and chamber are at the same initial pressure. The high and intermediate pressure sections are filled next to the intermediate pressure. The high pressure section continues to be filled to the desired high pressure. Now that the shock tube expansion device is set to the desired initial conditions, the rotary switch is set in the "Arm" position; a green light on the fire control box indicates that it is then "Safe to Arm" the device. The operator uses the key switch to arm the device, which illuminates a yellow "Armed Light" on the fire control box. Throwing the "Fire" switch on the fire control box initiates the ball valve opening; a red "Fired" light illuminates on the fire control box. Once the ball valve is completely opened, a timed electrical signal is sent to the solenoid valve which causes the intermediate pressure between the burst diaphragms to rupture, thus creating the shock.

<u>2.2 Device performance</u>

<u>2.2.1 Shock Tube Performance</u>

Table 2.1 listed the shock tube parameters for shocks of strength Mach 1.5, 2.0, and 3.0 produced in dry air. The information in the table along with the geometry of the shock tube expansion device is used to construct x-t diagrams of the shock tube. An x-t diagram is useful in the understanding of the flowfield within the shock tube. Figure 2.9 presents a detailed explanation of a typical x-t diagram for a shock tube. In an x-t diagram, the horizontal axis represents the position within the shock tube and the vertical axis represents time. Diaphragm burst represents time 0.0 and the location of the expansion wave, contact surface, and shock front can be found at any time thereafter by taking a horizontal "slice" at that time.
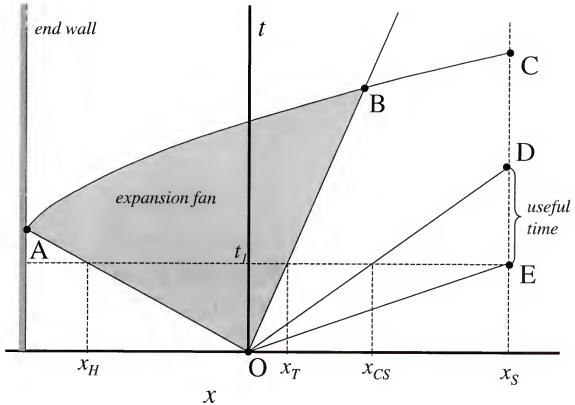
Figure 2.9 Typical shock tube *x-t* diagram

For instance, in Figure 2.9, O represents the position of the diaphragm. Line O-A depicts the location of the head of the expansion fan that propagates into the high pressure region. Line O-B represents the tail of the expansion fan. Note, depending on the initial conditions, the tail of the expansion fan can propagate either into the high pressure or low pressure section. Line O-D represents the contact surface that propagates into the low pressure section and, similarly, line O-E represents the location of the shock wave. Note that the inverse slope of line O-E is the shock wave propagation speed (W). Since the high pressure section is finite in length, the head of the expansion fan will reflect off the end-wall. This reflection is shown as line A-B. The curvature of this line represents the expansion fan reflecting upon itself. The line B-C represents the reflected

expansion fan head propagating into the low pressure section. Line D-E represents the "useful" time for experimentation. That is, it is the time from the arrival of the shock wave to the arrival of the contact surface. During this time, the gas within the shock tube has been imparted with momentum from the shock wave and exits the tube. Care must be taken in the shock tube design to assure this time is of sufficient length for meaningful experiments. It is possible in some instances that the line B-C will intersect line O-D thereby reducing the available experimentation time

Figures 2.10-2.12 show the *x-t* diagrams for the Mach 1.5, Mach 2.0, and Mach 3.0 cases of Table 2.1 respectively. Each of these Figures was constructed with the geometry of the shock tube expansion device and initial conditions of Table 2.1. Also shown on each Figure is the location of the two pressure transducers.

It is seen in Figure 2.10 for the Mach 1.5 case that the tail of the expansion fan propagates slightly into the high pressure region. It is also seen that the shock arrives at the entrance to the shock tube expansion device about 0.002 seconds after diaphragm burst. The available time for experimentation is about 0.0025 seconds. For the Mach 2.0 and 3.0 cases the experimentation times are given in Table 2.2.

Table 2.2 Useful time for experimentation of shock waves produced in the shock tube expansion device

Shock Mach Number	Shock Speed (m/s)	Shock arrival time at STED Entrance (mS)	Useful Time (mS)
1.493	514.9	2.047	2.408
2.016	692.3	1.523	0.819
3.053	1053	1.001	0.324

38
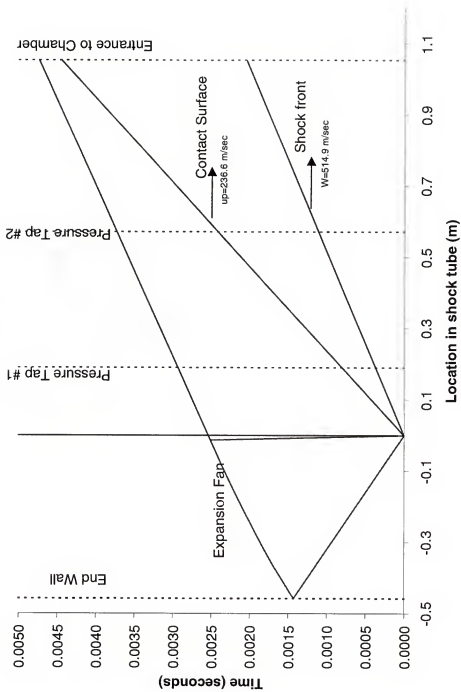
Figure 2.10 *X-t* diagram for a Mach 1.5 shock produced in the shock tube expansion device
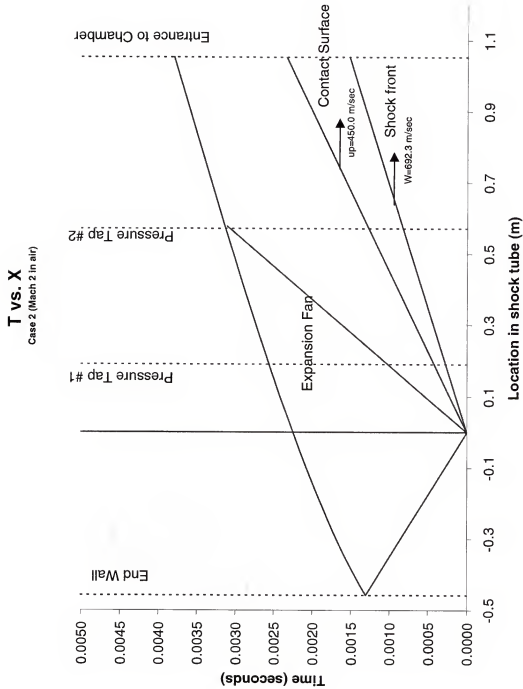
Figure 2.11 *X-t* diagram for a Mach 2.0 shock produced in the shock tube expansion device
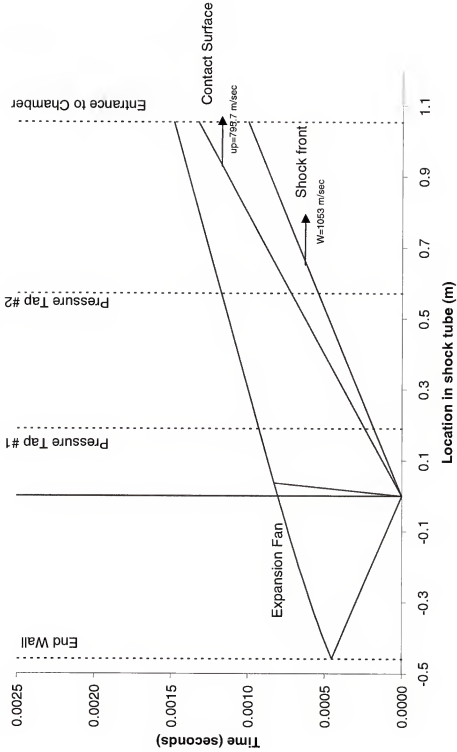
Figure 2.12 *X-t* diagram for a Mach 3.0 shock produced in the shock tube expansion device

2.2.2 Pressure Performance

Shock tube performance can be measured by both the pressure increase of the low pressure section from the passage of the shock and the speed of the shock (W) itself. The shock tube expansion device shock tube was designed to incorporate two pressure transducers to measure these quantities.

Based upon the *x-t* diagrams presented in Section 2.2.1 for the three Mach numbers cases, the *Pressure vs. Time* traces can be readily constructed. These data are presented in Figures 2.13-2.15 for the three cases of interest. Ideally, the passage of the shock serves to uniformly and instantaneously raise the pressure of the quiescent gas to an elevated level. The ratio of raised pressure behind the shock (p_2) to quiescent pressure (p_1) is given in table 2.1 for the three cases of interest. The pressure across the contact surface remains constant until the arrival of the reflected expansion fan. Figures 2.13-2.15 depict the theoretical pressure profile for each transducer based upon physical location. Note that the shock arrival time difference is a function of the shock speed (W) and physical separation of the transducers.

2.2.3 Shock Quality

All the data presented in Figures 2.10-2.15 are based upon the theoretical equations that govern shock tube flow as presented in the first chapter of this work. Comparing the actual measured data to these theoretical data is now necessary to judge the experimental device performance.

Figure 2.16 shows the actual transducer data from the shock tube expansion device for a shock Mach number of 1.5. Note that for this and all subsequent transducer data, the transducer measures only the dynamic pressure. That is, prior to shock arrival
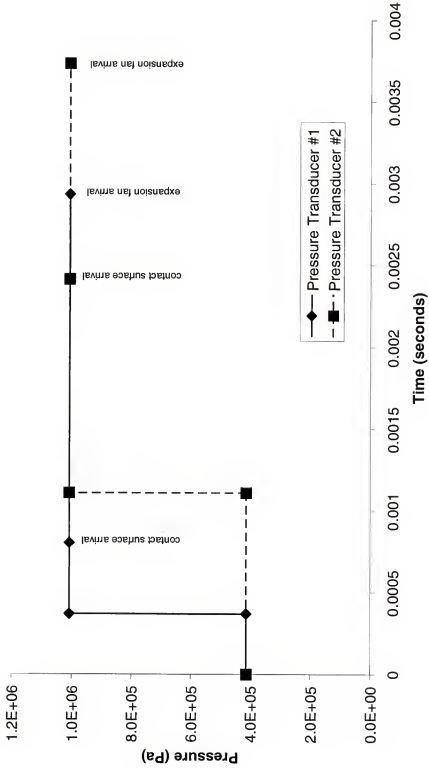
Figure 2.13 *Pressure vs. Time* plot for a Mach 1.5 shock produced in the shock tube expansion device
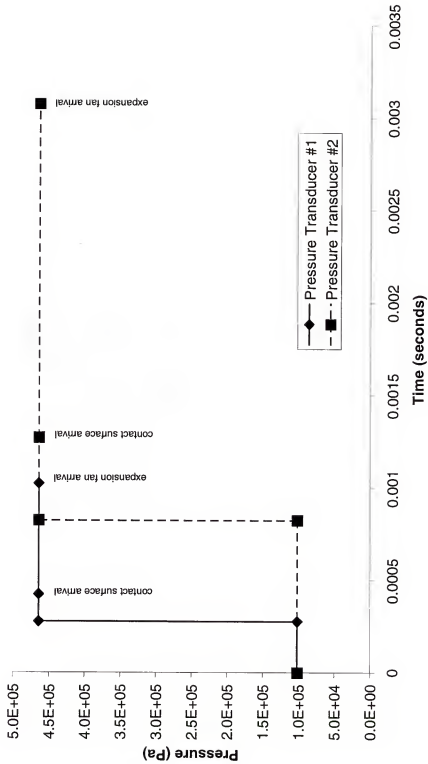
Figure 2.14 *Pressure vs. Time* plot for a Mach 2.0 shock produced in the shock tube expansion device

44
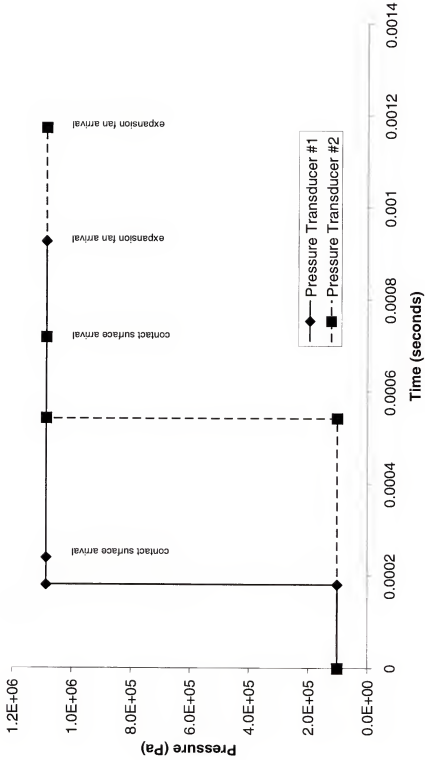
Figure 2.15 *Pressure vs. Time* plot for a Mach 3.0 shock produced in the shock tube expansion device
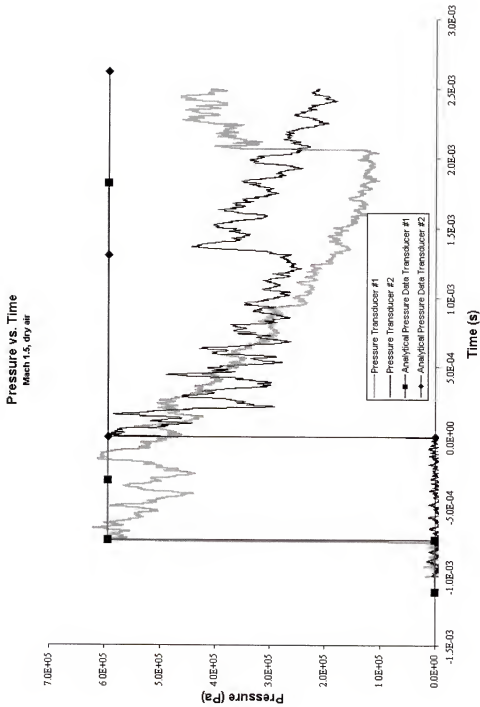
Figure 2.16 Experimental and analytical *Pressure vs. Time* plot for a Mach 1.5 shock produced in the shock tube expansion device where diaphragm is burst via double diaphragm method

the transducer reads 0.0 Pa. A correction for the quiescent pressure must be applied to compare with the data of Figures 2.13-2.15. Included in Figure 2.16 is the theoretical transducer data for direct comparison.

It is evident from this comparison that excellent agreement exists for the shock speed (W) since the shock arrival times coincide quite well. It is also evident that the shock strength agrees well also since the pressure behind the shock is very nearly that of the theoretical value. However, in sharp contrast to the theoretical data there are two aspects that do not agree well. The first is that the shock strength falls soon after shock arrival. The second is that there is a distinctive "ringing" in the pressure data for the number two pressure transducer. This ringing was repeatable from one shot to the next. The following sections will address each of these aspects in greater detail.

2.2.3.1 Fall off in Shock Strength

Upon observation of the fall off in shock strength soon after shock arrival an investigation of the possible causes was started. It was suspected that the method for initiation may be the cause. Section 2.1.4.1 detailed the design and operation of the double diaphragm initiation system. It was suspected that poor operation of this component may have contributed to the fall off in shock strength. Perhaps the opening of the valve to reduce the central pressure was actually allowing a significant amount of the high pressure gas to escape. To prove this assumption, a trial was conducted at roughly the same conditions but without using the double diaphragm method. To achieve this, the high pressure section was filled until the diaphragm burst of its own accord. The results of this trial are shown in Figure 2.17. A slightly higher strength shock (Mach 1.51 vs.
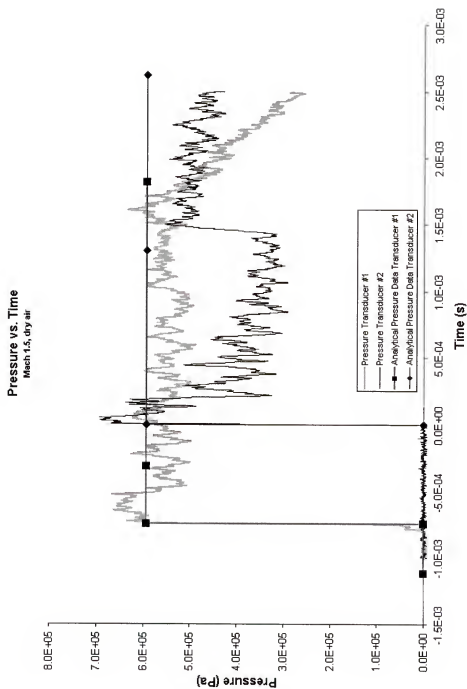
Figure 2.17 Experimental and analytical *Pressure vs. Time* plot for a Mach 1.5 shock produced in the shock tube expansion device where the diaphragm is bust via overpressure

1.49) was formed but the results are still valid for comparison. It is immediately noted that for the number one pressure transducer the peak pressure remains at the elevated level until the arrival of the expansion fan. However, there was still the same "ringing" of the data and there was still the drop-off in pressure after the number two pressure transducer. It was concluded that since the shock arrival times and associated pressures were extremely close to predicted values that the shock was being produced correctly. Suspicion for the pressure fall-off and ringing in the number two transducer was centered on the geometric tube itself.

2.2.3.2 "Ringing" of Pressure Data

Disassembly of the shock tube expansion device and an internal inspection of the shock tube was conducted. A bore-scope, used to inspect rifle barrels, was used to image the inside of the shock tube for clues. It was quickly noted that just prior to the number two pressure transducer there was a large port used for static pressure measurement. This hole is 9.5 mm in diameter whereas the shock tube diameter is 25 mm. Figure 2.18 is a photograph of the inside of the shock tube at the number two pressure transducer location. It was therefore suspected that this inordinate sized hole was the source of pressure loss and ringing.

It was easier to redesign and build a new shock tube than repair the existing one. A thick-walled tube was used for the new shock tube and 1.6 mm access holes were used where required.

Figure 2.19 depicts the pressure traces from a Mach 1.5 shock generated with the new shock tube. It is clearly evident from this data that the shock tube performance is vastly improved.
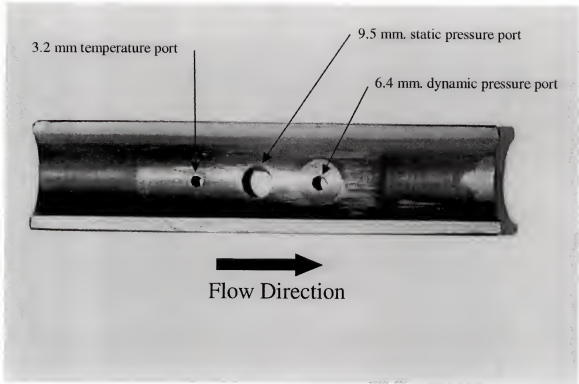
Figure 2.18 View of original shock tube ports in location of #2 pressure transducer

2.2.3.3 Old Tube vs. New Tube Data

The question now arises is how useful is the data (both optical and pressure) generated with the old tube vs. the new tube. Logic would indicate that all new data be generated for detailed analysis. A direct comparison of old tube vs. new tube data was performed. Surprisingly, the data did not show any appreciable change from one tube to the next. Figures 2.20 and 2.21 present optical images from the old and new shock tubes for a similar Mach number and time. No differences in the data are noted. And perhaps more convincingly, the pressure data within the shock expansion chamber are nearly identical for old tube and the new tube as shown in Figure 2.22. Also shown in this Figure is the pressure trace from the trial where the double diaphragm was used.
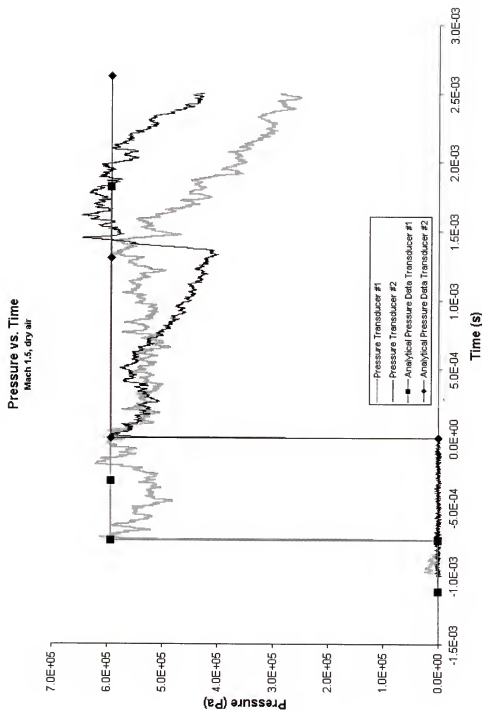
Figure 2.19 Experimental and analytical *Pressure vs. Time* plot for a Mach 1.5 shock produced in the shock tube expansion device with new, thick walled, shock tube

a) original shock tube
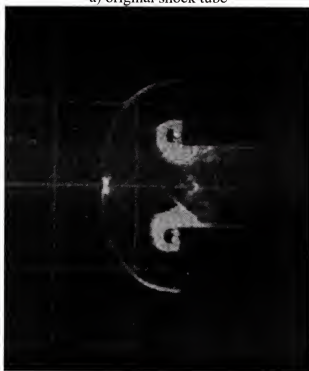
b) new shock tube

Figure 2.20 Comparison of optical data at Mach 1.5 for original shock tube vs. new shock tube during initial shock expansion
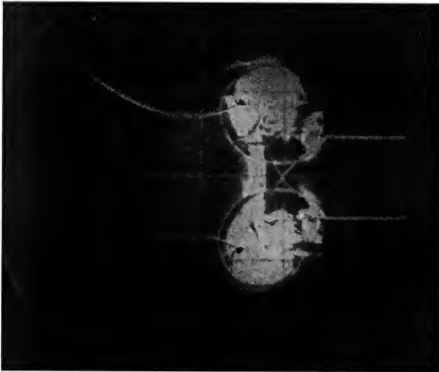
a) Old Tube

b) New Tube

Figure 2.21 Comparison of optical data at Mach 1.5 for original shock tube vs. new shock tube during shock reflection and interaction
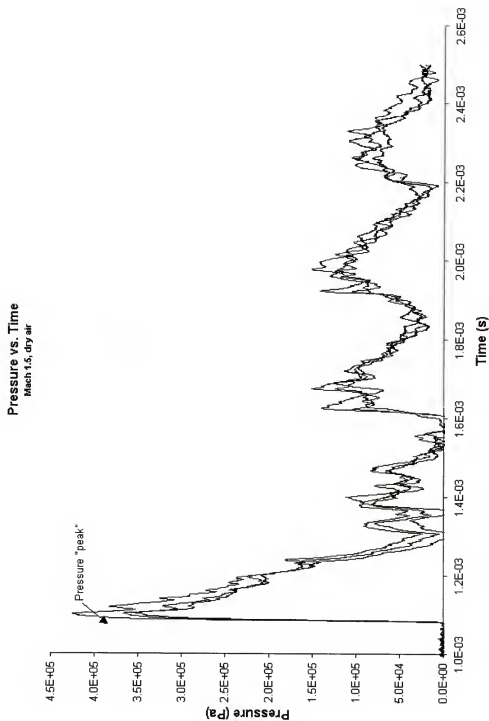
Figure 2.22 *Pressure vs. Time* data for pressure transducer #3 for shock waves produced with and without the double diaphragm in the original shock tube and a shock wave produced with the new shock tube

Based upon this data, it was concluded that all of the experimental data gathered by the shock tube expansion device is valid for analysis in this work.

2.2.4 Transducer Performance

The transducers used for this work are PCB® model 113A36. This transducer has a 500,000 hertz , one microsecond response time. This transducer is specifically designed for shock tube operations. However, the diameter of the transducer is 6.4 mm and given the fact that the shock tube itself is 25 mm in diameter it was prudent to investigate the transducer response for later comparison with numerical data.
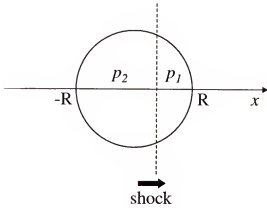
Figure 2.23 Schematic of shock wave passing over pressure transducer

Figure 2.23 shows an end view of the circular pressure transducer that is nearly flush with the shock tube wall. Also shown is the passing shock wave at some position across the transducer. If the pressure ahead of the shock is p_1 and the pressure behind the shock is p_2, then the integrated pressure over the transducer is given by

$$P = \frac{2}{A}\left[p_2 \int_{-R}^{x} \sqrt{R^2 - x^2}\, dx + p_1 \int_{x}^{R} \sqrt{R^2 - x^2}\, dx \right]$$

(2.1)

where P is the integrated pressure over the face of the transducer, R is the radius of the transducer face, A is the area of the transducer, and x is measured from the center of the transducer. This integral equation has an exact solution given by

$$P = \frac{2}{A}\left[\left(p_2 - p_1\right)\left[\frac{x}{2}\sqrt{R^2 - x^2} + \frac{R^2}{2}\sin^{-1}\frac{x}{R}\right] + \left(p_2 + p_1\right)\frac{\pi R^2}{4}\right]. \qquad (2.2)$$

Since the x-location of the shock front is a function of it's speed (W), a *pressure vs. time* chart can be constructed using small (i.e. microsecond) time steps. Figure 2.24 presents the time-accurate solution to Equation 2.2 and is compared to actual transducer data. Here it is clearly seen that the response of the transducer is adequate for the pressure measurement and that the size is not excessive.
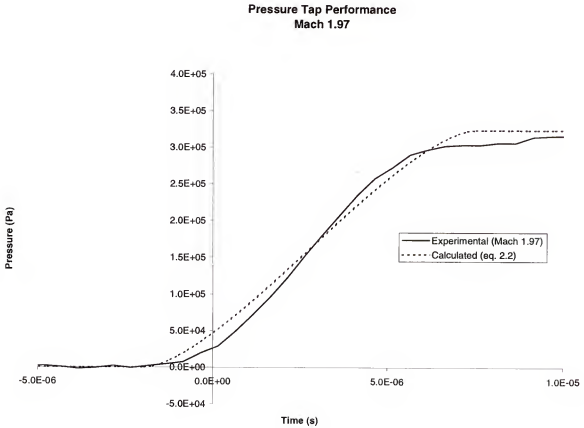
Figure 2.24 Pressure transducer performance for Mach 1.97 shock and comparison with analytical data

2.2.5 Expansion Chamber Transducer Performance

The previous section presented an analysis of transducer data when a uniform shock passes. In the expansion chamber itself, the expanding shock wave is unsteady and the pressure at the transducer location varies as a function of time. For the comparison of the experimental data to forthcoming numerical data, a method to account for transducer size is presented.
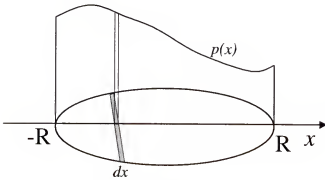
Figure 2.25 Schematic of pressure transducer within the expansion chamber subject to time-varying pressure

Figure 2.25 depicts the situation within the expansion chamber of a two-dimensional time varying shock wave passes over the transducer. Again, x is measured from the center of the transducer and the integrated pressure is given by the expression

$$P = 2 \int_{-R}^{R} p(x)\sqrt{R^2 - x^2}\,dx. \tag{2.3}$$

Since the radius of the transducer is 6.4 mm, there may be a difference in the actual pressure recorded by the transducer as the time varying pressure wave passes. However, this will only be the case for sharp changes in the pressure as it traverses the transducer. This occurs at two instances: 1) When the shock wave passes the transducer and 2) when the peak pressure passes the transducer as seen in Figure 2.22.

The function $p(x)$ is not readily known in equation 2.3. A first order simplification to equation 2.3 would be to estimate the pressure at three locations along

the transducer: at the beginning, middle, and end. Figure 2.26 represents this simplified pressure variation. The assumption is that the pressure varies linearly from the three locations. The pressure for this case is then given as

$$P = 2\left[\int_{-R}^{0}\left[\frac{(p_2 - p_1)x}{R} + p_2\right]\sqrt{R^2 - x^2}\,dx + \int_{0}^{R}\left[\frac{(p_3 - p_2)x}{R} + p_2\right]\sqrt{R^2 - x^2}\,dx\right] \qquad (2.4)$$

where p_1, p_2, and p_3 are the pressures at the beginning, middle, and end of the transducer.
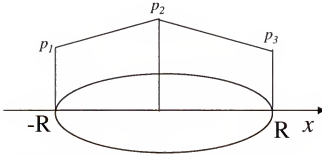
Figure 2.26 Schematic of pressure transducer within the expansion chamber with simplified time-varying pressure

Equation 2.4 can be numerically integrated to convert numerical pressure data along the chamber wall to the value the transducer reads. This will be used in later sections when experimental and numerical data are compared.

2.3 Summary

A unique device to observe and measure a shock wave undergoing a sudden expansion has been developed. Based upon the review of current literature and needs of the numerical modeling community, a shock tube expansion device was conceived, designed, and constructed for this effort. In addition to the shock tube itself, support systems such as gas handling and instrumentation were designed and constructed as well.

The result is a device uniquely capable to observe the sudden expansion of a shock wave within a confined chamber. The device itself is capable of generating shocks

of various strengths; anywhere from mach 1.2 to Mach 3.0 and above. The device is compact, mobile, and is ideal for laboratory use.

The quality of the shocks produced by the device has been analyzed and come extremely close to predicted values. A fault with the original tube manufactured for the device was identified and the tube was remanufactured. However, it was seen that the faulty tube did not effect the pressure or visual data within the chamber itself.

Finally, methods for evaluating pressure transducer performance were presented. The results indicated that the transducers used in the experiments accurately capture the passage of the shock. A method to evaluate computational data to the measured data was derived and will be used in subsequent sections.

CHAPTER 3
FLOW VISUALIZATION SYSTEM

This chapter details the optical flow visualization system used in this research. The goal of the optics system is to provide new information about the fluid dynamic field using state-of-the-art instrumentation and techniques. Unlike transducers (e.g., pressure or temperature) which can measure only one specific parameter, optical records can provide several measurement parameters simultaneously. In addition, time resolved records can provide additional insight in their ability to be viewed in sequence much like a movie is a sequential viewing of individual pictures. This added feature is essential to determine the development of fluid dynamic features such as vortices and shear layers. Additionally, the time-accurate flow visualization system allows examination of events that occur at microsecond intervals to be viewed at much slower rates for human eye examination. Use of state-of-the-art digital cameras allows for immediate inspection of the recorded data as well as the ability to analyze the data digitally.

In the current research, the sudden expansion of a shock wave and its interaction with reflected shock waves, vortices, and shear layers is highly unsteady and time dependent. Single image flow visualization would not allow for clear understanding of the fluid dynamic phenomena involved. Sequential imagery of the flowfield development at specific, known times is essential for correct identification and, more importantly, temporal development of flow phenomena.

3.1 Objective

The goal of this research and, hence, the goal of the optical instrumentation system is to increase fundamental understanding of fluid dynamic phenomena. To that end, an optical instrumentation system is desired that can capture time-resolved imagery of flow structure while in the shock tube expansion device (STED). The ability to capture time accurate data is essential in understanding the process for which the flow structure has evolved (i.e., development of a vortex or shear layer). In the current research, the sudden expansion of a shock wave and its interaction with reflected shock waves, vortices, and shear layers is highly unsteady and time dependent. Single image flow visualization would not allow for clear understanding of the fluid dynamic phenomena involved. Sequential imagery of the flowfield development at specific, known times is essential for correct identification and, more importantly, temporal development of flow phenomena.

3.2 Flow Visualization Systems

Of all the methods available for flow visualization, observation of changes in the refractive index of the fluid media is perhaps most common. The change of refractive index will cause bending of light as it passes through a fluid. These changes can then be recorded optically on film or a digital camera's charge-coupled–device (CCD).

The phenomenon of interest within a flowfield (e.g., shock waves, boundary layers, shear layers, etc.) usually involves changes to the fluid's density (ρ), which according to equation 3.1, is directly related to the refractive index given as (Fuller, 1997)

$$n - 1 \approx k\rho. \tag{3.1}$$

Here, n is the index of refraction and k is known as the Gladstone-Dale constant which is a function of the particular fluid medium.

The velocity of light (c) is related to the refractive index (n) by the equation

$$c = \frac{1}{n} c_o \tag{3.2}$$

where c_o is the speed of light in a vacuum.

The optical effects brought about by local changes in density can be made visible by three general methods:

- *Shadowgraph* method in which the optical response is to a rate of change of density gradient along a distance x (i.e., $d^2\rho/dx^2$).

- *Schlieren* method in which the optical response is to the density gradient (i.e., $d\rho/dx$).

- *Interferometry* in which the optical response is to a uniform change in density (ρ).

3.2.1 Shadowgraph

According to Fuller (1997), shadowgraphs are the least demanding form of flow visualization in terms of apparatus and complexity. Shadowgraphs can be taken with only a short duration light source and a sheet of film or equivalent and give excellent results. Figure 3.1 illustrates a divergent shadowgraph system. For a shadowgraph, in regions where the density gradient is increasing (i.e., $d^2\rho/dx^2$ is positive) the light rays will diverge and the illumination on the film will decrease. The shadowgraph is superior to other techniques where sharp indications of flow discontinuities are required.
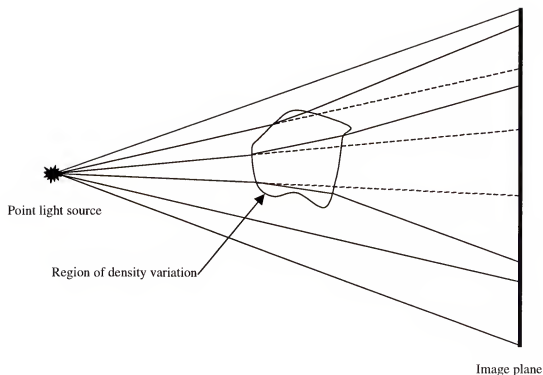
Figure 3.1 Diagram of operation of a basic shadowgraph system

The best results from a shadowgraph result when there is no window between the light source and optical media. Any intervening glass will reduce the quality of detail obtainable and reduce the amount of light that reaches the optical plane. The simplest system with a point light source and sheet of film has no aberrations and the optical apparatus is immune to vibration effects. This technique provides excellent detail for strong disturbances and is ideally suited for ballistic range work (Winchenbach, 1997).

The disadvantages of the direct shadowgraph method are that the experiment needs to be conducted in total darkness and that a large film area is required to accommodate the divergent point light source (Fuller, 1997).

3.2.2 Schlieren Methods

Schlieren methods have been documented over the years by a number of sources (Holder and North, 1950, Holder and North, 1963, and Fuller, 1997). Schlieren methods have been used extensively in the study of high speed flows such as in wind tunnels and shock tube facilities. The method was first discovered by Foucault in 1859 to observe defects in glass components. Later, Toepler (1866) pointed out it could be used to show inhomogeneities in air.

3.2.2.1 Knife-Edge Schlieren System

A basic Schlieren system is shown in Figure 3.2. Here, a "slit" light source is collimated through a region of interest, "R", condensed and focused onto an image plane. A knife-edge is placed at the focal point of the condensing lens. Thus, the image plan will show regions of darkness where the incident beam was "blocked" by the presence of the knife-edge and will show regions of brightness where the incident beam was not blocked. The disadvantage of such a system is its directional dependence. That is, only those changes is density that refract the light normal to the knife edge will be seen at the image plane. However, in most shock tube or wind tunnel applications where density gradients are dominant in one direction this system is adequate.

Limitations of the knife-edge Schlieren method are pointed out by Speak and Walters (1950) and improvements to the traditional Schlieren system are outlined by Taylor and Waldram (1933).
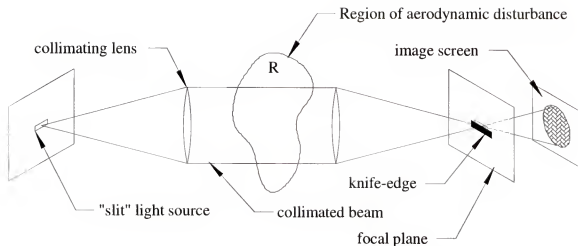
Figure 3.2 Schematic of a traditional Schlieren system with a knife-edge filter

3.2.2.2 Circular Cut-off Schlieren System

A simple improvement to the knife-edge Schlieren system is to use a circular cut-off filer vice a knife-edge. This system is shown in Figure 3.3. Here the slit source of light is replaced with a point source and the corresponding filter at the image plane is an opaque "dot." The advantage of this system is that density gradients in any direction will be observed on the image plane. This system will be expanded upon in greater detail in Section 3.3.

3.2.2.3 Color Schlieren System

Schlieren imagery in color can be obtained by a variety of methods. Regardless of the method used, the basic premise is to use hues of color to identify density gradient strength and/or direction. Kleine and Grönig (1991) state that in the analysis of complex flow structure, monochrome pictures may be unclear but note, however, that black-and-white systems can be made more sensitive.
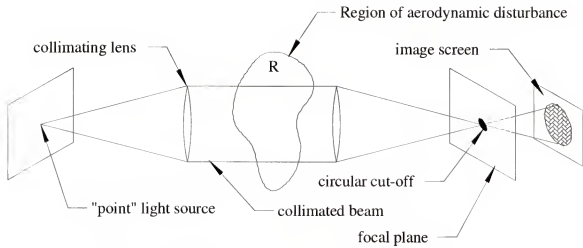
Figure 3.3 Schematic of a Schlieren system with circular cut-off filter

A color Schlieren system is arranged identical to the circular cut-off system in Figure 3.3. However, in place of the opaque cut-off a transparent color "wheel" is used as shown in Figure 3.4. This color wheel is the critical element in the system. The resulting imagery from this filter will allow for identification of density gradient direction. For example, a hue of "blue" would indicate a gradient vertically down while a hue of yellow would indicate a vertically up density gradient.

Kleine and Grönig (1991) point out however that it is difficult to determine the strength of the gradients, as color saturation is hard to estimate. High sensitivity Schlieren systems will best be left to black-and-white methods although color systems have an enhanced aesthetic value. As with the circular cut-off, this two-dimensional method does allow one to record

Figure 3.4 Diagram of filter used for color Schlieren imagery

density gradients in all directions on a single picture. A limiting factor for this system is the light source.

Additionally, there are higher demands on the optical components of the color Schlieren setup as well as the additional complexity of developing and reproducing the color images which has kept many from using this system.

3.2.3 Interferograms

While both the shadowgraph and Schlieren method make use of light deflection in a compressible fluid media, the associated phase alteration is the basic effect for visualization with an interferometer (Merzkirch, 1974). In a classical Mach-Zender system, the phase of an undisturbed light ray is compared with that of a ray that has passed through a compressible media. The subsequent interference of the reference and disturbance beams is recorded for flowfield visualization. As was previously mentioned, this arrangement gives sensitivity directly related to the density. A basic arrangement for an interferometric system is given in Figure 3.5. Usually, the reference and disturbed beam originate from the same light source and traverse the same optical path length. The main drawback of this system is the optical complexity required for visualization and the sensitivity of the components to vibration.

Many improvements to the basic interferometer system have occurred through the years (Smartt and Steel, 1974, Anderson and Taylor, 1982, Loomis et al., 1991, Watanabe et al., 1991, and Dillmann et al., 1998) but, again, the complexity of these systems make it difficult in application.
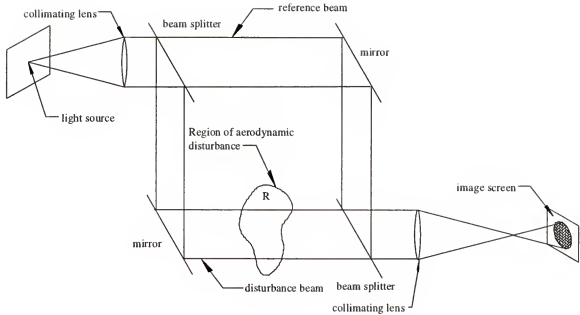
Figure 3.5 Schematic of an interferogram system

3.2.4 Other Methods

Other methods for flow visualization focus on using laser-spectroscopic techniques in which actual species within the flow are imaged. McKenzie et al. (1992) present a thorough review of such modern techniques. The advantage of such systems, such as laser absorption, laser-induced fluorescence, Rayleigh scattering, and Raman scattering is that species tracking can be accomplished as well as measurement of selected population density.

The disadvantages of these systems are that they are complex, are expensive to implement, and may require optical access that cannot be achieved.

3.2.5 Method Comparison

Table 3.1 presents the various methods discussed along with their advantages and disadvantages. One of the best visualization "values" in the table is the Schlieren system with the circular cut-off. The advantages are that it is a simple system to implement, is stable (i.e., not susceptible to vibration), and robust. The information gathered from the system will meet this research needs.

Table 3.1 Comparison of flow visualization methods

	Sensitive to:	Difficulty	Cost	Advantages	Disadvantages
Shadowgraph	$d^2\rho/dx^2$	Easy	$	Simple, easy to implement	Not very sensitive
Schlieren:					
Knife-edge	$d\rho/dx$	Easy	$	Simple, easy to implement, more sensitive	Directional dependence
Circular cut-off	$d\rho/dx$	Easy-difficult	$	Simple, easy to implement, more sensitive	Gradients in all directions
Color	$d\rho/dx$	Difficult	$$	Identify density gradient direction	Gradients in all directions, difficult to arrange
Interferogram	ρ	Difficult	$$$	Direct measure of density field	Difficult to implement, expensive
Other:					
Laser Absorption	Specific species	Hard	$$$$	Direct species measurement	Difficult to implement, very expensive
Laser Induced Fluorescence	Specific species	Hard	$$$$	Direct species measurement	Difficult to implement, very expensive
Rayleigh scattering	Specific species	Hard	$$$$	Direct species measurement	Difficult to implement, very expensive
Raman scattering	Specific species	Hard	$$$$	Direct species measurement	Difficult to implement, very expensive

3.3 Imaging System for Current Research

For the current research, a circular cut-off Schlieren system will be employed for detailed, time-accurate qualitative data. The decision to use the circular cut-off Schlieren system as opposed to an interferometric system is based upon the observation that more qualitative information can be gleaned from the Schlieren imagery versus the interferograms. Interferograms of the flow structure would be a natural follow-on to this data once the qualitative flow features are fully understood. A detailed analysis to highlight the advantages of the circular cut-off Schlieren system will be detailed in the following sections.

3.3.1 Knife-edge vs. Circular Cut-off Schlieren Imagery

A "traditional" Schlieren system was depicted in Figure 3.2. Here a light source emanates from a slit and is expanded and collimated through a region of interest R. The beam is then focused on an image screen for viewing/recording. At the focal plane, an image of the slit is present and a knife-edge is placed as shown which obscures part of the beam on the image screen.

If the density of the medium within R is uniform, then even illumination of the image screen will occur. If there exists some regions of variable density due to aerodynamic disturbances, then changes to the refractive index, as given by equation 3.1, will occur; "bending" the otherwise collimated light rays that pass through the disturbed region. What results from the sum total of all light rays passing through the region R is a picture of the refractive index gradients or medium density changes that occur. Shafer (1949), through a rigorous analysis, shows that the optimum knife-edge position for this

arrangement is on the optic axis. One disadvantage of this system is that only density gradients perpendicular to the knife-edge will be seen.

In contrast, a circular cut-off Schlieren system was shown in Figure 3.3. Here, the source is a "point source" and the corresponding image at the focal plane is a point as well. It is here that a circular cut-off filter is placed. The advantage of this system is that changes in density gradient well be seen in all directions.

To better understand the advantage of the current circular cut-off Schlieren system first return to the "traditional" knife-edge system. Figure 3.6a illustrates the image of the light source in the focal plane for the knife-edge system. It is here that the knife-edge is placed. Figure 3.6a also depicts the image of the light source for a beam that has undergone a deflection due to a density change within the region of interest. The amount of shift of the beam in the direction parallel to the knife-edge is given as Δx and the shift perpendicular is given as Δy. Displacements parallel to the knife-edge will produce no effect on the image screen (Holder and North, 1963). Displacements perpendicular to the knife-edge will produce a picture of the refractive index gradients in the image screen. In most wind tunnel applications this system is sufficient as density variations occur primarily in one direction. However, in the current apparatus, density will vary in equal magnitudes in all directions.
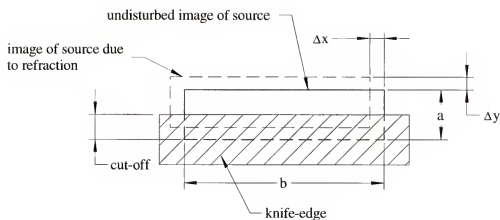
a) Knife-edge cut-off
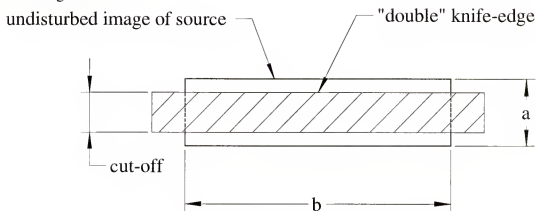
b) Double knife-edge cut-off
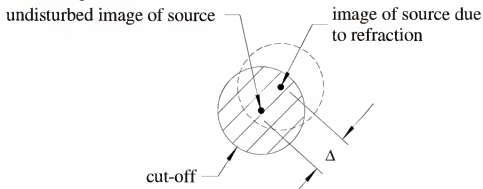
c) Circular cut-off

Figure 3.6 Schlieren system focal-plane filter schematics

Figure 3.6b illustrates an improved knife-edge technique called a "double knife-edge" (Stolzenburg, 1965). The double knife-edge is used to increase the sensitivity of the Schlieren image. According to Stolzenburg (1965) the sensitivity of a traditional Schlieren system can be expressed as

$$S = \frac{dC}{\phi} = \frac{f}{a}$$ (3.3)

where C is the contrast, ϕ is the deflection angle of the light beam due to refraction, f is the focal length of the collimating lenses, and a is the height of the undeflected light source image allowed to pass over the knife-edge (Figure 3.6a). It can then be shown (Holder and North, 1963) that the maximum sensitivity of the system is given by

$$S = \frac{2}{\overline{\phi}}$$ (3.4)

where $\overline{\phi}$ is the range of the angular deflection. Equation 3.4 shows the sensitivity is dependent solely on the angular deflection of the light rays due to variation in density.

The double knife-edge Schlieren system offers improvements over traditional Schlieren systems via the following qualitative analysis (Stolzenburg, 1965). The contrast is defined as

$$C = \frac{\Delta I}{I}$$ (3.5)

where

$$\Delta I = \frac{Bb\phi}{M^2 f}$$ (3.6)

and where I is the intensity of the undeflected light source, B is the brightness of the source, b is the length of the slit, and M is magnification. Therefore we see the contrast is directly related to ϕ which is constant for a particular flow disturbance. However, the intensity, I, is given as

$$I = \frac{Bba}{M^2 f^2} \tag{3.7}$$

which varies directly with a. If a is reduced to a_1 by the substitution of the double knife-edge such that $0 < a_1 < a$ then the intensity I will be reduced to I_1 such that $0 < I_1 < I$ thus increasing the contrast C via equation 3.5. The sensitivity will also be increased due to the reduction of a via equation 3.3.

Figure 3.6c illustrates the image of the point light source at the focal plane for the current system. Here, it is seen the circular cut-off which demonstrates its ability to observe deflections due to refraction in any direction. Comparing Figure 3.6b with that of 3.5c, it is evidently seen that the circular cut-off filter for a point light source is identical to that of the double knife-edge filter for the slit light source of traditional Schlieren systems. Subsequently, this analysis that shows improved sensitivity for the double knife-edge system is analogous to that of the circular cut-off system.

3.3.2 Optical Arrangement

The flow visualization system employed in the current work takes advantage of the increased sensitivity of the circular cut-off Schlieren system previously described. This was because the changes in density gradient varied equally in all directions in the experimental apparatus. Additionally, the Schlieren system afforded better capability to visualize and track flowfield structure.

The experimental system used to gather the current data is similar to the schematic depicted in Figure 3.3. Here, the light source is a continuous wave 100 mW, frequency doubled YAG laser operating at 532 nm wavelength. The laser output is spatially filtered to remove unwanted beam non-uniformity. A 1.5 m focal length, spherical lens is used to collimate the 150 mm diameter optical beam through the test region. The optical beam is then focused by a second 1.5 m focal length lens onto the circular cut-off filter discussed previously. For this filter, we are using 20 μm to 5 mm absorptive dots which block those portions of the optical beam that are not refracted in the test chamber.

3.4 Digital Camera

The last component of the optical system is a Hadland 468 framing camera (Honour, 1994). This unit has eight individual image intensifiers and CCD detectors to allow the capture of eight time-resolved images. Although the camera supports inter-frame times of 30 nanoseconds, we are operating the device with between 5-35 μs between images. After the event is complete, the images are sent via fiber-optic link to a computer where they can be image enhanced or viewed in a time-sequential movie format.

Important parameters of the digital camera that can be set include "gain" and "exposure time." Gain is a multiplier of the image signal upon the CCD detector. Increasing the gain serves to intensify the image's brightness. Exposure time is the amount of time the image is integrated upon the CCD detector. Short exposure times are required to obtain the "stop action" required to image such a highly transient event. Both gain and exposure times are varied to obtain optimal results.

Although the use of the digital camera offers advantages in data acquisition, quantitative analysis of the images is not practical. This is due to the fact that the light beams go through individual, non-linear image intensifiers before they arrive at each of the CCD chips. Photographic densitometry (Holder and North, 1963) may be employed to obtain quantitative data but the process is difficult and the accuracy low. This is exacerbated by the fact that the gray-scaling within the camera system is poor.

3.5 Summary

A review of flow visualization methods clearly shows that a Schlieren system that uses a circular cut-off filter is ideal for the flowfield of a confined shock wave expansion. Other imagery methods are applicable and can provide additional insight but also tend to increase the cost and complexity of the system. The circular cut-off Schlieren system will be used to capture time-accurate flow visualization data for this research herein. A circular cut-off filter with a point light source has been qualitatively shown to provide greater sensitivity and detail to density gradients, especially in all directions, than traditional knife-edge Schlieren systems. A digital framing camera is used to capture the time accurate flow development within the shock tube expansion device. The current system is ideal for determination of flow features and their development in time.

CHAPTER 4
EXPERIMENTAL DATA

This chapter will discuss the results obtained from the shock tube expansion device using the flow visualization system described in the preceding chapters. The first section of this chapter is dedicated to the presentation of experimental flowfield imagery. An analysis of the optical imagery that shows the advantage of the current flow visualization system follows. The pressure data obtained along the wall of the expansion chamber is presented next. These sections will provide a better understanding of the experimental data and its usefulness. Comparisons to numerical data will be presented once the experimental data obtained is thoroughly analyzed.

4.1 Experimental Results

Although numerous tests have been conducted in the shock tube expansion device, this work will concentrate on only three specific test cases. Namely, the results for shocks studied in the device with nominal Mach numbers of 1.5, 2.0, and 3.0 with dry air as the test gas. Table 4.1 lists the conditions and results of all trials conducted in which the desired flowfields were achieved.

The experimental sequences of flow visualizations for the cases of Table 4.1 are presented in Figures 4.1 through 4.15. These time accurate data clearly depict the evolution of the sudden expansion of a shock wave within the shock tube expansion device. Within each image of Figures 4.1 to 4.15 is a grid of fiducial wires. These

fiducials are physically separated by 25 mm in each direction. When measured data such as shock or vortex location are presented in this work, the fiducials were used to correctly scale distances in both the x- and y-directions.

As given in Table 4.1, Trials 1-11 were conducted in dry air to achieve a nominal Mach 1.5 shock in the device. Most of these trials were conducted to better understand the performance of the shock tube expansion device. Trial 1 is considered a "baseline" for the Mach 1.5 case. Trial 2 was performed to understand the effect of the double-diaphragm on the shock wave (see discussion of Section 2.2.3.1). Trials 3 and 4 extend the baseline imagery data beyond that of the baseline case. Trial 5 was performed to validate that the shock imagery is independent of the driver gas and pressure. Trials 6 through 9 repeat the baseline trial conditions with variations to the circular cut-off. These results will be discussed in a following section. Trial 10 presents the baseline conditions using a knife-edge filter vice the circular cut-off filter. These results will also be discussed in a following section. Finally, Trial 11 repeats the baseline conditions for the new shock tube as discussed in Section 2.2.3.3.

Trials 12 through 14 present the baseline data for the Mach 2.0 case. The three trials capture the evolution of the flow structure over a wide time domain. Trial 15 presents the case for a Mach 3.0 shock in dry air. Only one shot is presented as increased sensitivity of the optical data is seen for the higher Mach number cases. This will be discussed in greater detail later in this work.

A description of the flow structure for a typical image is given in Figure 4.16. Here is seen the shock front as it expands from the shock tube, the formation of the

vortices and shear layer due to the sudden expansion at the sharp corner, the reflected shock and its interaction with these vortices. The fiducial grid is also highlighted.

The time-accurate evolution of the flowfield can be described in the following manner. The shock wave travels down the square shock tube and enters the shock tube expansion device. Here it encounters a sudden area change on opposite sides of the shock tube while there is no expansion in the other direction. The planar shock transitions to a cylindrical shock as it travels through the shock tube expansion device. Two opposing vortex cores are formed at the corner of the area expansion and are convected down the shock tube expansion device and expand outward slightly. Large gradients in density are observed in the vortex region. The fluid originally in the shock tube, having an induced velocity due to the traversing of the shock wave, now enters the shock tube expansion device and begins to form a blast jet. The shock wave expands until it encounters the wall of the shock tube expansion device and is reflected. This reflected shock then interacts with the vortex cores formed at the area change. Here, the reflected shock wave splits as described by Jiang et al. (1997).

Similar flow structure is seen for all three cases studied (Mach 1.5, 2.0, and 3.0) however some differences are noted. For instance, the vortex cores in the higher Mach number flows expand out further into the shock tube expansion device. The formation of the starting jet is also different for each case. In Case 3 large areas of density change are present. This is because the higher incident shock Mach number causes greater changes and, hence, gradients in the density field.

Table 4.1 Summary of experimental trials conducted in shock tube expansion device

Trial number	Flow visualization Figure number	Pressure data Figure number	Size of circular cut-off filter (mm)	Time delay of first image after arrival at transducer #2	Time delay between images	Driver gas/pressure (Pa)	Driven gas/pressure (Pa)	p4/p1	Velocity of shock wave (w) in shock tube (m/sec)	Shock Mach number within tube	Velocity of shock wave (w) at entrance to expansion chamber (m/sec)	Shock Mach number at entrance of expansion chamber	Comments
Case 1: Mach 1.5 in air													
1	4.1	4.20	3.138	800µS	35µS	Argon/4.137E6	Air/4.137E5	10.00	520.7	1.509	480.8	1.390	Baseline Mach 1.5 trial using double-diaphragm initiation
2	4.2	4.21	1.772	800µS	35µS	Argon/4.944E6	Air/4.137E5	11.95	522.4	1.514	-	-	Use overpressure to initiate
3	4.3	NA	1.772	1,100µS	35µS	Argon/4.137E6	Air/4.137E5	10.00	NA	NA	-	-	Extension of baseline data to increased times
4	4.4	NA	1.772	1,100µS	35µS	Argon/4.137E6	Air/4.137E5	10.00	NA	NA	-	-	Extension of baseline data to increased times
5	4.5	4.22	1.772	800µS	35µS	Air/7.481E6	Air/4.137E5	16.95	523.5	1.517	-	-	Effect of driver gas on shock structure
6	4.6	4.23	1.772	800µS	35µS	Argon/4.137E6	Air/4.137E5	10.00	509.8	1.478	-	-	
7	4.7	4.24	1.000	800µS	35µS	Argon/4.137E6	Air/4.137E5	10.00	523.5	1.517	-	-	Effect of filter size of imagery
8	4.8	4.25	0.316	800µS	35µS	Argon/4.137E6	Air/4.137E5	10.00	523.5	1.517	-	-	
9	4.9	4.26	3.798	800µS	35µS	Argon/4.137E6	Air/4.137E5	10.00	516.6	1.497	-	-	
10	4.10	4.27	NA	800µS	35µS	Argon/4.137E6	Air/4.137E5	10.00	524.9	1.521	-	-	Knife-edge filter used
11	4.11	4.28	2.358	910µS	40µS	Argon/4.137E6	Air/4.137E5	10.00	518.0	1.502	-	-	New shock tube used
Case 2: Mach 2.0 in air													
12	4.12	4.29	1.000	650µS	30µS	Nitrogen/3.310E6	Air/1.014E5	32.70	665.4	1.909	658.1	1.910	Baseline Mach 2.0 trial
13	4.13	4.30	1.772	650µS	80µS	Argon/4.826E6	Air/1.724E5	28.00	684.5	1.984	-	-	Extension of baseline data to greater times
14	4.14	4.31	1.772	740µS	30µS	Argon/4.826E6	Air/1.724E5	28.00	683.3	1.981	-	-	Extension of baseline data to greater times
Case 3: Mach 3.0 in air													
15	4.15	4.32	1.000	425µS	15µS	Helium/4.826E6	Air/1.014E5	47.60	1034.5	3.016	992.8	2.880	Baseline Mach 3.0 trial

a) 0 µs

b) 35 µs

c) 70 µs

d) 105 µs

e) 140 µs

f) 175 µs

g) 210 µs

h) 245 µs
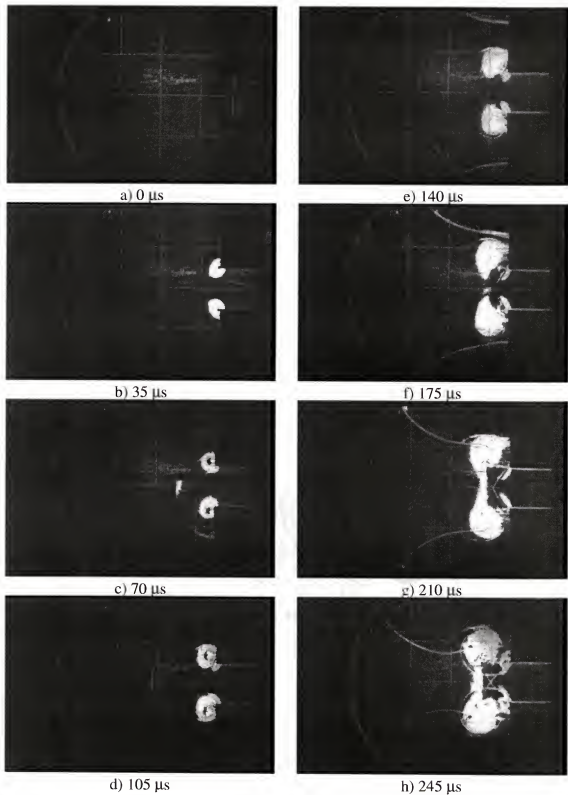
Figure 4.1 Baseline time accurate flow visualization imagery for Trial 1 with initiation via double diaphragm: Mach 1.5 in air

a) 0 µs

b) 35 µs

c) 70 µs

d) 105 µs

e) 140 µs

f) 175 µs

g) 210 µs

h) 245 µs
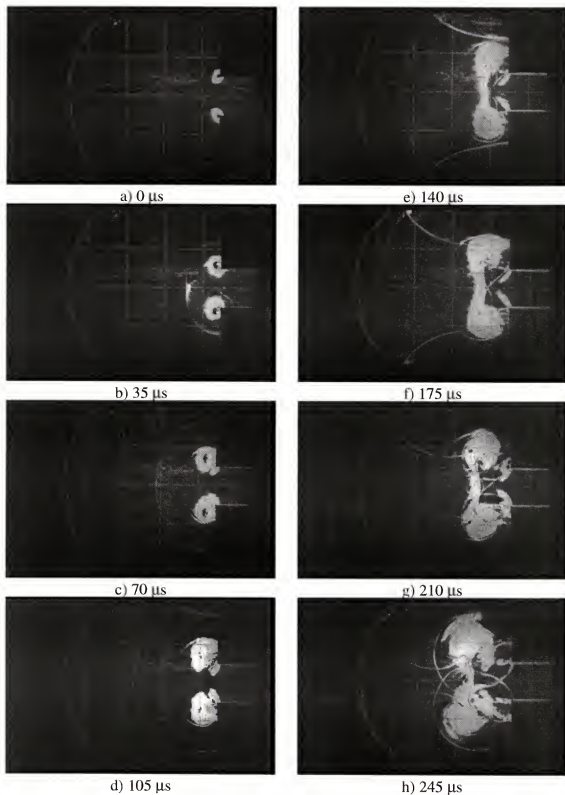
Figure 4.2 Time accurate flow visualization imagery for Trial 2 with initiation of shock wave via overpressure: Mach 1.5 in air

a) 0 µs

e) 140 µs

b) 35 µs

f) 175 µs

c) 70 µs

g) 210 µs

d) 105 µs

h) 245 µs
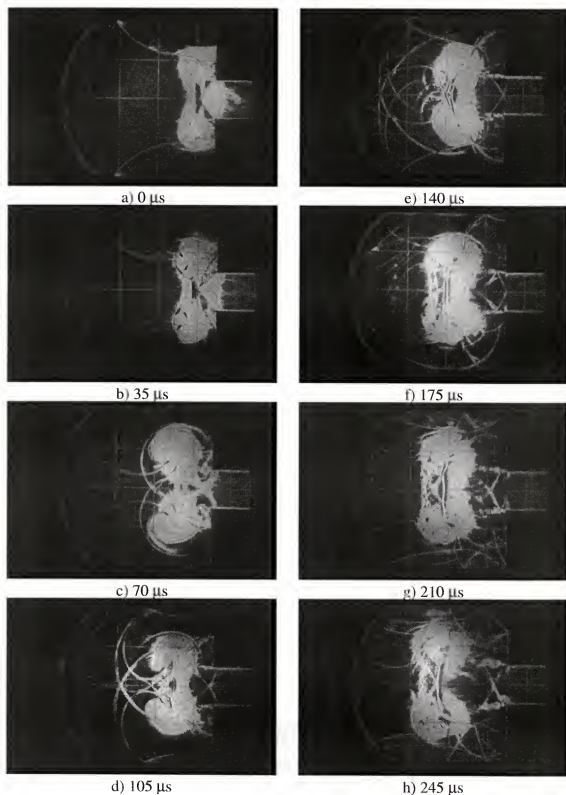
Figure 4.3 Flow visualization imagery for Trial 3 which is extension of baseline imagery data to greater times: Mach 1.5 in air

a) 0 µs

e) 140 µs

b) 35 µs

f) 175 µs

c) 70 µs

g) 210 µs

d) 105 µs

h) 245 µs
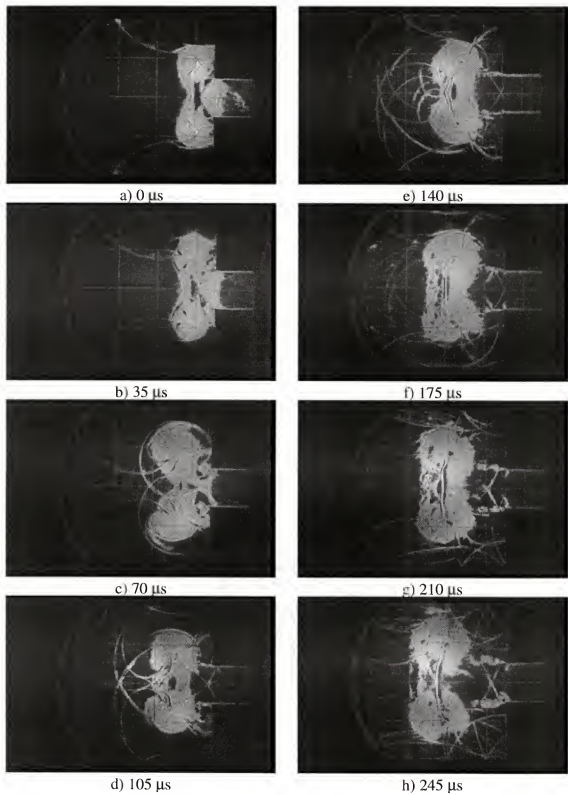
Figure 4.4 Flow visualization imagery for Trial 4 which is extension of baseline imagery data to greater times: Mach 1.5 in air

a) 0 µs

e) 140 µs

b) 35 µs

f) 175 µs

c) 70 µs

g) 210 µs

d) 105 µs

h) 245 µs
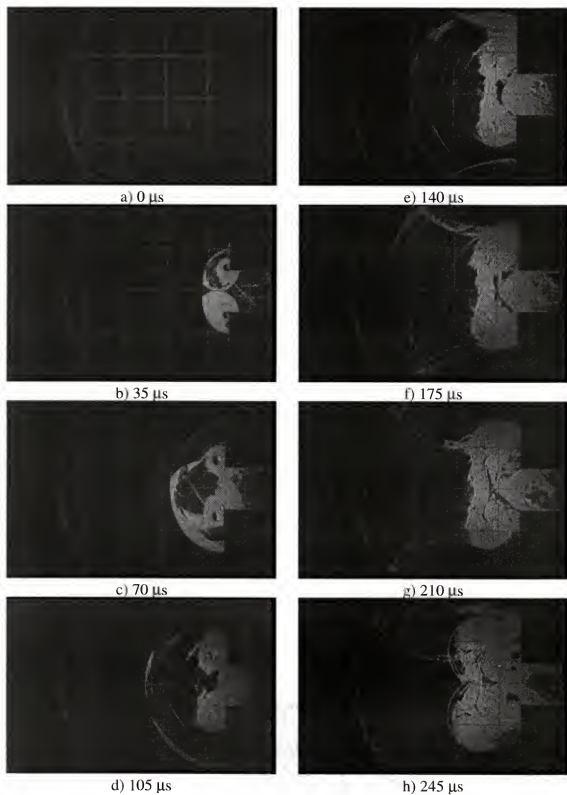
Figure 4.5 Flow visualization imagery for Trial 5 with air as driver gas: Mach 1.5 in air

a) 0 μs

b) 35 μs

c) 70 μs

d) 105 μs

e) 140 μs

f) 175 μs

g) 210 μs

h) 245 μs
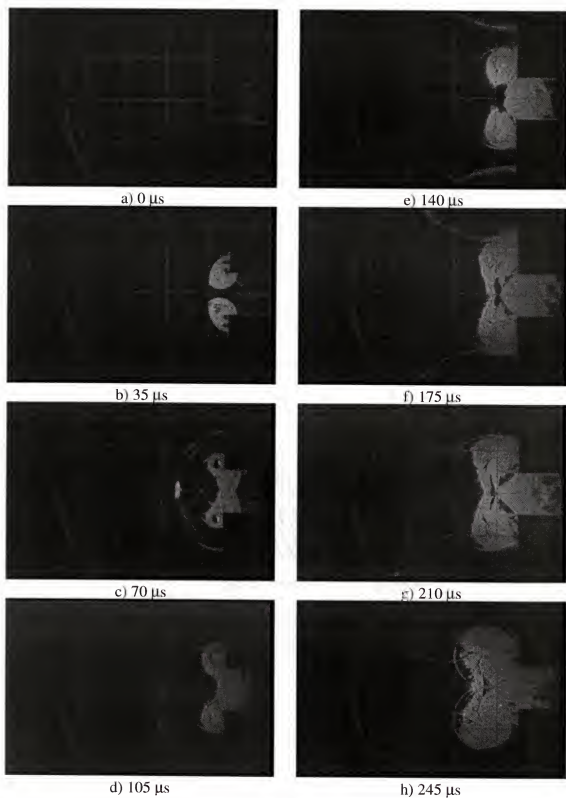
Figure 4.6 Flow visualization imagery for Trial 6 which uses a circular cut-off filter of 1.7716 mm: Mach 1.5 in air

a) 0 μs

b) 35 μs

c) 70 μs

d) 105 μs

e) 140 μs

f) 175 μs

g) 210 μs

h) 245 μs

Figure 4.7 Flow visualization imagery for Trial 7 which uses a circular cut-off filter of 1.000 mm: Mach 1.5 in air

a) 0 µs

e) 140 µs

b) 35 µs

f) 175 µs

c) 70 µs

g) 210 µs

d) 105 µs

h) 245 µs
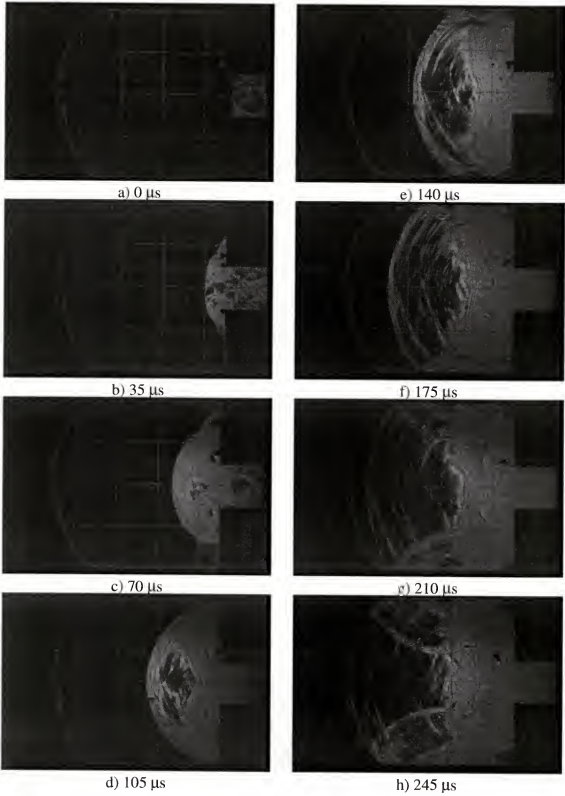
Figure 4.8 Flow visualization imagery for Trial 8 which uses a circular cut-off filter of 0.3164 mm: Mach 1.5 in air

a) 0 μs

b) 35 μs

c) 70 μs

d) 105 μs

e) 140 μs

f) 175 μs

g) 210 μs

h) 245 μs
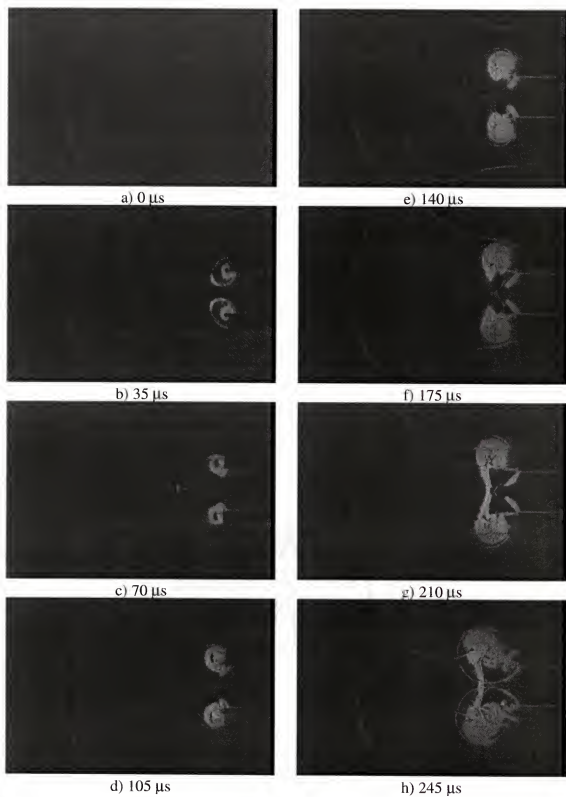
Figure 4.9 Flow visualization imagery for Trial 9 which uses a circular cut-off filter of 3.7975 mm: Mach 1.5 in air

a) 0 μs

b) 35 μs

c) 70 μs

d) 105 μs

e) 140 μs

f) 175 μs

g) 210 μs

h) 245 μs

Figure 4.10 Flow visualization imagery for Trial 10 which uses a knife-edge filter: Mach 1.5 in air

a) 0 µs

e) 160 µs

b) 40 µs

f) 200 µs

c) 80 µs

g) 240 µs

d) 120 µs

h) 280 µs
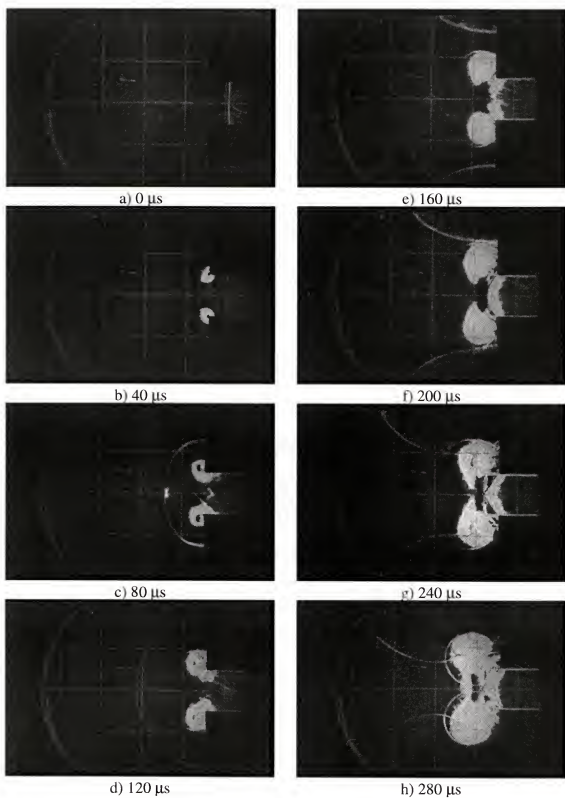
Figure 4.11 Flow visualization imagery for Trial 11 in which the new shock tube is used: Mach 1.5 in air

a) 0 μs

e) 120 μs

b) 30 μs

f) 150 μs

c) 60 μs

g) 180 μs

d) 90 μs

h) 210 μs
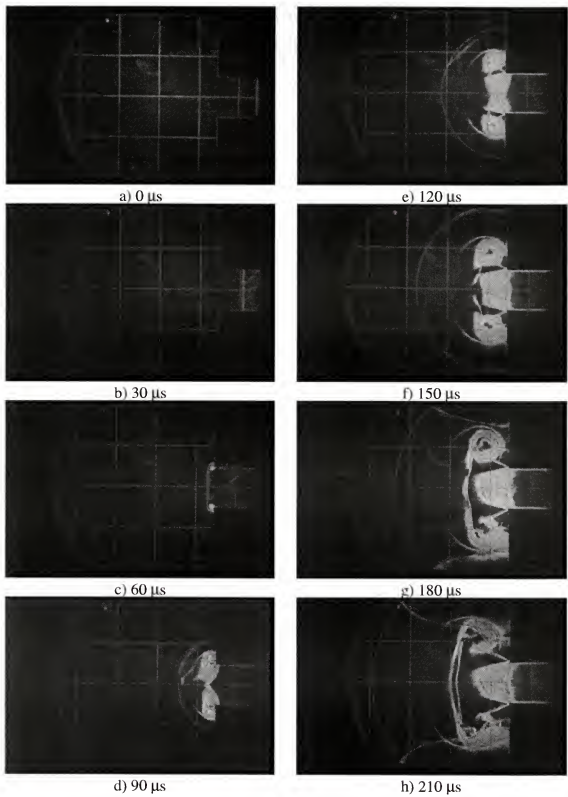
Figure 4.12 Baseline time accurate flow visualization imagery for Trial 12: Mach 2.0 in air

a) 0 µs

e) 240 µs

b) 60 µs

f) 300 µs

c) 120 µs

g) 360 µs

d) 180 µs

h) 420 µs
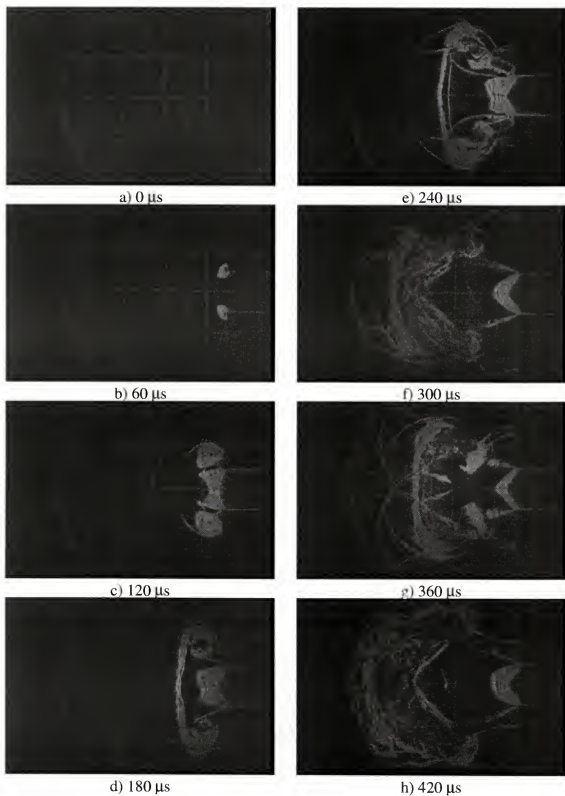
Figure 4.13 Flow visualization imagery for Trial 13 which is extension of baseline imagery data to greater times: Mach 2.0 in air

a) 0 µs   e) 120 µs

b) 30 µs   f) 150 µs

c) 60 µs   g) 180 µs

d) 90 µs   h) 210 µs
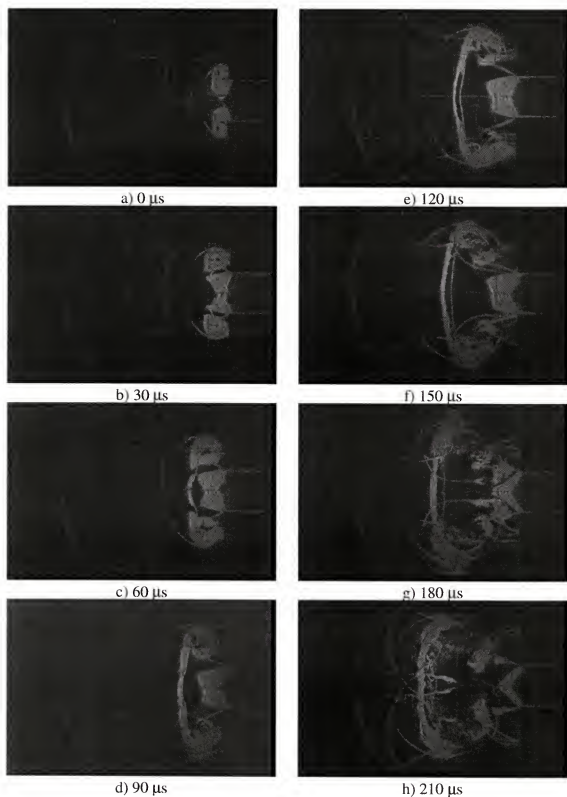
Figure 4.14 Flow visualization imagery for Trial 14 which is extension of baseline imagery data to greater times: Mach 2.0 in air

a) 0 µs

b) 15 µs

c) 30 µs

d) 45 µs

e) 60 µs

f) 75 µs

g) 90 µs

h) 105 µs
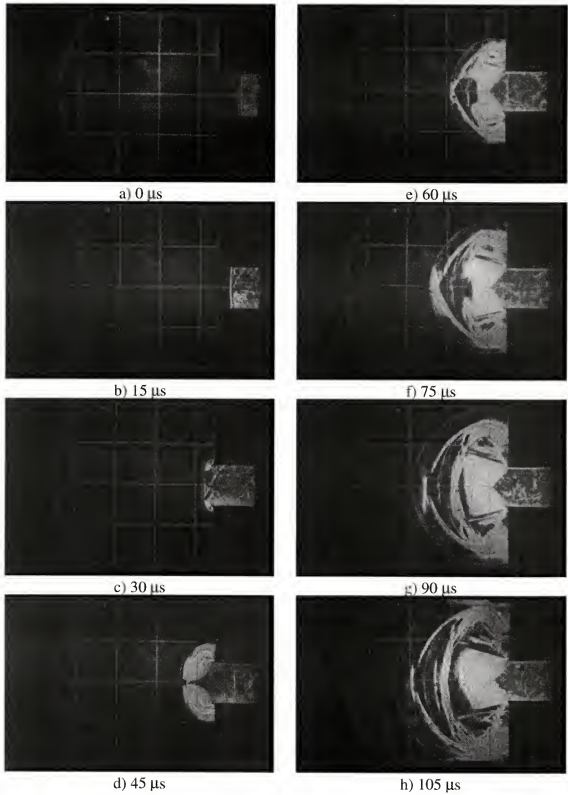
Figure 4.15 Baseline time accurate flow visualization imagery for Trial 15: Mach 3.0 in air
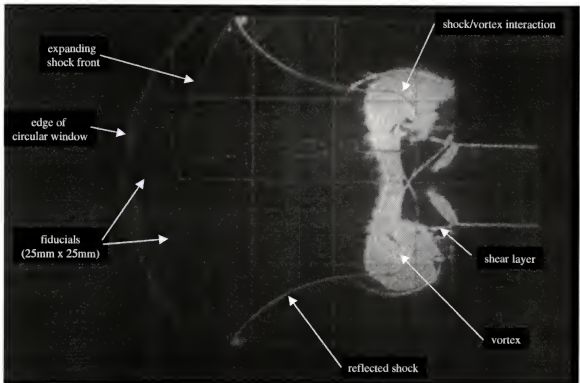
Figure 4.16 Detail of typical flow visualization data; Trial 2, frame g

The measured speeds of the experimental shock waves reported upon in Table 4.1 were determined via two methods. The first method uses data from the two pressure transducers located within the shock tube itself. Figure 2.6 indicates the location of four pressure transducers. The measured speed within the shock tube is based upon the time difference of the shock front between the #1 and #2 transducers. These transducers, roughly centered in the shock tube, are physically separated by 390.5 mm. The arrival time of the shocks are recorded via standard laboratory oscilloscope. The determination of time difference between shock arrival times for each transducer is straightforward. The second method for measuring shock speed, and perhaps more relevant to the coming analysis is the measure the shock front locations in the imagery at or near the sudden expansion. That is, based upon the first few images of the shock entering the shock tube

expansion device chamber, the relative locations of the shock front can be measured based upon the fiducials. The timing between frames is known as well so the speed can easily be determined.

It is seen from the data of Table 4.1 that the shock speed decreases slightly from within the shock tube to the entrance of the shock tube expansion device. However, this is to be expected as there is attenuation of the shock front as it passes through the tube itself.

As previously mentioned, this optical data were recorded via the Hadland 468 digital camera. Triggering for the camera was accomplished by programming a time delay from the arrival of the shock wave at the #2 pressure transducer located in the shock tube. Hence, the experimental pressure data uses the arrival of the shock front at the #2 pressure transducer as time 0.0. The entrance of the shock tube expansion device is roughly 460 mm from the second pressure transducer. Based upon the predicted shock strength, a time delay was calculated for each trial based on this distance. Although this technique is crude, repeatable results were obtained. However, exact placement of the shock front within the shock tube expansion device is difficult. Hence, the initial images shown in Figures 4.1 through 4.15 have the shock waves within the shock tube before they are subjected to the sudden expansion and, thus, this location varied from trial to trial.

4.1.1 Time-resolved Imagery

Figure 4.1 represents a typical, time-resolved, sequence of circular cut-off Schlieren images that show flowfield development within the shock tube expansion

device. This shock wave was created by 4.137 x 10^6 Pa (600 psi) argon gas in the high pressure reservoir and dry air at 4.137 x 10^5 Pa (60 psi) in the shock tube and expansion chamber. The temperature of each gas was 296K. These initial parameters produce a nominal Mach 1.5 shock that travels down the shock tube and expands in the chamber. Here we see the eight individual images of the flowfield as it develops. The time between images is a constant 35 microseconds. The image exposure time on each CCD within the camera is 100 nanoseconds. When viewed in sequence, one can easily discern flowfield features and development.

4.1.2 Image Analysis

If we examine in detail an individual frame shown in Figure 4.1 we can see the usefulness of the current visualization system. The brighter regions on the image correspond to locations of higher density gradient ($d\rho/dx$). Thus, the shock wave and its reflection show up nicely on the image as strong changes in density exist across a shock. In addition, the slug of fluid that enters the chamber and undergoes change due to the sudden expansion also experiences density changes as is evident in Figure 4.1.

As mentioned, the use of Schlieren systems to obtain direct measurement of density gradients is possible but not practical. We are limited in our ability to get quantifiable data from this or any other Schlieren system since phase information is lost in the non-linear integration of the image on the CCD. For example, we know there is a significant density change across a shock. But if we examine the captured data we see that the fluid on either side of the shock is equally exposed. Although the density gradient due to the shock stands out in the image, exactly how much density change is

present is unknown. Likewise, we see a large area of density gradient in the region of the vortex but the current system is limited it its ability to quantify that change.

However, the current system is extremely useful in its ability to provide excellent qualitative, time-accurate, flowfield structure of a shock expansion process. The current system allows for easy tracking of flowfield features of interest such as shock-vortex interaction.

4.1.2.1 Advantage of Circular Filter

Figure 4.10 presents the eight time resolved images when a knife-edge replaces the current circular cut-off filter. A direct comparison of images produced by the current circular cut-off Schlieren system and a traditional knife-edge Schlieren system is presented in Figure 4.17. A typical circular cut-off Schlieren image captured by the shock tube expansion device is shown in Figure 4.17a. Figure 4.17b is an image captured by the knife-edge system at nearly the same conditions. Although the setup used in Figure 4.17b is not strictly a traditional knife-edge Schlieren (i.e., the light source is not a slit), the resulting image highlights the advantage of the circular cut-off. There are two important things to note about these images. First, because of the knife-edge filter, the density gradients can only be sensed that are perpendicular to the knife-edge (the vertical fiducials cannot even be seen in the region behind the shock). Second, regions that show up as dark on one side of the image will be light on the other and vice-versa. This again is due to the physics of the knife-edge filter.

If we compare flow structure, we see a much "cleaner" image for the circular cut-off system than for the knife-edge system. The advantage of this circular cut-off system as seen here is that the intensity of the imagery is for comparable density gradients in any

direction. That is, with the knife edge system, only the density gradients (or components thereof) that are perpendicular to the knife-edge are visible. Density gradients of equal magnitude by varying in direction will be imaged with different intensity. Clearly, the circular cut-off system is ideal for our research as changes in density gradient will occur in all directions.
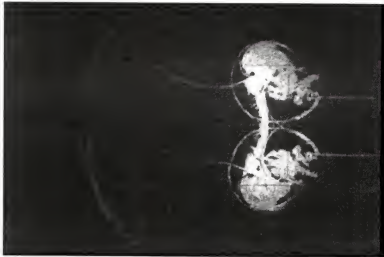
a) Circular cut-off Schlieren image

b) Knife-edge Schlieren image

Figure 4.17 Comparison of Schlieren techniques for flowfield visualization of a Mach 1.5 shock expansion in air within the shock tube expansion device

4.1.2.2 Effect of Filter Size

An added feature to this system is that the size of the filter can be changed to "filter" the level of density gradient that illuminates the image plane. For example, a large circular cut-off may only allow large density gradients, such as shock waves, to be passed through while a small cut-off filter will allow smaller density gradients to be seen. The size of the circular cut-off filter greatly influences the resulting imagery. Figure 4.18 shows selected images from three trials with similar conditions where the filter or "dot" size was varied. We see that with the large filter less detail is seen in the images (i.e., only strong changes, such as the shock, are seen). Smaller than optimum dot size resulted in images that had too much detail. For instance, in Figure 4.18a there are seen wavelets or Mach lines behind the shock fronts. These wavelets can also be seen in the knife-edge imagery of Figure 4.17 b as well. The presence of these features may indicate that less than optimal flow conditions are present in the chamber. However, the ability of the circular filter to customize the level of detail is advantageous. Trial and error results in the optimal filter size being used for the ensuing trials.

4.1.2.3 Effect of Mach Number

Variations of the imagery for different Mach numbers were also observed. Figure 4.19 depicts two shots of different Mach number where the circular cut-off filter remained the same (1 mm) and the initial quiescent pressure in the shock tube expansion device was 101.4×10^3 Pa (14.7 psia). Here it is seen that the higher the Mach number the more sensitivity there is in the imaging system. Stolzenburg (1965) also observed a similar relationship with the double-edge Schlieren system. Here it was observed that as the free stream Mach number was increased, which results in a corresponding increase in
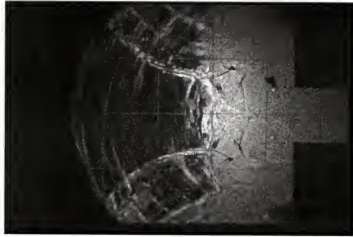
a) 0.316 mm filter, Mach 1.5
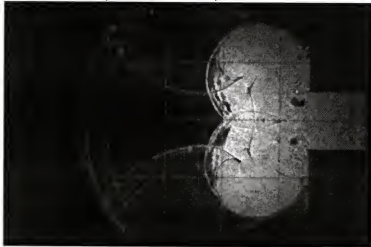
b) 1.00 mm filter, Mach 1.5
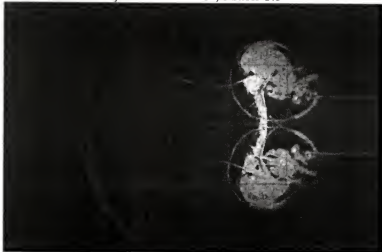
c) 3.797 mm filter, Mach 1.5

Figure 4.18 Comparison of Schlieren images as a function of circular cut-off filter size for a Mach 1.5 shock expansion in air within the shock tube expansion device

density and density gradients, the light source cut-off became more critical. This was also observed in the current system whereby the size of the circular cut-off filter needed to be increased to obtain similar qualitative imagery at higher Mach numbers.
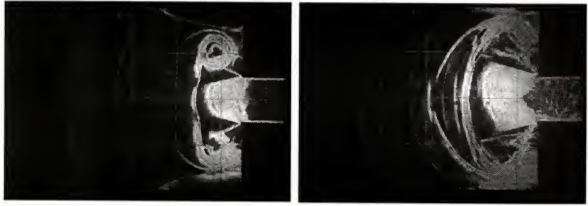
a) Mach 2.0, 1.000 mm filter   b) Mach 3.0, 1.000 mm filter

Figure 4.19 Comparison of Schlieren images as a function of Mach number for a shock expansion in air within the shock tube expansion device

4.1.3 Flowfield Pressure Data

Pressure data gathered from the trials reported upon in Table 4.1 are presented in Figures 4.20 through 4.32. Note that in a few instances there were no pressure data obtained. Also recall the discussion of Section 2.2.3 when reviewing this data. This data is most useful in determining the shock strength via traces from the #1 and #2 transducer. Useful experimental data is given via trace #3 that is recorded in the shock tube expansion device chamber. This data will be used for analysis against numerical data in the following sections.
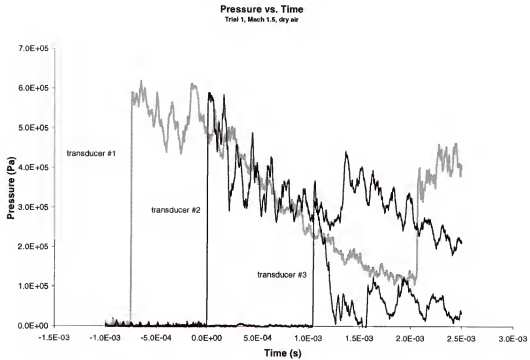
Figure 4.20 Pressure transducer data for Trial 1: Mach 1.5 in air
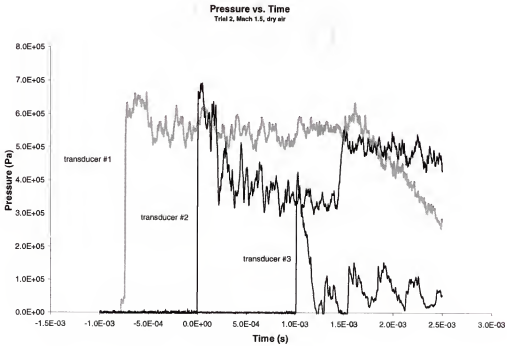
Figure 4.21 Pressure transducer data for Trial 2: Mach 1.5 in air
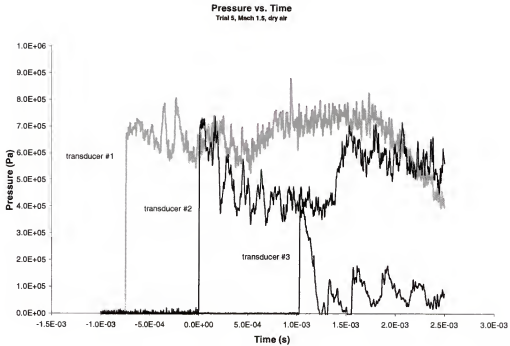
Figure 4.22 Pressure transducer data for Trial 5: Mach 1.5 in air
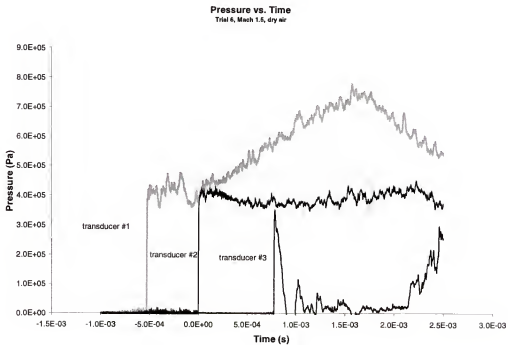
Figure 4.23 Pressure transducer data for Trial 6: Mach 1.5 in air
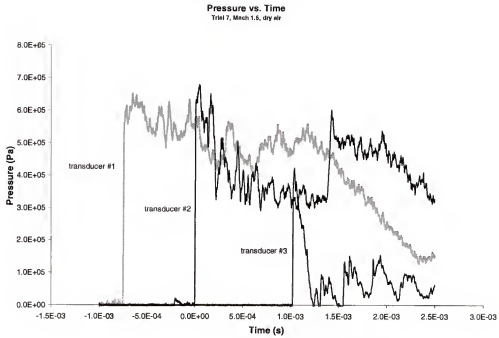
Figure 4.24 Pressure transducer data for Trial 7: Mach 1.5 in air
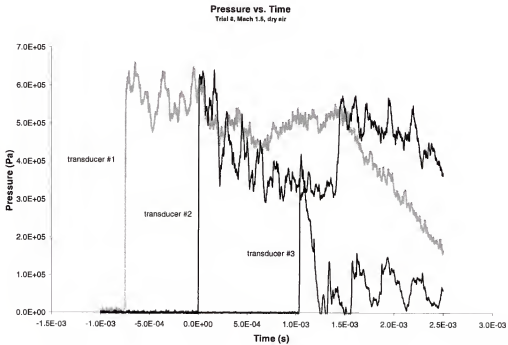
Figure 4.25 Pressure transducer data for Trial 8: Mach 1.5 in air
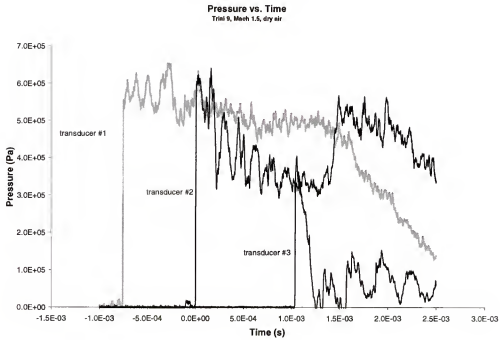
Figure 4.26 Pressure transducer data for Trial 9: Mach 1.5 in air
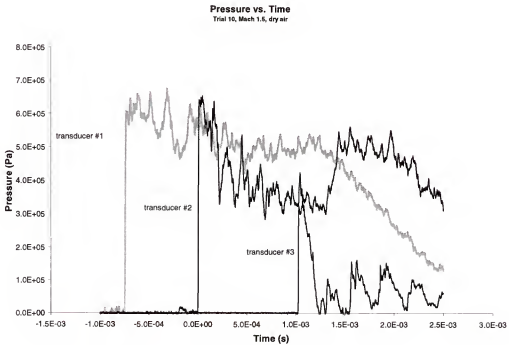
Figure 4.27 Pressure transducer data for Trial 10: Mach 1.5 in air
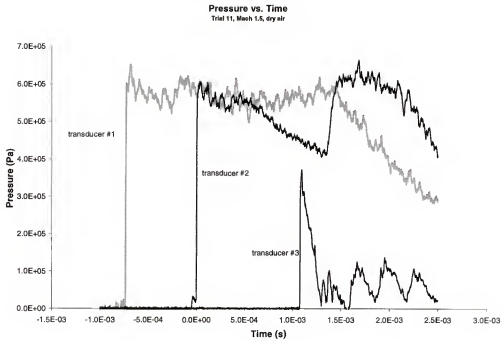
Figure 4.28 Pressure transducer data for Trial 11: Mach 1.5 in air
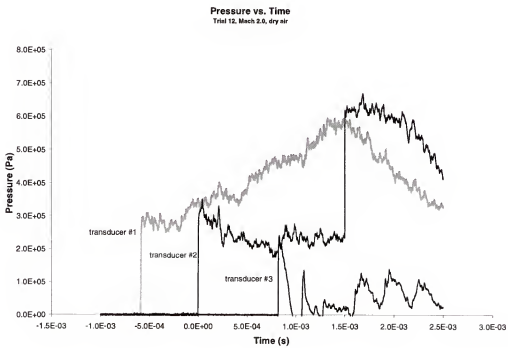
Figure 4.29 Pressure transducer data for Trial 12: Mach 2.0 in air
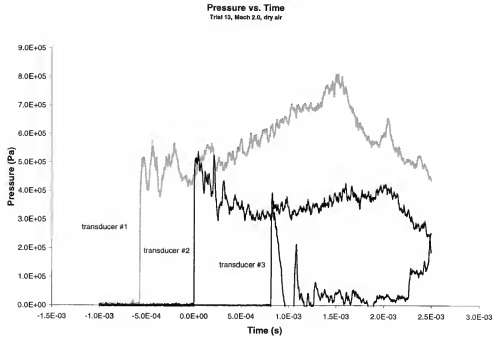
Figure 4.30 Pressure transducer data for Trial 13: Mach 2.0 in air
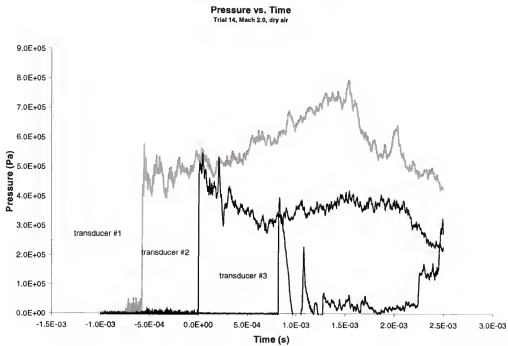
Figure 4.31 Pressure transducer data for Trial 14: Mach 2.0 in air
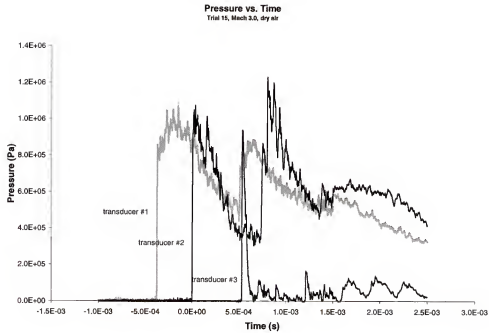
Figure 4.32 Pressure transducer data for Trial 15: Mach 3.0 in air

4.2 Summary

The time resolved imagery gathered during this research was analyzed qualitatively and quantitatively. First, the quality of the data was addressed since circular cut-off Schlieren imagery is not common in the literature. The analysis showed this an extremely useful and economical method for studying the sudden expansion of a shock wave in a confined chamber. This is because the density gradients occur in all directions. Th circular cut-off Schlieren system is inherently sensitive to such. The advantage of using a circular cut-off vs. a traditional knife-edge Schlieren was demonstrated in a direct comparison of the two methods. Namely, the knife-edge method can only visualize density gradients perpendicular to the knife-edge and as such, features of the flow were not even present in the imagery. It was also shown that this method for flow visualization

is sensitive to both filter size and Mach number. The sensitivity to the filter size is advantages as one can determine the optimal size for desired results. For instance, if it is desired to observe only the shock structure and identify shocklets present in the flow a large filter is necessary. However, if the quality of the flowfield is an issue, the filter can be made small to visualize wavelets and/or Mach lines. Care in obtaining the imagery through proper selection of cut-off filter is required for the present research. Otherwise, images may be overwhelmed with small density gradients that mask the salient flow features such as shocklets and contact surfaces.

CHAPTER 5
RESULTS AND DISCUSSION

In this chapter, a detailed analysis of the observed flowfield data will be performed. The analysis will concentrate on Case 1 (Mach 1.5) where a subsonic flow is induced in the flow behind the shock and Case 2 (Mach 2.0) where a supersonic flow is induced behind the shock. Details about the current flowfields will be highlighted and will be compared to prior work and analytical theory. This will validate the usefulness of the current data and will provide a basis for comparisons to numerical work. The comparison to numerical flowfield solutions will be performed in the second section of this chapter. Here, comparisons to both two-dimensional and three-dimensional sudden shock wave expansions will be performed. Agreement and differences with the data sets will be highlighted so conclusions can be drawn.

5.1 Analysis of Data

For the analysis described herein, Case 1 will be for the sudden expansion of a shock wave within a confined chamber with a Mach number of 1.413 and Case 2 will be for a shock with sudden expansion within a confined chamber with a Mach number of 1.908. These two cases correspond to Trial 1 and Trial 12 respectively (see Table 4.1).

5.1.1 Flowfield Evolution

Figure 5.1 depicts a schematic of the flowfield evolution for Case 1. This data was traced from the experimental data presented in Figure 4.1. The images when viewed

on the instrumentation camera allow for detailed review. However, when presented in printed form, the images lose resolution. Therefore it was felt that providing the schematic of the flowfield evolution allowed for easy interpretation of the data. A similar schematic is shown for Case 2 in Figure 5.2. However in this Figure, the first seven frames are schematics of images b-h of Figure 4.12. For completeness, frame e from Figure 4.13 is used for the final frame of Figure 5.2 to show a more complete flowfield evolution.

For Figures 5.1 and 5.2, the geometry of the shock tube expansion chamber is shown along with the fiducial lines discussed earlier. The "thick" lines represent the shock wave while the "thinner" lines are used to trace around the vortices and other structure of the expanding flowfield. The "dots", where present, represent the vortex core location and are only shown in those images where the core is clearly seen. The advantage of these schematic images is that features like shock-vortex interaction can be more clearly seen.

Because the flowfield is forced to expand about a 90^0 corner, the expanding shock wave is not of constant strength during the expansion. The curvature of the shock causes a variation strength along the shock front which imparts variations in the pressure and density jump across the shock front. This variation in pressure and density is not linear and the pressure and density fields vary along the curved expansion front. This "misalignment" in the density and pressure fields gives rise to baroclinic torque and, thus, produces the vortices. Note that this mechanism is not dependent upon viscosity.
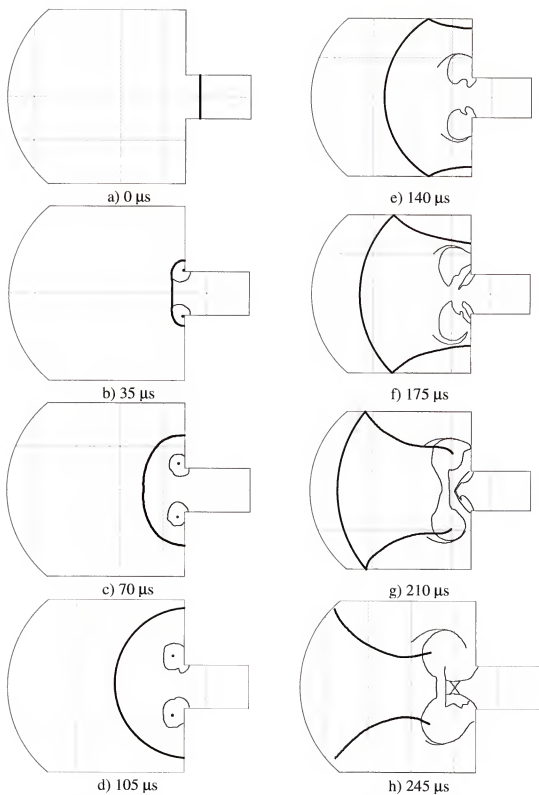
Figure 5.1 Schematic of flowfield evolution for Case 1, Mach 1.413 in air

a) 0 μs

e) 120 μs

b) 30 μs

f) 150 μs

c) 60 μs

g) 180 μs

d) 90 μs

h) frame e, Trial 13
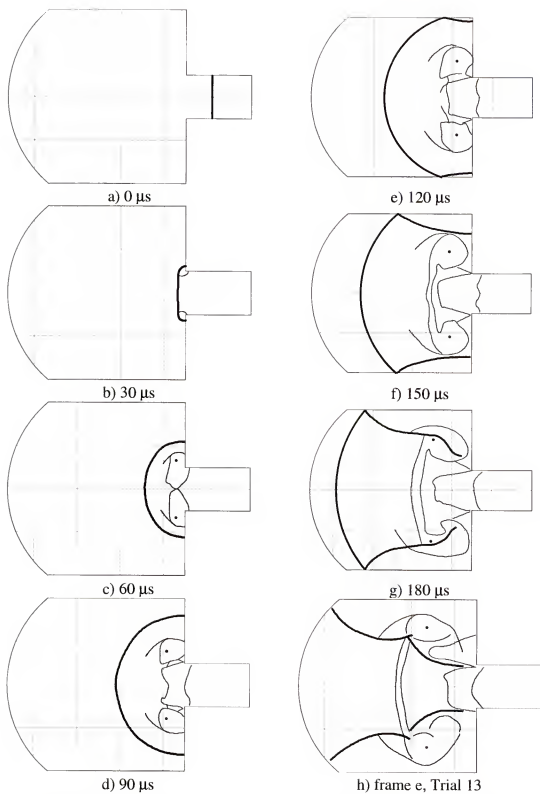
Figure 5.2 Schematic of flowfield evolution of Case 2 (Trial 12, frames a-g and Trial 13, frame h), Mach 1.908 in air

5.1.2 Shock Location

Table 5.1 presents the measured location of the shock wave for both Case 1 and Case 2. The axial location of the shock is the position of the shock along the centerline of the expansion chamber. The lateral location of the shock is measured from the centerline of the chamber to the position of the expanding shock from in the vertical direction. The measurements were made using a computer aided drafting (CAD) software package. The images were imported into the CAD program where it was easy to select the desired points from the image for measurement. The fiducial grid in the images allowed for precise measurements, as their location is exactly known. For all of the presented measurements, the origin (i.e., 0,0) is along the chamber centerline at the exit plane.

In Table 5.1 D non-dimensionalizes the shock locations, where $D=25$ mm, T non-dimensionalizes the time, where $T=D/2c$ ($c=$ *speed of sound in the test gas in the chamber, 345 m/s*), and $(t/T)'$ adjusts the location of the shock to the chamber entrance at $t=0$. The shock strength is defined as the pressure ratio across the shock (p_2/p_1) and is referred to as z'. The nominal value of z is that z of the initial shock wave. Finally, the x/D_{ave} is the 'average' location of the shock front between the experimental images. The shock parameters are computed via direct differencing of the measured data so that these computed values are at the "average" location.

Table 5.1 Axial and lateral shock locations for Case 1 and Case 2

Axial shock locations

	Frame	x (mm)	x/D	t (s)	T (s)	t/T	(t/T)'	W (m/s)	Mach #	z' (p2/p1)	x/D ave	z'/z
Case 1	a	-9.075	-0.3573	0.000E+00	3.681E-05	0.0000	-0.5059	487.343	1.413	2.1613	-0.0215	0.9994
	b	7.982	0.3143	3.500E-05	3.681E-05	0.9508	0.4449	486.229	1.409	2.1507	0.6493	0.9945
	c	25.000	0.9843	7.000E-05	3.681E-05	1.9016	1.3957	470.286	1.363	2.0012	1.3083	0.9253
	d	41.460	1.6323	1.050E-04	3.681E-05	2.8524	2.3465	433.886	1.258	1.6786	1.9312	0.7762
	e	56.646	2.2302	1.400E-04	3.681E-05	3.8031	3.2973	424.400	1.230	1.5988	2.5226	0.7393
	f	71.500	2.8150	1.750E-04	3.681E-05	4.7539	4.2481	416.143	1.206	1.5308	3.1017	0.7078
	g	86.065	3.3884	2.100E-04	3.681E-05	5.7047	5.1989					
Case 2	b	-15.181	-0.5977	0.000E-05	3.681E-05	0.0000	-0.6327	651.817	1.889	3.9978	-0.2127	0.9796
	c	4.374	0.1722	3.00E-05	3.681E-05	0.8150	0.1823	653.083	1.893	4.0140	0.5579	0.9836
	d	23.966	0.9435	6.00E-05	3.681E-05	1.6299	0.9972	554.784	1.608	2.8502	1.2712	0.6984
	e	40.610	1.5988	9.00E-05	3.681E-05	2.4449	1.8122	534.416	1.549	2.6327	1.9144	0.6451
	f	56.642	2.2300	1.200E-04	3.681E-05	3.2598	2.6272	516.467	1.497	2.4479	2.5350	0.5998
	g	72.136	2.8400	1.500E-04	3.681E-05	4.0748	3.4421	504.021	1.461	2.3234	3.1377	0.5693
	h	87.257	3.4353	1.800E-04	3.681E-05	4.8898	4.2571					

Lateral shock locations

	Frame	y (mm)	y/D	t (sec)	T (s)	t/T	W (m/s)	Mach #
Case 1	b	19.130	0.7531	3.500E-05	3.681E-05	0.9508		
	c	31.940	1.2575	7.000E-05	3.681E-05	1.9016	366.000	1.061
	d	46.170	1.8177	1.050E-04	3.681E-05	2.8524	406.571	1.178
Case 2	c	15.644	0.6159	3.000E-05	3.681E-05	0.8150		
	d	27.648	1.0885	6.000E-05	3.681E-05	1.6299	400.135	1.160
	e	40.805	1.6065	9.000E-05	3.681E-05	2.4449	438.573	1.271

5.1.3 Vortex Location

The vortex locations were measured in a similar fashion to the shock locations. The time-resolved images were imported into a CAD program at the center of the vortex was measured from the entrance. In the images where a distinct vortex core was not visible, a circular region was drawn around the region assumed to be the vortex. The geometric center of this circular region is then used as the vortex center. This may not be the actual center of the vortex but is the closest approximation to the center given the image data.

Table 5.2 presents the measured vortex locations for Case 1 and Case 2. Also calculated in this table are the vortex velocity (q). Figure 5.3 depicts the vortex path in relation to the expansion chamber geometry. Note the "hook" in the vortex trajectory of Case 1, which is caused by the interaction of the reflected expansion shock pushing the vortex towards the chamber axis.

Table 5.2 Vortex locations for Case 1 and Case 2

	Frame	x (mm)	x/D	y (mm)	y/D	t (s)	T (s)	t/T	(t/T)'	q (m/s)
Case 1	c	3.503	0.1379	15.308	0.6027	7.00E-05	3.6812E-05	1.9016	1.3957	
	d	7.196	0.2833	17.444	0.6868	1.05E-04	3.6812E-05	2.8524	2.3465	121.90
	e	8.613	0.3391	19.012	0.7485	1.40E-04	3.6812E-05	3.8031	3.2973	60.39
	f	11.648	0.4586	20.544	0.8088	1.75E-04	3.6812E-05	4.7539	4.2481	97.14
	g	15.809	0.6224	22.883	0.9009	2.10E-04	3.6812E-05	5.7047	5.1989	136.36
	h	18.164	0.7151	21.127	0.8318	2.45E-04	3.6812E-05	6.6555	6.1497	83.91
Case 2	d	5.7129	0.2249	16.653	0.6556	6.00E-05	3.6812E-05	1.6299	1.0126	
	e	7.830	0.3083	20.174	0.7943	9.00E-05	3.6812E-05	2.4449	1.8276	136.94
	f	11.944	0.4703	23.921	0.9418	1.20E-04	3.6812E-05	3.2598	2.6426	185.52
	g	15.661	0.6166	27.292	1.0745	1.50E-04	3.6812E-05	4.0748	3.4576	167.26
	h	26.380	1.0386	32.979	1.2984	1.80E-04	3.6812E-05	4.8898	4.2726	404.46
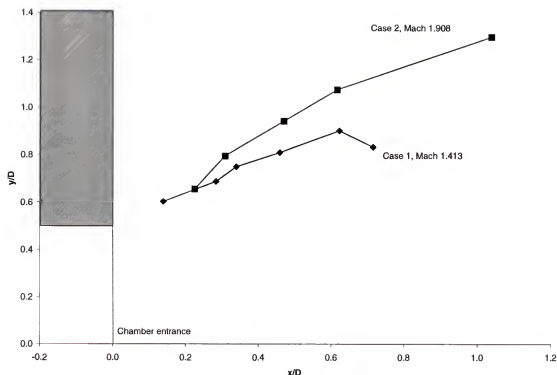
Figure 5.3 Schematic of vortex trajectories for Case 1 (Mach 1.413) and Case 2 (Mach 1.908) in air

If it were assumed that the vortex follows a particle path, then this would suggest a curved trajectory for the vortex as proposed by Whitham (1956). It is been established, however, that the particles comprising the slipstream move along a nearly straight path (Skews, 1967b). As the vortex moves along just below the slipstream it is therefore expected to follow a straight path as well. The current data supports this position. The vortex trajectories sketched in Figure 5.3 very nearly follow straight paths. The difficulty in measuring the exact vortex core location accounts for the data not falling on a perfectly straight line.

5.1.4 Wall Shock Mach Number

The wall shock is defined as the shock that undergoes diffraction at the sharp corner and expands axially along the wall. This is depicted in Figure 5.4. Previous work by Skews (1967a) present experimental data for expanding shock flows of Mach numbers from 1.5 to 4.0 about corners of various angles ranging from 15° through 165°. In this data, an initial shock of Mach 1.5 is shown to have a wall shock Mach number of 1.15 and, similarly, an initial shock of Mach 2.0 has a wall shock Mach number of 1.3 while expanding around a 90° corner.

The wall shock Mach number for the current data can be determined from the time-accurate imagery. For Case 1, frames b, c, and d of Figure 5.1 are used to measure the wall shock velocity and Mach number. For Case 2, frames b, c, and d are used as well.
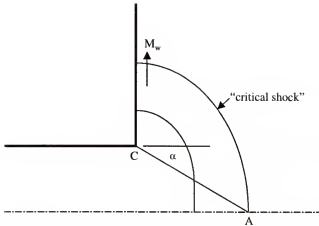
Figure 5.4 Schematic of shock wave expanding at sharp corner

Table 5.1 shows the measured data and the corresponding wall shock Mach numbers for Case 1 and 2. Here it is seen that for both cases, the initial expansion wall shock Mach number is lower than expected but the wall shock Mach number between frames c and d in both cases is very close to the data of Skews (1967a).

<u>5.1.5 Critical Shock</u>

The expansion of a shock within an area change occurs in two phases. The axial shock strength remains roughly constant before decreasing rapidly (Sloan and Nettleton, 1975). This is due to the fact that the shock remains planar until the "critical shock" is reached. The critical shock is that shock wave that first becomes non-planar. This is seen in Figure 5.4 where as the shock undergoes its expansion, the region of the shock wave that is planar steadily decreases along the line *C-A*. According to Sloan and Nettleton (1975), when a shock wave passes a convex corner an expansion wave is propagated radially through the flow behind the shock. This wave travels at the local velocity of sound relative to the gas. By considering the relative velocities of the expansion wave and the incident shock wave, Skews (1967a) showed that the trajectory of the point of contact between the shock and the expansion wave was linear and inclined at an angle α to the original direction of the flow, where

$$\tan^2 \alpha = \frac{(\gamma - 1)(M^2 - 1)\left[M^2 + \frac{2}{(\gamma - 1)}\right]}{(\gamma + 1)M^4}. \tag{5.1}$$

In two dimensions, the shock wave is diffracted at each edge of the area change. Considering both diffractions together leads to an exact description of the expansion of the shock up to the instant that the shock and the expansion waves from the opposite corners interact.

If the shock is free to expand in three dimensions, it diffracts around the rim of the entrance of the area change. Equation 5.1 was developed by Skews (1967a) for a two dimensional diffraction. The shape and strength of the diffracting wave is different in

three dimensions, but the angle of the propagation α of the intersection of the shock and expansion wave remains unchanged.

For the present data, the angle of propagation α is measured directly from the imagery. Figure 5.5 shows the measurement of the propagation angle for Case 1 and Case 2. For accuracy, the schematic images were imported into a computer aided drafting (CAD) software package for measurement.

The measured angles shown in Figure 5.5 are compared with the equation of Skews (1967a) in Figure 5.6. Here it is seen that excellent agreement in the propagation angle with Mach number for the present data and that of Skews (1967a).

a) Case 1, Mach 1.413   b) Case 2, Mach 1.908

Figure 5.5 Measurement of propagation angle for experimental data of Case 1 and Case 2

5.1.6 Supersonic vs. Subsonic Expansion

A good qualitative comparison of the present data is to compare the expanding flowfields of Case 1 and Case 2. For Case 1 the measured shock speed entering the chamber is 1.413. This corresponds to a pressure increase (p_2/p_1) of 2.163 via equation 1.2. The induced velocity of the gas behind the shock is given via equation 1.5 to be 219.97 m/s. The speed of sound behind the shock is given by $a^2 = \gamma RT$. The temperature increase across the shock is given via equation 1.3 to be 373.88 K. This corresponds to a subsonic Mach number behind the shock of 0.565.
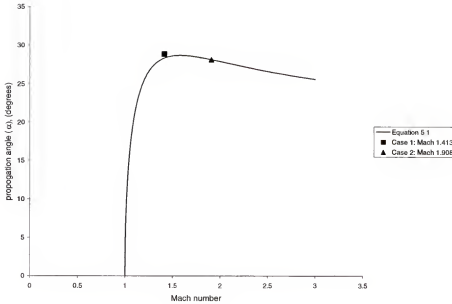
Figure 5.6 Propagation angle vs. Mach number for current data and theory of Skews (1967a)

Case 2 on the other hand has a measured shock Mach number of 1.908 entering the chamber. Through a similar analysis to Case 1, the induced velocity in the flow behind the shock is 414.3 m/s that corresponds to a Mach number of 0.946. Figure 5.7 depicts direct comparisons of the Case 1 expansion to Case 2. These are the schematic images presented in Figures 5.1 and 5.2 earlier in this chapter. The images shown in Figure 5.7 have the shock fronts at very nearly the same location, which is purely coincidence. The images shown in Figure 5.7 can not be compared directly at a given time. That is because the time accuracy of the data is only valid frame to frame for any trial. The timing of the camera from trial to trial is based upon a predetermined time delay from the arrival of the shock wave at the number two pressure transducer within the shock tube. Since the shock waves varied in strength from shot to shot, the initial image of the shock wave was at random locations within the tube.
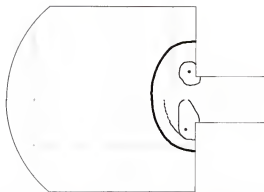
a) top: Case 1, frame *c*, bottom: Case 2, frame *c*
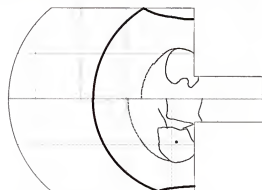
b) top: Case 1, frame *e*, bottom: Case 2, frame *e*
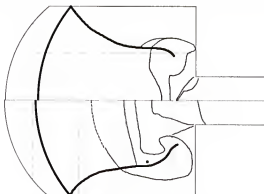
c) top: Case 1, frame *g*, bottom: Case 2, frame *g*

Figure 5.7 Comparison of flowfield structure for Case 1 versus Case 2

However, qualitative comparisons of the images in Figure 5.7 can be made. It is seen from Figure 5.7 *a* that for a similar shock location, the vortex for the Case 2 expansion has propagated further into the flowfield and that the region of vorticity is

larger. These statements are also valid for Figure 5.7 *b* and *c* as well. Naturally, the stronger expansion gives rise to increased convection of the vortices and increased strength. Recall that the difference in wall Mach number for Case 1 and 2 was 13% (1.15 vs. 1.3 respectively). The difference in axial Mach number is, at least initially, 33% (Mach 1.5 vs. Mach 2). Therefore, along the shock front there is a greater variation in Mach number for Case 2 than for Case 1 which leads to increases in the baroclinic torque and, hence, vorticity. Note also that in figure 5.7 *b* that for a similar shock axial position, the Mach 2 shock has greater curvature. Again, this is related to the relatively small variation in wall Mach number vs. axial Mach number. Also it is noticed that the vortex produced in Case 2 is stronger as it has severely diffracted the shock as opposed to Case 1. This again is related to the fact that the wall Mach numbers vary only slightly while the vorticity produced is greater for Case 2 vice Case 1.

5.1.7 Two-dimensional vs. Three-dimensional Sudden Shock Expansions

Sloan and Nettleton (1975) point out that the axial shock does not decay until it becomes the critical shock as discussed in section 5.1.5. After this, the shock will continue to expand eventually acquiring symmetry; cylindrical symmetry for 2-D and spherical symmetry for 3-D. Chisnell (1957) developed a first order relationship to determine the shock strength in channels with varying geometry. Sloan and Nettleton (1975) conclude from their work that the analysis of Chisnell can be extended to include abrupt area changes provided that the initial shock area is defined in terms of the surface area of the axial segment of the critical shock.

According to Chisnell (1957), a shock strength/area relation can be formulated such that

$$A * f(z) = \text{constant} \tag{5.2}$$

where z is defined as the shock pressure ratio (i.e., $z = p_2/p_1$) and A is defined as the surface area of the shock wave. The Chisnell function $f(z)$ is given as

$$f(z) = z^{1/\gamma}(z-1)\left(z+\frac{\gamma-1}{\gamma+1}\right)^{-1/2}\left[\frac{1+\left(z+\frac{\gamma-1}{(\gamma+1)z}\right)^{-1/2}}{1-\left(z+\frac{\gamma-1}{(\gamma+1)z}\right)^{-1/2}}\right]^{\sqrt{\frac{\gamma}{2(\gamma-1)}}} *$$

$$\left[\frac{1+\left(z+\frac{\gamma-1}{(\gamma+1)z}\right)^{-1/2}-\left(\frac{\gamma-1}{2\gamma}\right)^{1/2}}{1+\left(z+\frac{\gamma-1}{(\gamma+1)z}\right)^{-1/2}+\left(\frac{\gamma-1}{2\gamma}\right)^{1/2}}\right]e^{\left[\left(\frac{2}{\gamma-1}\right)^{1/2}\tan^{-1}\left(\frac{2}{\gamma-1}\left(\frac{yz}{z+\frac{\gamma+1}{\gamma-1}}\right)^{1/2}\right)\right]} \tag{5.3}$$

Applying the theory of Chisnell to understand the differences between a spherically and cylindrically expanding shock yields the following. According to Sloan and Nettleton (1975) the onset of decay occurs at

$$X_c = \frac{w}{2}\cot\alpha \tag{5.4}$$

for a cylindrical shock emanating from an opening of width w and at

$$X_s = \frac{d}{2}\cot\alpha \tag{5.5}$$

for a spherical shock emanating from a opening of diameter d. Again, according to Sloan and Nettleton (1975) $X_c = X_s$. The surface area for the cylindrical shock undergoing a sudden expansion about a 90° corner at the onset of decay is given as

$$A_c = \pi X_c h \tag{5.6}$$

and the surface area of a spherical shock undergoing a sudden expansion about a 90° opening at the onset of decay is given as

$$A_s = 2\pi X_s^2. \tag{5.7}$$

The Chisnell relationship given in equation 5.2 can then be used to study the evolution of a 2-D or 3-D shock expansion. For any Mach number and geometry, the shock surface area and pressure ratio can be determined via equations 5.1, 5.4-5.7. Given the shock strength, the shock speed, W, is known. For a small δt, a new position of the shock can be calculated and a new, increased, shock area is found via equation 5.6 or 5.7. The Chisnell relation (equation 5.2) gives a new $f(z)$ and a new pressure ratio, z, can be found. The Mach number of this expanded shock wave can be found via equation 1.2 and a new shock speed, W, is calculated. This process is repeated over and over to determine the variation in shock strength for the expanding shock.

The above process was carried out for cylindrical shocks with Mach numbers 1.413 (Case 1), 1.5, 1.908 (Case 2) and 2.0 emanating from an opening that is 25mm x 25mm square which is allowed to expand in one direction only and also for a spherical shock of Mach numbers 1.5 and 2.0 emanating from a circular opening that is 25mm in diameter which is allowed to expand in all directions. Figure 5.8 shows the decay in shock strength (z'/z) for these cases. As expected, the drop off in strength for the spherical shock is more severe than for the cylindrical shock. Also shown in Figure 5.8 are the calculated pressure ratios for Case 1 and Case 2 as calculated in Table 5.1. These ratios were found by noting the difference in shock location between successive
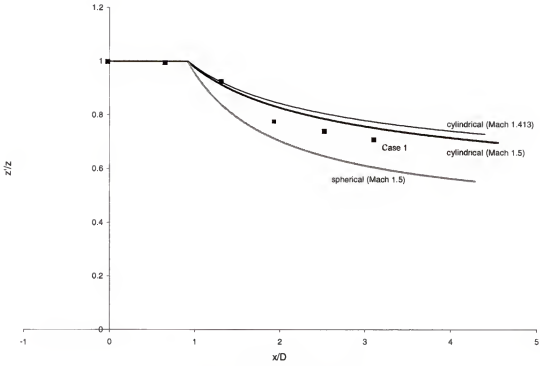
a) Case 1 (Mach 1.5 and 1.413)
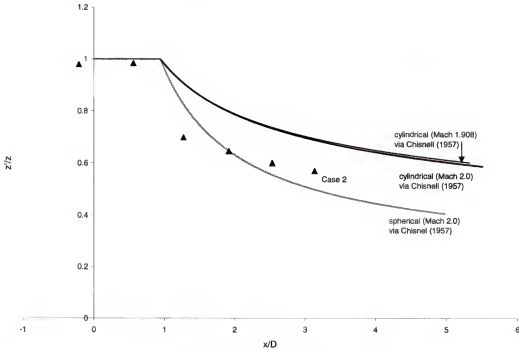
b) Case 2 (Mach 2.0 and 1.908)

Figure 5.8 Shock strength decay vs. location for a cylindrical and spherical shocks according to the theory of Chisnell and current data

frames of the experimental data. The agreement of the current data with the theory of Chisnell is poor which indicates that the assumptions for this theory are no longer valid in the current geometry. However, Sloan and Nettleton (1975) have validated this theory for a shock undergoing sudden expansion in a vessel with an expansion ratio of 15:1. The current data has an expansion ratio of 4:1. For the current geometry, the expanding shocks experience the confinement when the shocks are only 1.5D into the chamber.

It should be recalled that the measured and predicted wall shock Mach numbers were quite small in comparison the shock front Mach number (1.15 vs. 1.5 in Case 1 and 1.3 vs. 2.0 for Case 2). This fact alone implies that the shock will not expand uniformly in all directions which accounts for the mismatch in shock location in Figure 5.8. Due to the increased expansion ratio (15:1) of the work of Sloan and Nettleton (1975) the shock front may reach uniform expansion during that process but in the early stages of the event, the shock front does not follow cylindrical or spherical expansion.

The plot of the non-dimensional axial shock position (x/D) vs. the non-dimensional time (t/T, where $T=D/2a$) is given in Figure 5.9 for the same Mach numbers of Figure 5.8. While it is seen that the spherical shock wave expands slower than the cylindrical shock wave, the difference in location, at least up to 2D, is quite small. This is especially true for the current data (Mach 1.413 and Mach 1.908) compared with the spherical shock waves of Mach 1.5 and 2.0 respectively. This point will be important in the comparison of the present data to three-dimensional numerical data to be discussed in a following section.
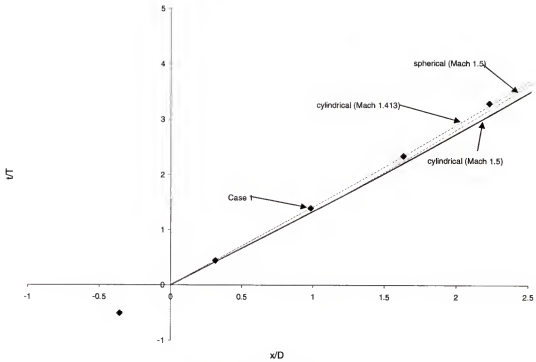
a) Case 1 (Mach 1.5 and 1.413)
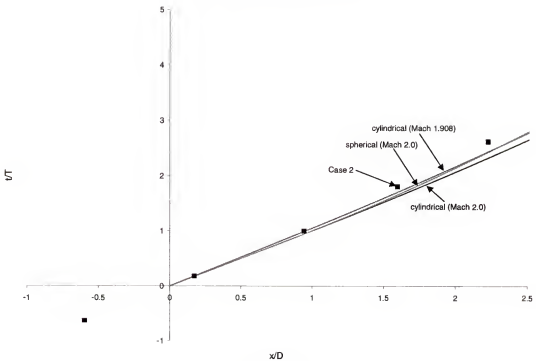
b) Case 2 (Mach 2.0 and 1.908)

Figure 5.9 Axial shock location for a cylindrical and spherical shocks according to the theory of Chisnell

5.2 Comparison with Numerical Data

Now that the experimental data has been thoroughly presented, detailed comparison to numerical data will be done to gain further insight into the fluid dynamic physics. Numerical data or experimental data on its own cannot give the insight into the fluid dynamic mechanisms of interest such as compressibility, turbulence, shock/vortex interaction, and mixing. It is only through this process that new information can be learned.

The first part of this section will be a comparison of the present data to that of existing two-dimensional axisymmetric and three-dimensional numerical data. The next part will compare the current data with new, unpublished two-dimensional data specific to the current geometry. These comparisons will allow for the assessment of the ability of the codes to match the experimental data as well as assessing the two-dimensional vs. two-dimensional axisymmetric and three-dimensional flow structure.

5.2.1 Two-dimensional Axisymmetric and Three-dimensional Numerical Data

Table 1.2 detailed the limited data available for the sudden expansion of a shock wave. The works of Abe and Takayama (1990), Yu and Grönig (1996), and Jiang et al. (1999) present data for an unconfined expansion of a shock wave. This data may be used for comparison with the current work during the initial expansion (i.e., before the expanding shock wave encounters the confining chamber). Of the other works presented in Table 2.1, Chang and Kim (1995) and Jiang et al. (1997), may be directly compared with the current data noting that the geometric expansion and confining chamber are circular while the current work is square. The work of Pantow et al. (1996) details the

expansion of a detonation wave from a rectangular section. Because of the distinct differences between shock waves and detonation waves these data will not be compared with the current work.

A major difference to keep in mind during the ensuing comparisons between the current results and the work of Chang and Kim (1995) and Jiang et al. (1997) is the shock tube cross sectional shape. The data reported herein has a 25 mm x 25 mm square shock tube that is allowed to expand in one dimension only (refer to Figure 2.8). The data of Chang and Kim (1995) and Jiang et al. (1997) are for circular shock tubes of 25 mm in diameter. Finally, the work of Jiang et al. (1999) present data for an unconfined shock expansion from a square shock tube that is 40 mm x 40 mm..

5.2.1.1 Shock and Vortex Location Comparison

The evolution of the sudden shock expansion within the shock tube expansion device has been quantified in Section 5.1.2. A comparison of axial progression of the shock front for the current data and that of Chang and Kim (1995) and Jiang et al. (1997) are presented in Figures 5.10 and 5.11. An x vs. y plot of the comparison of the vortex core trajectories for the current data and that of Chang and Kim (1995), Jiang et al. (1997), and Jiang et al. (1999) is presented in Figure 5.12.

As can be seen in Figures 5.10 and 5.11, the agreement of the shock wave expansion is very good as compared to Chang and Kim (1995). Chang and Kim (1995) specifically cite the time interval between their presented images. In contrast, Jiang et al. (1997) present similar flowfield data but do not specifically provide the time basis. This explains the mismatch of data presented in Figure 5.10 since it was not explicitly given in the reference and therefore it was assumed that the time sequence between images of

Jiang et al. (1997) is T; just as is the case for Chang and Kim (1995). However, this does not appear to be the case and thus we cannot correlate the present data to the work of Jiang et al. (1997) accurately. The Mach 2.0 data of Jiang et al. (1997) are therefore not presented with the data of Figure 5.11. However, the Jiang et al. (1997) data can be used for the comparison of vortex trajectories in Figure 5.12 since it is time independent.

The good correlation with axial shock progression for the current two-dimensional planar data vs. the two-dimensional axisymmetric data of Chang and Kim (1995) is easily explained from the discussion of section 5.1.7. Here it was shown that early on in the sudden expansion process (i.e., within the first 2-2.5 x/d), a two-dimensional planar at nearly the same rate as that of a two-dimensional axisymmetric shock front.

Figure 5.12 compares the x- vs. y-location of the vortex core for the current data (Cases 1 and 2), the data of Chang and Kim (1995), Jiang et al. (1997), and Jiang et al. (1999). Note here that the vortex trajectories determined by Jiang et al. (1999) are for the mid-wall and diagonal axis of the square tube. It is noticed that for all the data the vortex trajectories emanate in nearly straight lines from the expansion corner in agreement with Skews (1967b). The curvature of the vortex trajectories for both Chang and Kim (1995) and Jiang et al. (1997) occur due to the small ratio of the expansion chamber (3:1) vice the current data expansion ratio of 4:1.
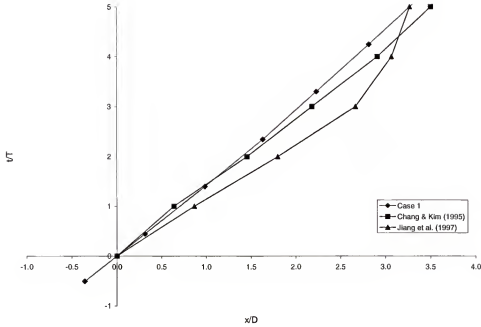
Figure 5.10 Shock front location (x/D) vs. time (t/T) for Case 1 (Mach 1.413), Mach 1.5 data of Chang and Kim (1995), and Mach 1.5 data of Jiang et al. (1997)
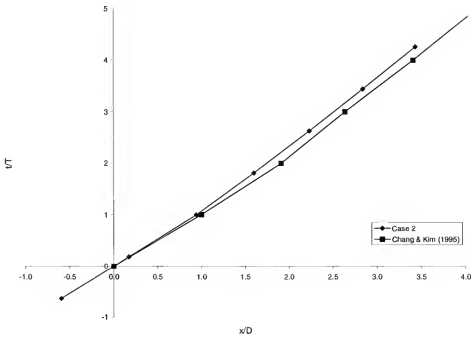
Figure 5.11 Shock front location (x/D) vs. time (t/T) for Case 2 (Mach 1.908) and Mach 2.0 data of Chang and Kim (1995)
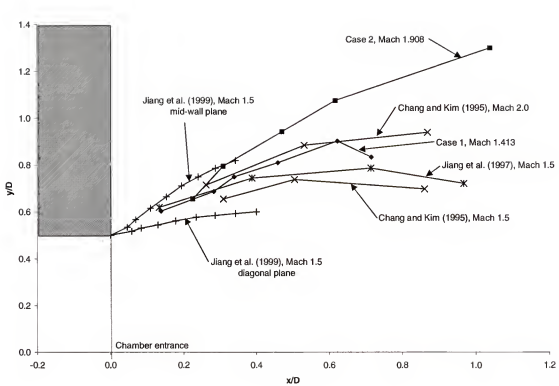
Figure 5.12 Vortex locations (y vs. x) of Cases 1 and 2 and the reference data of Chang and Kim (1995), Jiang et al. (1997), and Jiang et al. (1999)

5.2.1.2 Flow Structure Comparison

Direct comparison of the current experimental data with the numerical image data of Chang and Kim (1995) and Jiang et al. (1997) are presented in Figures 5.13 and 5.14. In Figure 5.13 we have near alignment of the shock fronts for the current data of Case 1 (frame c, $t/T = 1.396$) with that of Jiang et al. (1997) at an unknown time and also for the current data of Case 1 (frame d, $t/T = 2.347$) with that of Chang and Kim (1995) at $t/T = 2$. Note that the agreement in shock fronts is expected from the prior analysis of section 5.1.7. Also note that the initial vortex core formations are of similar size but that the vortex location of Chang and Kim (1995) is slightly ahead of that of the current data.
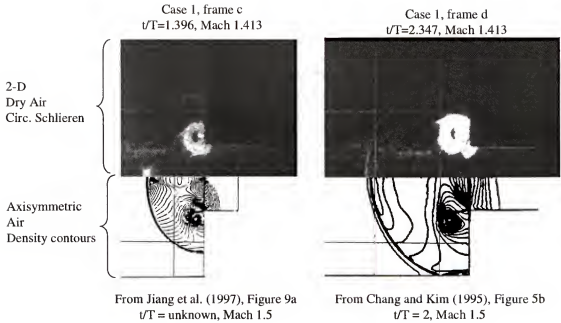
Figure 5.13 Direct comparison between current experimental data (Case 1, Mach 1.413) and numerical data of Jiang et al. (1997) and Chang and Kim (1995)
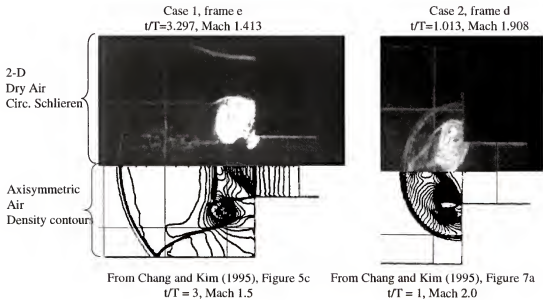
Figure 5.14 Direct comparison between current experimental data (Case 1, Mach 1.413, and Case 2, Mach 1.908) and numerical data of Chang and Kim (1995)

Figure 5.14 compares the data of Case 1 (frame e, $t/T = 3.297$) with that of Chang and Kim at $t/T = 3$ and also of the current data of Case 2 (frame d, $t/T = 1.013$) with that of Chang and Kim (1995) at $t/T = 1$. Here, the former image clearly shows the advanced progression of the vortex core for the Chang and Kim (1995) data vs. the current work. The latter image shows almost a direct comparison of the two data again confirming that early on in a sudden shock expansion, two-dimensional planar and two-dimensional axisymmetric progression is very similar. This image comparison also shows very similar structure in the core flowfield as well.

Based upon this data, we are seeing good agreement of flow structure upon immediate exit of the shock from the tube. But as the shock continues to move away from the tube exit, the correlation shock front and vortex location between the current data and the data of Chang and Kim (1995) and Jiang et al. (1997) becomes worse. This may be attributed to the cylindrical vs. spherical shock tube exit for the two data sets. More specifically, the geometric difference results in different pressure and density distributions which, in the form of the baroclinic term, causes different vorticity generation in time and space. While the shock speed and location depend on the flow configuration, in the present case, the shock development seems to be dictated less by the geometric details and more by the basic parameters such as Mach number and the fact that there is a sudden expansion.

5.2.2 Two-dimensional Planar Numerical Data

New numerical data specific to the geometry of the shock tube expansion device has been computed by Edwards (1999) of the United Kingdom's Defense Evaluation Research Agency (DERA). This data is an attempt to benchmark the DERA numerical

code called DRAMR as well as provide data specific to the shock tube expansion device geometry. The DRAMR (Defense Research Agency Mesh Refinement) is a coding environment that was conceived with three primary objectives:

- The code should be conveniently and directly applicable to a wide range of problems.
- The code should facilitate rapid, convenient incorporation of numerical solvers for evaluation, testing, and development.
- The code should allow unimpeded development of high resolution numerical schemes suitable for use in hypersonic aerodynamics at relatively low cost in both manpower and computer effort.

Currently DRAMR solves for perfect gas flows described by either the Euler equations or the Navier-Stokes equations using time marching, explicit, cell centered characteristics based schemes. To maintain generality, the code has been developed with real and reacting gases in mind and contains suitable 'hooks' to enable the incorporation of such gas dynamic terms. The only limitation inherent in DRAMR is that all numerical schemes must be cell-centered. A more complete description of DRAMR, the geometry of the computational mesh, and an example of the adaptive grid used in the following simulations are presented in Appendix A.

Edwards (1999) computed Case 1 (Mach 1.413) and Case 2 (Mach 1.908) in the DRAMR environment for this research. The initial data computed for this effort used a 1 mm x 1 mm grid resolution with adaptation of the grid based upon $\nabla \rho$. The adaptation is 4:1 when density gradients are is excess of 20% of the global maximum. With this computational scheme, shock waves occur over three cells.

The results for Case 1 are given in Figures 5.15 and 5.16 and the results for Case 2 are given in Figures 5.17 and 5.18. In Figures 5.15 and 5.17, the time accurate data is

presented depicting density gradient at the same time as the experimental data of Cases 1 and 2 respectively. Figures 5.16 and 5.18 present schematics of the flowfield evolution similar to the experimental data presented in Figure 5.1.

a) 0.0 μsec

b) 35.0 μsec

c) 70.0 μsec

d) 105.0 μsec

e) 140.0 μsec
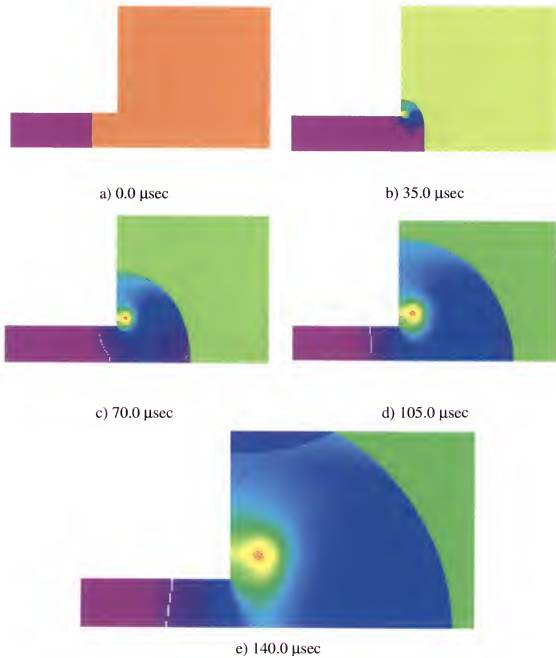
Figure 5.15 Density gradient images from DRAMR computational results for Case 1 (Mach 1.413)

a) 0.0 μsec

b) 35.0 μsec

c) 70.0 μsec

d) 105.0 μsec

e) 140.0 μsec
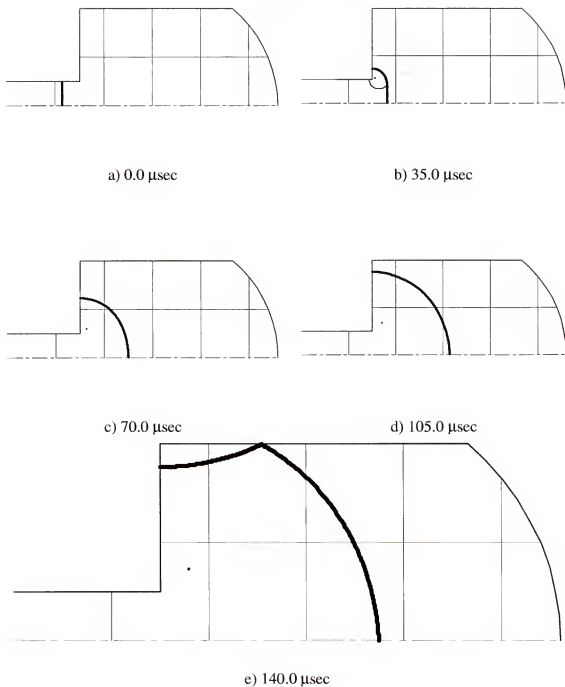
Figure 5.16 Schematics of flowfield structure from DRAMR computational results for Case 1 (Mach 1.413)

a) 30.0 μsec

b) 60.0 μsec

c) 90.0 μsec

d) 120.0 μsec

e) 150.0 μsec

f) 180.0 μsec
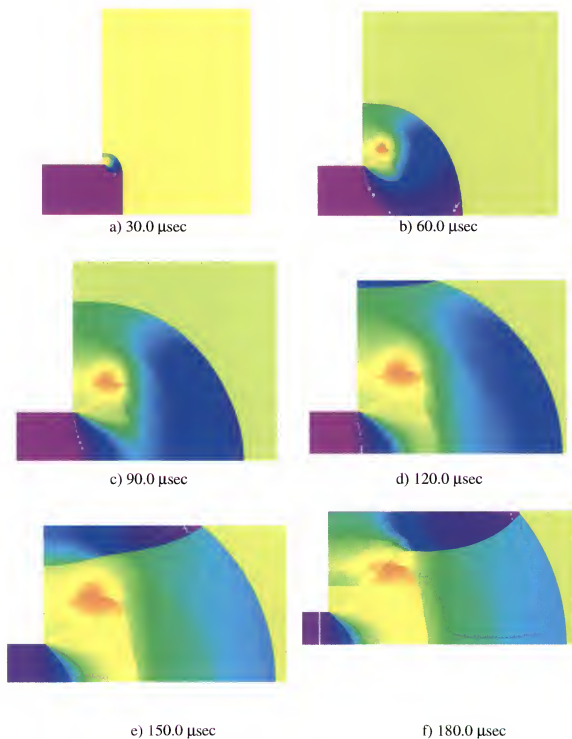
Figure 5.17 Density gradient images from DRAMR computational results for Case 2 (Mach 1.908)

a) 30.0 μsec

b) 60.0 μsec

c) 90.0 μsec

d) 120 μsec

e) 150.0 μsec

e) 180.0 μsec
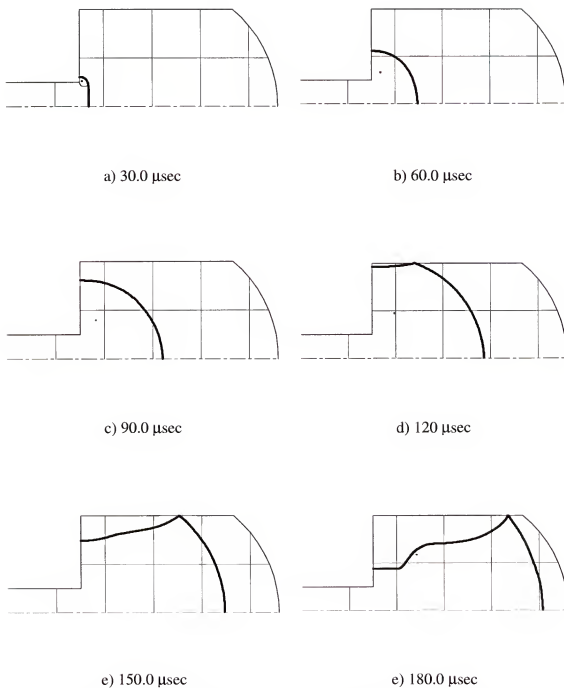
Figure 5.18 Schematics of flowfield structure from DRAMR computational results for Case 2 (Mach 1.908)

5.2.2.1 Grid Refinement Study

A grid refinement study was performed to insure that the spatial resolution of the DRAMR data was adequate. As previously noted, the initial results were computed on a base grid that was 1 mm x 1 mm for the full size geometry (see Figure A.1). This grid is refined at a factor of 4:1 where the local density gradient exceeds 20% of the global maximum. This results in refined, overset meshes that are .25 mm x .25 mm where required by the DRAMR algorithm.

A second study was performed where the base grid was halved to .5 mm x .5 mm. The same mesh refinement criterion was applied such that the overset refined meshes are .125 mm x .125 mm where required. Comparing the results of the second study to that of the first showed little noticeable change in the data. The comparison of shock location and flow structure, in general, was quite good. It would appear that the grid resolution of 1 mm x 1 mm is adequate for this geometry. However since the second data set were available, it used in this work. Therefore, all the DRAMR data presented in the following sections are from computations on the finer (.5 mm x .5 mm) grid.

5.2.2.2 Flow Structure Comparison

Figures 5.19 through 5.24 present the direct flowfield comparisons for the DRAMR data and the current experimental data. For Figures 5.19 through 5.23 the DRAMR data shows density gradient for a grid that is .5 mm x .5 mm in all cases. The DRAMR data for Figure 5.24 shows density contours. The experimental data are all circular cut-off Schlieren images of the evolving flowfield. Note that for all the DRAMR data of Figures 5.19 through 5.24 the computations were inviscid

Case 1, Mach 1.413
Time = .000070 sec
.5 mm x .5 mm grid with refinement
Refinement: 4:1 at ∇ρ > 20% global max gradient
Inviscid flow throughout

∇ρ

Figure 5.19 Direct comparison of current circular cut-off Schlieren data (Case 1, frame c) and numerical density gradient data from DRAMR (Case 1, t=70 μS, Mach 1.413)

Case 1, Mach 1.413
Time = .000140 sec
.5 mm x .5 mm grid with refinement
Refinement: 4:1 at ∇ρ > 20% global max gradient
Inviscid flow throughout

∇ρ
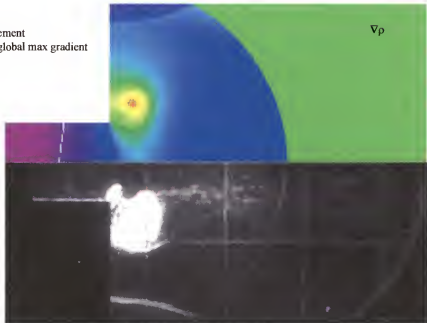
Figure 5.20 Direct comparison of current circular cut-off Schlieren data (Case 1, frame e) and numerical density gradient data from DRAMR (Case 1, t=140 μS, Mach 1.413)

Case 2, Mach 1.908
Time = .000060 sec
.5 mm x .5 mm grid with refinement
Refinement: 4:1 at $\nabla\rho$ > 20% global max gradient
Inviscid flow throughout

$\nabla\rho$
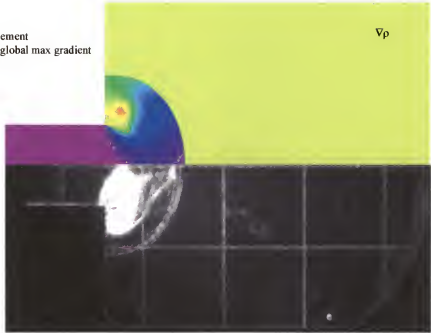
Figure 5.21 Direct comparison of current circular cut-off Schlieren data (Case 2, frame d) and numerical density gradient data from DRAMR (Case 2, t=60 µS, Mach 1.908)

Case 2, Mach 1.908
Time = .000120 sec
.5 mm x .5 mm grid with refinement
Refinement: 4:1 at $\nabla\rho$ > 20% global max gradient
Inviscid flow throughout

$\nabla\rho$
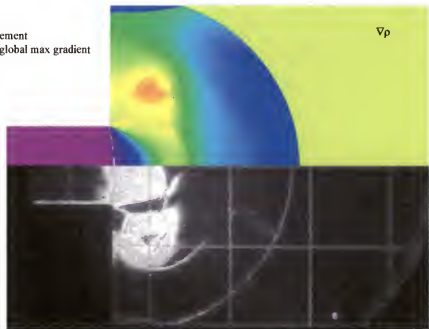
Figure 5.22 Direct comparison of current circular cut-off Schlieren data (Case 2, frame f) and numerical density gradient data from DRAMR (Case 2, t=120 µS, Mach 1.908)

Case 2, Mach 1.908
Time = .000180 sec
.5 mm x .5 mm grid with refinement
Refinement: 4:1 at $\nabla\rho$ > 20% global max gradient
Inviscid flow throughout

$\nabla\rho$
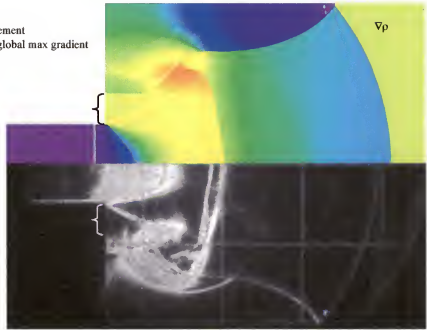
Figure 5.23 Direct comparison of current circular cut-off Schlieren data (Case 2, frame h) and numerical density gradient data from DRAMR (Case 2, t=180 μS, Mach 1.908)

Case 2, Mach 1.908
Time = .000180 sec
.5 mm x .5 mm grid with refinement
Refinement: 4:1 at $\nabla\rho$ > 20% global max gradient
Inviscid flow throughout

$\nabla\rho$
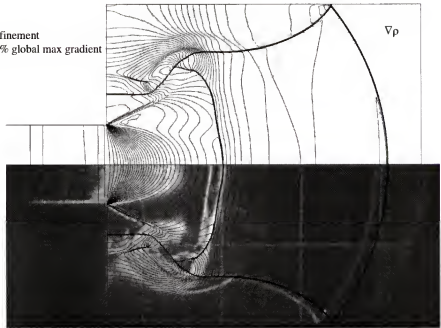
Figure 5.24 Direct comparison of current circular cut-off Schlieren data (Case 2, frame h) and numerical density contour data from DRAMR (Case 2, t=180 μS, Mach 1.908)

5.2.2.3 Shock and Vortex Location Comparison

Although the DRAMR data and the current data are depicted at exactly the same times, plotting of the shock and vortex locations for these data as well as for the two-dimensional axisymmetric data is useful. Figure 5.25 depicts the shock front location for the current data, the DRAMR data, and the data of Chang and Kim (1995) for Case 1 and Case 2. Figure 5.26 plots the vortex trajectories of the current data, that DRAMR data, the data of Chang and Kim (1995), and the data of Jiang et al. (1997). Time-accurate position of the vortices in both the x- and y-directions are plotted as well in Figure 5.27 for the Case 1 data and in Figure 5.28 for the Case 2 data. Note that the data of Jiang et al. (1997) is not included in the latter figures as the temporal resolution of that data is unknown.

As seen in the direct comparison of Figures 5.19 and 5.21 for the Case 1 (Mach 1.413) data and in Figures 5.25a, 5.26a, and 5.27, there is excellent agreement of the shock location and the vortex position. In fact, there is near exact alignment of the shock front for the experimental data and DRAMR data of Case 1. Comparing the vortex trajectory data of Figure 5.27, note that there is near exact agreement of the current data, the DRAMR data, and the Chang and Kim (1995) data in t/T vs. y/D. The agreement in t/T vs. x/D is not as good. This goes back to the earlier argument of the two-dimensional axisymmetric vortex is converted downstream faster that two-dimensional planar but the lateral movement of the vortex in identical.
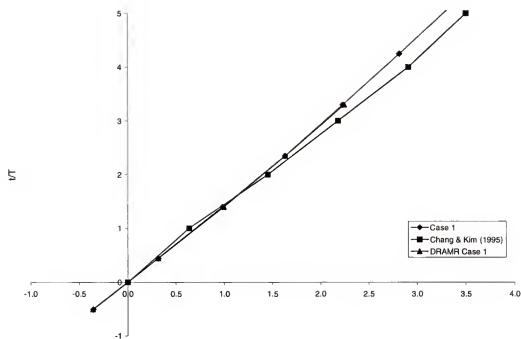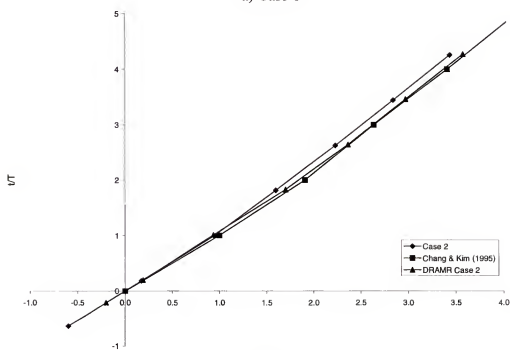
a) Case 1

b) Case 2

Figure 5.25 Shock front location (x/D) vs. time (t/T) for current data, DRAMR data, and data of Chang and Kim (1995)
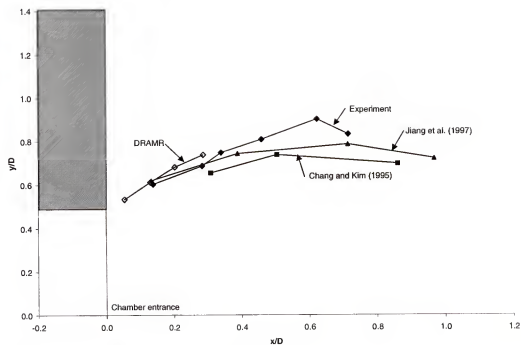
a) Case 1
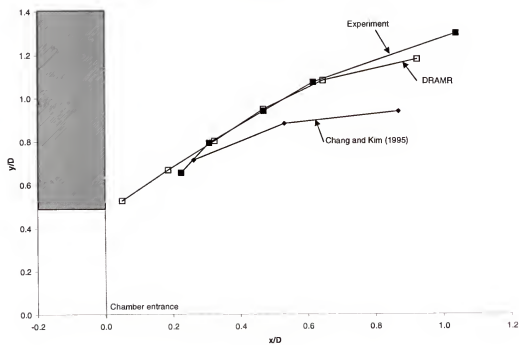
b) Case 2

Figure 5.26 Vortex location (y/D vs. x/D) for current data, DRAMR data, the data of Chang and Kim (1995), and the data of Jiang et al. (1997)
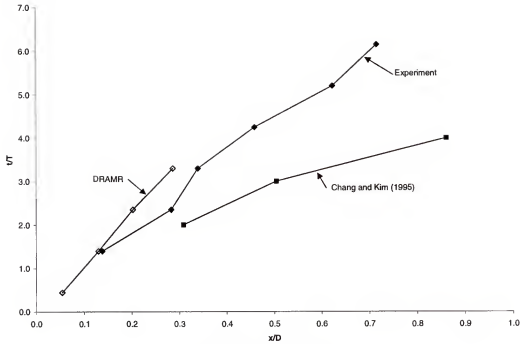
a) time vs. x-location
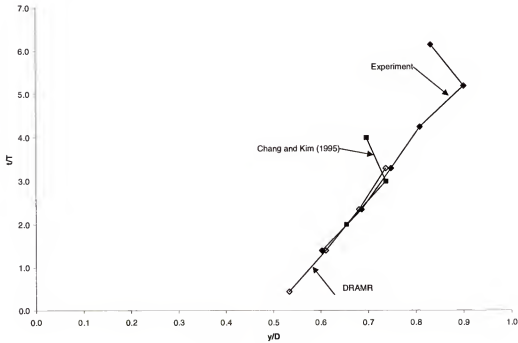
b) time vs. y-location

Figure 5.27 Time-accurate vortex location for current data, DRAMR data, and the data of Chang and Kim (1995) for Case 1
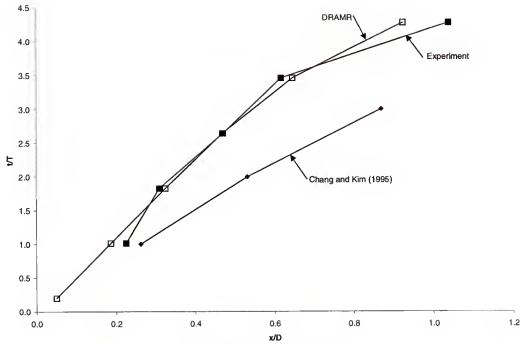
a) time vs. x-location
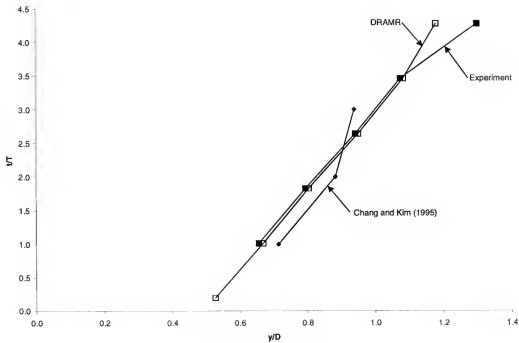
b) time vs. y-location

Figure 5.28 Time-accurate vortex location for current data, DRAMR data, and the data of Chang and Kim (1995) for Case 2

The comparison of the Case 2 (Mach 1.908) data is not as good but it does show an interesting trend. The shock front progression initially matches the experimental data as seen in Figure 5.25b. However, as the shock expands, the front begins to correlate better with the data of Chang and Kim (1995). If we examine the location of the vortices in Figure 5.28, it is seen that there is much better agreement of the DRAMR data to the experimental data. Just as in Case 1, the x-progression of the vortex is off but the lateral progression match well for all three data sets. So there is mismatch in shock front location but agreement in vortex formation for the Case 2 data.

Returning to the shock front location for the current data and the DRAMR data of Case 2, it is seen that there is excellent agreement in the first image comparison (Figure 5.21). The measured location of the starting shock was checked for errors but was found to be accurate. As the flow progresses, there is general agreement in the flow structure. However, as is seen in Figures 5.22 through 5.24, the DRAMR shock is progressing faster in the chamber than the experimental data or, conversely, the experimental data is decaying faster than the DRAMR data. This would indicate, perhaps, an error in the initial conditions.

The initial conditions given to Edwards (1999) for the DRAMR computations consisted of the initial pressure and temperature of the gas within the chamber, the location of the shock in the entrance shock tube, and the Mach number of the incident wave (see Figure A.1). The location of the incident shock has been verified as accurate. Also, based upon successive experimental images, which are accurate in time, the initial speed of the incident shock is known. However, there could be variations in the measured pressure and temperature of the initial gas within the chamber. Variations of

these values could effect the speed of sound. Reasonable variations of these values show that the speed of sound may be anywhere from 340 m/s to 350 m/s (a variation of ± 5 m/s). This results in a Mach number range from 1.88 to 1.94.

To see if initial condition errors were perhaps causing the mismatch in shock front location in Case 2, Edwards (1999) generated another solution for Case 2 where the incident Mach number is 1.88. The comparison of this solution to the Mach 1.908 solution is given in Figure 5.29. Here it is seen that, indeed, the shock front for the lower incident Mach number lags behind the Mach 1.908 shock front. However, the variation in location is much smaller than the difference observed in Figure 5.23. Obviously, there is no significant error in the initial conditions and that this difference must be caused by other reasons.

Case 2, Mach 1.908
Time = .000180000 sec
.5 mm x .5 mm grid with refinement
Refinement: 4:1 at $\nabla\rho > 20\%$ global max gradient
Inviscid flow throughout

$\nabla\rho$
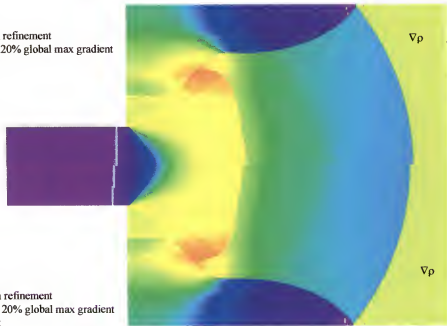
Case 2, Mach 1.88
Time = .000180000 sec
.5 mm x .5 mm grid with refinement
Refinement: 4:1 at $\nabla\rho > 20\%$ global max gradient
Inviscid flow throughout

$\nabla\rho$

Figure 5.29 Direct comparison DRAMR computational data for Case 2 at t=180 μS for Mach 1.908 on top and Mach 1.88 on bottom

Another examination of the shock front misalignment is shown in Figure 5.30. Here, the original Case 2 data (on the 1 mm x 1 mm grid, showing pressure gradient) at 169 µs is compared with the Case 2 data at 180 µs. Here there is agreement with the shock front location and better agreement with the location of the barrel shock as well. However, as indicated in Figure 5.30, there is disagreement in the location of the reflected shock front. The brackets are identical in size and clearly show that the wall shock for the computational data has not reflected and traveled to a comparable location for the experimental data. Interestingly, however, if we compare the location of the reflected shock in Figure 5.23, there is much better agreement.

Case 2, Mach 1.908
Time = .000168888 sec
1 mm x 1 mm grid with refinement
Refinement: 4:1 at $\nabla\rho$ > 20% global max gradient
Inviscid flow throughout

$\nabla\rho$
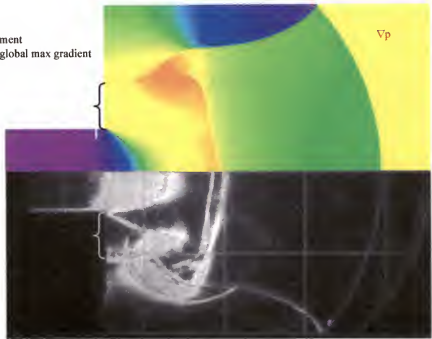
Figure 5.30 Direct comparison DRAMR computational data for Case 2 at t=169 µS for Mach 1.908 on top and Case 2 at t=180 µS on bottom

Therefore, there is agreement in the initial location of the shock front (see Figures 5.21 and 5.25b), there is good agreement in the location of the reflected shock front (see Figure 5.23), and the vortex trajectory correlates well as seen in Figures 5.26b and 5.28.

This clearly indicates that the initial structure of the expanding shock wave and expansion of the core flow (i.e., the formation and propagation of the vortices) have been correctly modeled by the DRAMR code. The good agreement in the complete flow structure of Case 1 would also indicate the DRAMR core is capable of modeling this geometry. The mismatch in shock front and barrel shock location of Case 2 is still unclear.

5.2.2.4 Comparison with Two-Dimensional Axisymmetric Numerical Data

One-to-one comparisons of the DRAMR data to the two-dimensional axisymmetric data of Chang and Kim (1995) and Jiang et al. (1997) similar to the comparisons shown in Figures 5.13 and 5.14 are shown in Figures 5.31 and 5.32. The Case 1 comparisons are similar to the experimental data given the excellent agreement in that data and the DRAMR data. The comparison to the Case 2 data is good in this instance as the shock has only begun to expand. Again, this data shows good agreement in the initial development of the flowfield except for the x-location of the vortex.

5.2.2.5 Viscous vs. Inviscid Data

In an attempt to see if viscous effects are playing a significant role in the shock front mismatch between the numerical and experimental data, the DRAMR solution was run with a fully viscous flow solver. However, only viscous effects in the field were studied. That is, there were no wall shear or turbulence modeling. Only the fully laminar Navier-Stokes equations were solved in the field. The comparison of this solution for Case 2 (Mach 1.908) to the inviscid solution is given in Figure 5.33. Here it is seen a nearly identical solution at 180 μs. This result indicates that viscous effects in the field are not influencing the shock location.
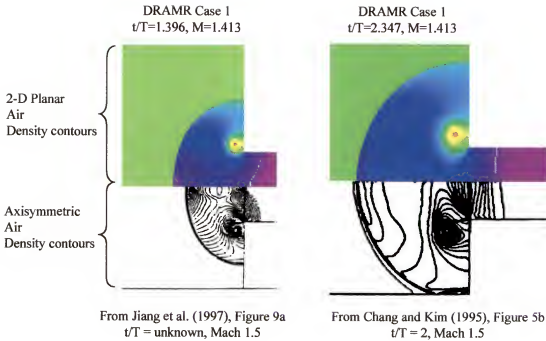
Figure 5.31 Direct comparison between the DRAMR data (Case 1, Mach 1.413) and data of Jiang et al. (1997) and Chang and Kim (1995)
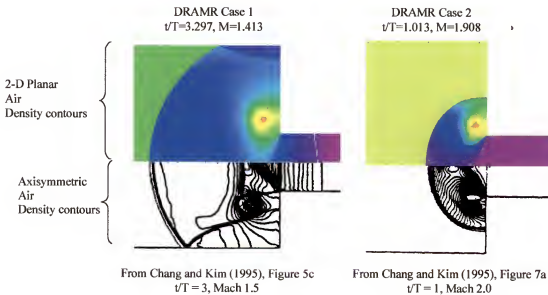
Figure 5.32 Direct comparison between the DRAMR data (Case 1, Mach 1.413, and Case 2, Mach 1.908) and data of Chang and Kim (1995)

Case 2, Mach 1.908
Time = .000180000 sec
.5 mm x .5 mm grid with refinement
Refinement: 4:1 at $\nabla\rho$ > 20% global max gradient
Laminar viscous flow in field
Re=25.9/m
No turbulence modeling
No wall shear

$\nabla\rho$

Case 2, Mach 1.908
Time = .000180000 sec
.5 mm x .5 mm grid with refinement
Refinement: 4:1 at $\nabla\rho$ > 20% global max gradient
Inviscid flow throughout

$\nabla\rho$

Figure 5.33 Comparison of DRAMR computational data for Case 2, Mach 1.908, at t=180 µS for viscous field solution (top) and inviscid solution (bottom)

5.2.2.6 Pressure Data

The DRAMR data computed for this effort provides the unsteady wall pressure along the expansion chamber for comparison to the experimental data. This will be extremely useful in analysis of the data over just the visualization data as this provides quantitative data for comparison.

The pressure data provided from the DRAMR data is for the Mach 2.0 case with the 1 mm x 1 mm grid. The data provided is the pressure along the entire bounding wall of the shock tube expansion device. In order to compare it to the pressure transducer data, the pressure value at the transducer location needs to be tracked in time. In addition, the pressure variation across the transducer is accounted for during the expansion process as outlined in Section 2.2.5.

the pressure variation across the transducer is accounted for during the expansion process as outlined in Section 2.2.5.

Figure 5.34 presents a typical pressure trace produced by the DRAMR code. Here, the pressure along the entire horizontal bounding wall is presented. The location of the pressure transducer is indicated as well as the values of pressure at the beginning, middle, and end of the transducer. These values will be used in equation 2.4 to determine the pressure indicated by the transducer. The comparison between the experimental and numerical (DRAMR) pressure data is shown in Figure 5.35. Here it is seen that the DRAMR data over-predicts the magnitude of the pressure. Again, going back to the argument of the previous section, this indicates a stronger shock for the DRAMR data that again accounts for the shock outrunning the experimental data.

5.2.3 Discussion of Numerical vs. Experimental Results

The mismatch in shock front location for Case 2 between the experimental data and DRAMR data is of concern. Errors in initial conditions have been ruled out and the fact that such good agreement is seen for Case 1 only increases the concern.

If it is assumed that the DRAMR data is "correct", that is, if it is assumed that the solution is accurate given its limitations, then comparing to the experimental data in the hopes of identifying experimental shortcomings may shed light on this disagreement. The DRAMR data is exactly two-dimensional. The experimental setup attempts to produce two-dimensional data. However, recall from Section 2.1.5 that at the entrance to the chamber, the circular shock tube transitions to a square cross section over 150 mm. Invariably, this expansion will cause gradients in the flowfield in the transverse direction. It was hoped in the initial design that and transverse gradients would diminish in the

following 38 mm where a constant square cross section exists. However, as the incident Mach number increases, there is an increase in the magnitude of these transverse gradients. It logically follows that at higher Mach numbers, the effect of the entrance transition will have greater effects on the incoming flowfield.
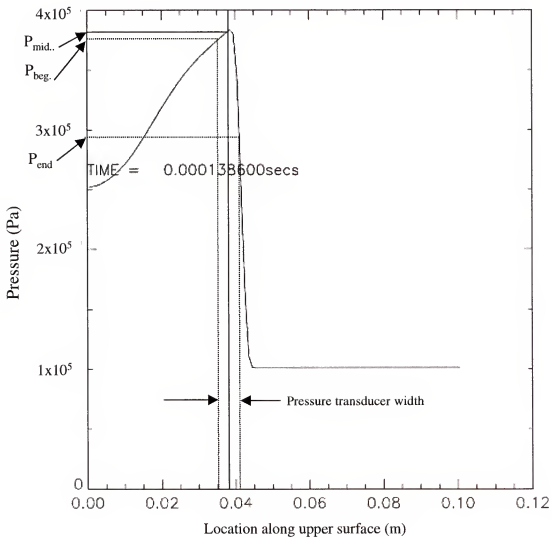
Figure 5.34 Typical pressure vs. distance trace along wall of expansion chamber for DRAMR data for Case 2 (Mach 1.908)
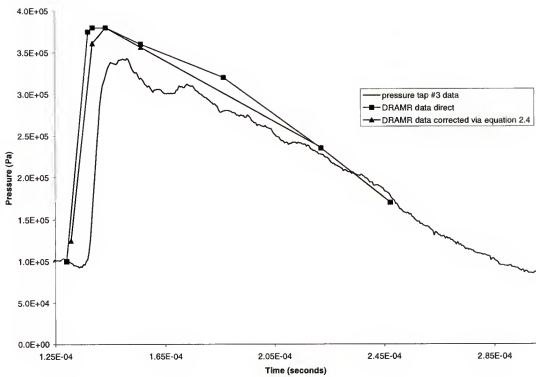
Figure 5.35 Comparison of experimental pressure data to results of the DRAMR code for Case 2 (Mach 1.908)

Figure 5.36 shows the decrease in shock strength for the Case 2 DRAMR data along with the current data and theory as originally presented in Figure 5.8b. Here it is seen that the decrease in shock strength for the DRAMR data falls off greater than for the cylindrical shock expansion. This is to be expected as it has already been shown that the shock strength varies along the shock front. It is interesting though that the DRAMR shock strength closely matches a spherical shock expansion initially and actually matches the experimental shock strength at $x/D=3.0$. It is clearly seen the extreme loss in shock strength for Case 2 which indicates increased three-dimensionality in the flowfield which is analogous to the spherical vs. cylindrical theoretical expansion. This sudden loss in shock strength is not seen for Case 1 (see Figure 5.8a)

Closer examination of the experimental data helps substantiate this argument. In Figure 5.24, there are seen two distinct density gradients in the region of the barrel shock. The front closest to the chamber entrance is the barrel shock as it is distinct and sharp. The other density gradient is smeared and indicates a sharp increase or decrease in density with this visualization system. Similar "double" density gradients are seen in Figure 4.14e and 4.14f that is also a Mach 2 expansion. Note that in these two time-accurate images there is a separation of the gradients in time.
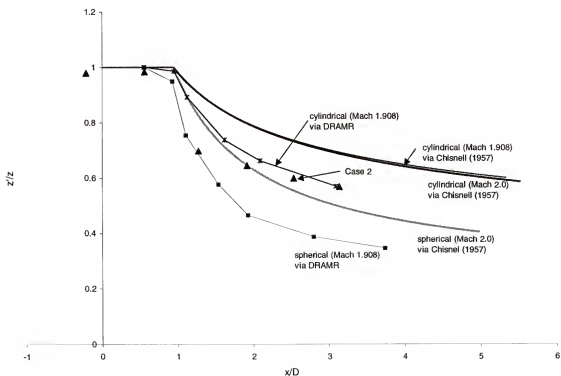
Figure 5.36 Shock strength decay vs. location for cylindrical and spherical shocks according to the theory of Chisnell, Case 2 DRAMR data, and Case 2 experimental data

5.2.3.1 Two Dimensionality

The experimental data was presented in Chapter 4 and discussed in detail in Section 5.1. Here, detailed schematics of the evolving flow structure were presented.

Precise measurements of the shock location and vortex location were measured. A detailed evaluation of the data was performed and compared with prior data.

An underlying design objective of this device was for the formation of a two-dimensional, planar shock expansion. The reason was that it would be easy to visualize the flowfield without the need for special optical devices. Another reason is that direct comparisons to numerical data would be simpler as a two-dimensional grid would be required, greatly saving time and resources. It is therefore important to show that the current data is in fact two-dimensional.

There is no evidence of three-dimensionality in the optical data. That is, the shocks entering the chamber prior to expansion are seen as planar. The theory of Chisnell indicates that early on in the expansion, that is up to the formation of the critical shock and half a diameter travel later, the spherical and cylindrical shocks will expand at about the same rate. This was verified in the comparison of the current data to that of Chang and Kim (1995).

A comparison of vortex trajectory of the current data to both the two-dimensional axisymmetric data of Chang and Kim (1995) and Jiang et al. (1997) and the three-dimensional square data of Jiang et al. (1999) is shown in Figure 5.12. Here there were distinct variations in the path of the trajectory for the two-dimensional planar, two-dimensional axisymmetric, and the three-dimensional data.

Finally, there were marked differences in the flow structure for the current data and for the data of Chang and Kim (1995) and Jiang et al. (1997) that were highlighted by Figures 5.13 and 5.14. In these comparisons, there were similarities in the flow structure, however, the locations of the structure varied significantly between the two cases.

The DRAMR data provided by Edwards (1999) are compared to the current data and shown in Figures 5.19 through 5.36. For the case where subsonic expansion followed the weak expanding shock (Mach 1.413) there is almost exact agreement between shock structure and vortex location. The agreement of the DRAMR data to the current data for the supersonic expansion of Case 2 (Mach 1.908) is not as good. The difference seems to stem from the axial shock location. This agreement is highlighted by the fact that there is excellent agreement in the early stages. However, in the later stages the agreement is poor and it is suggested that the reason for this is that the higher entrance Mach number is causing increased gradients in the flow in the transverse direction. These gradients reduce the intensity of the shock as it expands in much the same way a spherical shock decays faster that a comparable cylindrical shock.

So the culmination of all these arguments leads to the conclusion that the data is indeed two-dimensional for the Case 1 data. However, the data of Case 2 is suspect in its two-dimensionality. The Case 1 data can confidently be compared and studied against corresponding numerical data while additional studies into the Case 2 data are necessary.

5.2.3.2 Shock Vortex Interaction

The interaction of a shock and a vortex has been the subject of many studies (Ellzey et al., 1995, Guichard et al., 1995, and Kao et al., 1996). The current data is ideally suited to provide additional insight into those studies. The shock/vortex interaction is a fundamental topic for study in modeling fluid dynamics. Of the previous studies on shock vortex interaction, Ellzey et al. (1995) studied the interaction of a plane vortex and shock wave each having variations in strength. This numerical study drew conclusions about the interaction of the two fluid dynamic structures based upon the

relative strength and weakness of each. For instance, if the vortex is weak relative to the shock, then there is no significant distortion of the front. A strong vortex, however, distorts both a strong and weak shock. A weak shock interacting with a strong vortex causes the shock to distort and simply split. A strong shock and strong vortex interaction, however, causes the transmitted shock to split and form a Mach stem.

Looking at the current data we see that in the data for both Case 1 (Mach 1.413) and Case 2 (Mach 1.908) there is severe distortion and then a sudden splitting of the shock. The DRAMR data for Case 1 is not carried forward in time enough to study the interaction but it is clearly seen in the data of Case 2. Figure 5.24 clearly shows the distortion of the shock as it passes through the vortex and is matched quite well with the experimental data. This shows that the inviscid formation of the vortex by the baroclinic torque mechanism is sufficient as well as the code's ability to capture the shock front.

Based upon these observations and the work of Ellzey et al. (1995) it is clear that a strong vortex is produced in the current data and that the reflected shock is characterized as "weak". Ellzey refers to a shock of Mach 1.05 as weak and 1.5 as strong and goes on to clarify that a strong vortex/weak shock interaction requires that the maximum vortex velocity be much greater than the fluid velocity behind the shock. Recall that the wall Mach numbers measured in the current data range from Mach 1.1-1.3. This agrees with the assessment that the reflected shock is characterized as weak.

5.2.3.3 Viscous Dissipation

To investigate the role of viscous dissipation in the flowfield, a post-processing of the DRAMR data was performed. Fluid dynamic quantities not directly solved for by the code can be calculated based upon the numerical solution of the flowfield. This post

processing is easily performed with the aid of the commercial flow visualization software Tecplot®. This investigation is done mainly as a diagnosis effort to gain more insight about the flow structure. These quantities calculated here might not be quantitatively accurate. Based upon the results of Section 5.2.2.3, however, it was seen that the viscous flow solution does not make a noticeable impact on the inviscid solution. It is believed that the results presented here are meaningful nonetheless.

Recall the equation for viscous dissipation as given by equation 1.11. The quantities found in this equation were determined based upon the numerical flowfield computed by DRAMR for Case 2 at 180 μs. Figure 5.37 depicts contour lines of vorticity within the flowfield as given by equation 1.10 and the density variations via shading. Here it is seen that at this instance in the flowfield development, the vorticity is mainly confined to the shear layer roll-up from the 90° corner, the region around the vortex, and the regions where there is curvature in the shock fronts. The dilatation as given by equation 1.9 is shown in Figure 5.38 in a fashion similar to the vorticity term. Here it is seen that the dilatation is mainly confined to the regions around the shock waves, the shock tube exit, and the shear layer formed at the expansion corner.
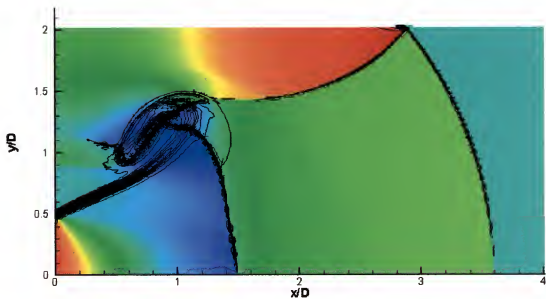
Figure 5.37 Vorticity contours (lines) and density variation (shade) for DRAMR computation of Case 2 at 180 μs
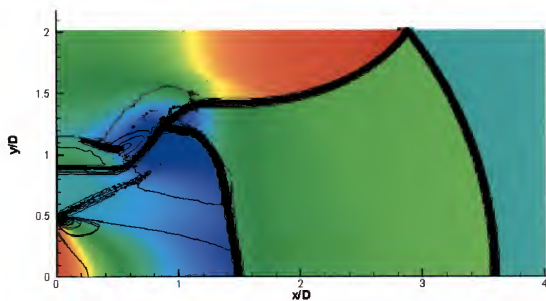
Figure 5.38 Dilatation contours (lines) and density variation (shade) for DRAMR computation of Case 2 at 180 μs

The computation of dissipation rate (equation 1.11) is presented in Figures 5.39 and 5.40. Figure 5.39 shows the two-dimensional dissipation rate contours similar to Figures 5.37 and 5.38 while Figure 5.40 presents that same information in a three-dimensional grid for clarity. Note that for Figure 5.39, the absolute value of TKE is plotted. Here it is seen that the majority of dissipation of TKE is confined to the shock fronts, the curve in the barrel shock, the region where the reflected shock interacts with the vortex, and the shear layer formed from the expansion corner.

Figure 5.41 splits the components of the dissipation rate of TKE into the solenoidal and dilatational components. As seen here, the vorticity, or solenoidal, component of the dissipation rate is predominant in the shear layer at the expansion corner. The dilatational component is confined mainly to the shock fronts, especially at the curvature of the barrel shock.
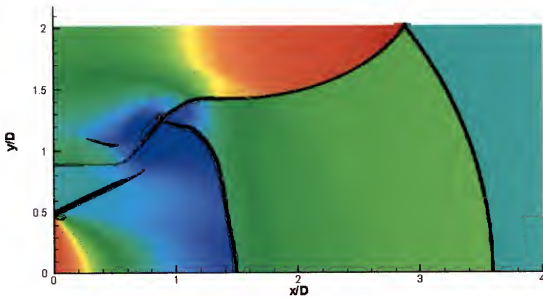
Figure 5.39 Rate of dissipation of TKE contours (lines) and density variation (shade) for DRAMR computation of Case 2 at 180 μs (2-D contour)

This indicates that there is little dissipation within the flow structure save for the areas around the shock and expansion corner. Vorticity is the main contributor to dissipation through the formation of the shear layer and dilatation contributes to the dissipation mainly through the shock fronts. This is especially true in the highly curved barrel shock region. However, from Figure 5.36 it is clear that there is a sudden decay in shock strength in the current experimental data of Case 2 when the expanding shock front transitions through the critical shock. Whether this mismatch is an error with the experimental device or computations is unclear at this time.
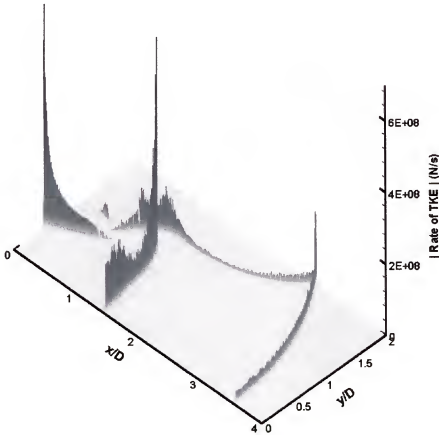
Figure 5.40 Absolute value of rate of dissipation of TKE computed for DRAMR data of Case 2 at 180 μs (3-D contour)

a) Solenoidal contribution to TKE

b) Dilatational contribution to TKE
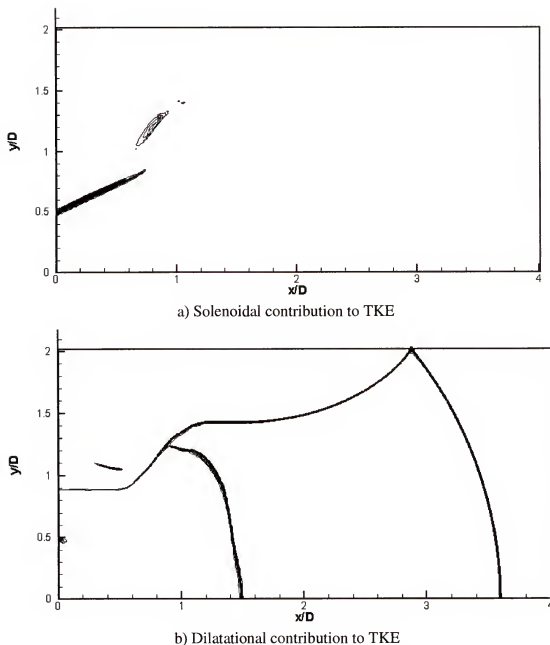
Figure 5.41 Solenoidal and dilatational components of the dissipation of turbulent kinetic energy (TKE) for the DRAMR Case 2 at 180 μs

5.3 Summary

A quantitative comparison of the time-accurate flowfield visualization data and pressure data was performed with existing numerical data. The numerical data used for

comparison included both a two-dimensional axisymmetric expansion and new, two-dimensional planar numerical data produced specific to the shock tube expansion device geometry and experimental conditions.

Comparison with existing numerical data where a circular geometry is used showed good correlation is observed with the flow structure and lateral expansion of the vortex core. However, correlation with longitudinal vortex core location was poor. This may be attributable to the fact the current data has a square shock tube exit while the previous numerical data has a round shock tube exit. Similar flow structure is observed with reflected shock and vortex interaction. Table 5.3 summarizes the comparison between the current experimental data and the numerical data of Chang and Kim (1995), Jiang et al. (1997), Jiang et al. (1999), and the DRAMR data of Edwards (1999).

Comparison to the new numerical data specific to the geometry showed favorable agreement for the subsonic flow expansion (Case 1) but was not so good for the supersonic expansion (Case 2). A grid refinement study indicated that the numerical grid with refinement is adequate. Further analysis of the experimental data indicates that perhaps excessive transverse gradients, as a result of the chamber inlet geometry, are causing the mismatch in Case 2 data. These transverse gradients are greater with increased inlet Mach number which helps explain the correlation at Mach 1.413 and not at Mach 1.908. Excessive shock strength decay is seen in the latter data set that is computed via DRAMR

Table 5.3 Summary table of comparison of current data to numerical data

	Mach number	Geometry	expansion ratio	Axial shock location	lateral shock location	Vortex location
Case 1	1.413	2-D planar	4:1			
Chang and Kim (1995)	1.500	2-D axisymmetric	3:1	good initially, then poor	excellent	marginal
Jiang et al. (1997)	1.500	2-D axisymmetric	3:1 and 2:1	poor due to timing errors	NA	marginal
Jiang, Onodera, and Takayama (1999)	1.500	square, 2-D axisymmetric	none	NA	NA	see comments
DRAMR	1.413	2-D planar	4:1	excellent	excellent	excellent
Case 2	1.908	2-D planar	4:1			
Chang and Kim (1995)	2.000	2-D axisymmetric	3:1	good initially, then poor	excellent	good
DRAMR	1.908	2-D planar	4:1	good initially, then poor	excellent	very good

A post processing of the DRAMR data yielded an estimation of the rate of dissipation of turbulent kinetic energy (TKE). This data showed that the solenoidal dissipation is centered mainly in the shear lay that forms at the exit of the shock tube while the dilatational dissipation is concentrated mainly along the shock fronts. The dilatational dissipation is strongest where there is curvature of the shock front. For the case studied, this is mainly in the barrel shock that forms due to the supersonic induced flowfield exiting the shock tube.

CHAPTER 6
CONCLUSIONS AND FUTURE DIRECTION

The experimental data has been presented in the preceding chapters as well as its comparison to numerical simulations. These numerical simulations include previously reported data on two-dimensional axisymmetric shock expansions and new two-dimensional planar data specific to the experimental trials. The first part of this chapter will present conclusions that are drawn about the flow structure based upon the experimental results and comparisons to the numerical data. Finally, the future direction this research should take will be presented.

6.1 Conclusions

A shock tube expansion device has been designed and constructed in an attempt to produce two-dimensional planar shock waves that exit into a confined chamber. This shock tube is 25 millimeters in diameter and approximately 1 meter in length. The shock tube exits into a "shock expansion chamber." The entrance to this chamber is 25 millimeters in diameter and the cross section transitions to 25 millimeters square over 100 millimeters. The square cross-section continues of for 38 millimeters. While in this section, the side walls are optically clear. This 25 millimeter square cross section then suddenly expands around a 90° corner to 25 millimeters by 100 millimeters where again the sides of the chamber that do not expand are optically clear.

Time accurate, circular cut-off, Schlieren images were captured of the shock wave undergoing the sudden expansion for shocks of nominal Mach numbers of 1.5, 2.0, and 3.0 in dry air. These time-accurate images are gathered via digital camera. The circular cut-off Schlieren technique has been shown to be superior to a traditional knife-edge Schlieren system in that density gradients can be observed in all direction. This is especially advantageous in the current situation, as there is no predominant flow direction. The imagery system produces excellent visualization of the flowfield structure and development. Features of the flowfield such as vortices, reflected shock waves, barrel shocks, etc. are easily tracked with this system.

Excellent shock/vortex interaction data were gathered in this work. The incident shock wave expands around the 90° corner when it enters the expansion chamber. The shock front begins to curve and the "wall shock" wave propagates along the chamber walls until reflected by the confining upper and lower walls of the chamber. At this same time, the flowfield that is following the shock front expands at the chamber entrance. A shear layer and vortex form here. This vortex is convected out into the flowfield essentially along a straight line. The reflected shock then encounters this vortex and interacts with it. There is seen diffraction of the shock front as it encounters the shock wave and then the shock wave is split. This splitting of the shock wave is indicative of a strong vortex and weak shock interaction. This data provides a unique set of two-dimensional planar shock fronts interacting with a vortex. The current data clearly shows the time-accurate evolution, distortion, and splitting of the shock as it interacts with a vortex.

Analysis of the time-accurate flowfield data of a shock wave that is allowed to suddenly expand around a 90° corner shows that the shock remains planar in the core until it reaches the "critical" shock stage. The critical shock is that shock that first becomes non-planar. Measurements from the data show that the shock that propagates along the expansion wall (i.e., the wall shock) is much weaker that the incident shock front. This gives rise to a curved, expanding shock that varies in strength along the front. Analysis showed that this shock is not cylindrical and that it decays faster than a cylindrical shock of equal magnitude that expands equally in all directions.

Two experimental trials that were studied extensively in this work were for incident shocks of Mach 1.413 (Case 1) and 1.908 (Case 2). The resultant flow structure for these two cases were compared. The Case 1 flowfield structure has a subsonic induced flowfield from the incident shock. The Case 2 flowfield is supersonic. The data presented in this effort compare the flow structure for these two induced flowfields. The Case 2 flowfield shows a distinct barrel shock formation and convection of the vortices into the chamber is more pronounced.

The time-accurate experimental flowfield data was then compared to existing two-dimensional axisymmetric and two-dimensional planar numerical data. The current Case 1 experimental data was produced with a Mach 1.413 shock that undergoes a two-dimensional expansion from a 25 mm square exit. The confining chamber has a 4:1 ratio. The Case 2 data is produced with a Mach 1.908 shock. The comparison of this data to numerical two-dimensional axisymmetric data produced from a circular exit into a circular confining chamber of 3:1 ratio shows that early on in the expansion process (i.e., within the first two diameters) the flowfield structure evolves very similarly. This aspect

was predicted by analysis and confirmed herein. This comparison also indicates that the trajectory of the vortex formed at the expansion corner is convected into the flowfield faster in the two-dimensional axisymmetric case. This is confirmed both experimentally and with comparison of the planar data as well. However, the lateral propagation of the vortices (i.e., in the y-direction) actually correlates very well for the axisymmetric and planar geometry.

Two-dimensional planar data was computed with DRAMR for the exact conditions of Case 1 and Case 2. Direct comparisons of the Case 1 experimental data showed excellent agreement of the flow structure; both in shock location and vortex position. However, the comparison with Case 2 data was not as good. For this case, there was agreement early on similar to the agreement of the axisymmetric data. However, as time progressed it was evident the computational shock was remaining stronger and, hence, propagating faster than the experimental shock. Variations of initial conditions and investigations with fully laminar viscous simulations (with no wall shear) showed no significant change over the baseline (inviscid, Mach 1.908) solution.

Closer examination of the experimental data showed evidence of three-dimensional effects in the flowfield. That is, there were two distinct density gradients in the location of the barrel shock where only one is expected. The chamber entrance geometry requires that the cross section undergoes a transformation. It is suspected that the increased Mach number is causing increases in transverse gradients within the flow at the entrance. Analysis of the experimental data shows a severe loss of shock strength immediately after the critical shock. The computational shock decreases in strength more

gradual from the critical shock. This result questions the validity of two-dimensionality for the Case 2 data.

Finally, an estimation of the rate of dissipation of turbulent kinetic energy (TKE) was undertaken with the data from the Case 2 DRAMR solution. The flowfield was studied after it evolved for 180 microseconds. At this instant, the shock front has undergone reflection via the confining walls and has begun interaction with the vortices formed from the expansion corner. Discrete calculations of the solenoildal and dilatational terms of the dissipation of TKE show that the solenoidal dissipation is confined to the region of the shear layer that forms from the expansion corner. The dilatational dissipation is concentrated mainly at the curvature of the incident, reflected, and barrel shock fronts.

6.2 Future Direction

Two natural next steps in this study would be to redesign the shock tube to use a square cross section shock tube. Earlier discussions indicated that a round shock tube is most efficient in strength and quality. However, the desire to produce a two-dimensional planar shock wave may require this step. The second would be to simulate the three-dimensional flowfield inclusive of the entrance geometry where the transverse gradients can be studied to assess their effect on the shock expansion properties. These two actions would help understand the mismatch seen in the Case 2 data.

It is also desirable to perform the numerical simulations with commmpressible turbulence models to see how it affects the data. While it is clear that the major features of the flowfield are captured by the two-dimensional inviscid code, the interaction of the

flowfield within the core, the formation of vortices, interactions with shock waves, etc., are all strongly affected by viscous effects.

Experimentally, additional types of imagery should be investigated. For instance, an interferometric system applied to the flowfield may yield other insights. Especially since this type of system is becoming more and more common. Also, a simple shadowgraph of the expanding flowfield would be advantageous, as some of the subtle shock structure is lost in the circular cut-off Schlieren system.

Finally, variations of test gas should be pursued to understand the changes in flow structure for these gases. Varying the initial pressure should also be included to better understand the influence of the pressure field on the data.

APPENDIX
THE DRAMR CODING ENVIRONMENT

The DRAMR (DRA Adaptive Mesh Refinement) coding environment is based on the structured hierarchical mesh refinement algorithm proposed by Berger (1982) and Quirk (1991). DRAMR was originally created to allow rapid and efficient solution of arbitrary series of partial differential equations (either in two-dimensions or modified to account for axial symmetry). The only stricture imposed on the numerical solvers is that the scheme must by cell centered. Separation of the mechanics of integration and mesh adaptation facilitates rapid incorporation of solvers for development, evaluation and exploitation. It is often the case that a single numerical method cannot accurately or efficiently resolve all of the features, which exist in the solution of a non-linear system. To address problems inherent with specific algorithms, it is common to apply 'fixes' to overcome (either locally or globally) the inapplicability of an algorithm to the solution of a problem. These 'fixes' can reduce the quality of the solution in regions where the unmodified algorithm would be expected to work well. An alternative (the philosophy adopted within DRAMR) is to apply a range of interchangeable algorithms to suit local solution features, e.g. for solving fluid flows around arbitrary configurations the Roe (1981), WAF (Toro, 1989), exact, Godunov, and hybrid solvers are available.

Since DRAMR was coded for solving arbitrary systems of partial differential equations, no major modifications are required to either the adaptation or integration in

order to add additional equations. In this manner DRAMR is ripe for extension to compute multi-species flows, combustion, real gas effects, etc:

DRAMR has predominantly been used to solve the Navier-Stokes (and Euler) equations to predict fluid flows around specific geometries, although there is no reason why, with suitable sets of equations and boundary conditions, the code should not be used to solve any discretizable problems. The use of hierarchical grid refinement provides optimized grid point placement, in that the code can be configured to detect regions of high spatial sensitivity (typically relatively large computational spatial gradients e.g. density, pressure, shear stress, etc.) and to undertake adaptation to provide enhanced spatial resolution. Due to the dynamic, time accurate nature of the adaptation, DRAMR is not limited to providing solutions to aerodynamically static flowfields, but can accurately track unsteady time dependant phenomena such as shock wave propagation, etc. Determination of precisely where to adapt is undertaken at every time step and hence the grid is seen to 'follow' flow structures as the solution progresses, e.g. the motion of a shock wave can be seen as a moving refinement in the computational grid.

DRAMR has subsequently been extended to accommodate arbitrary mesh importation, turbulence modeling, which employs algebraic and two-equation turbulence models (Zhang, 1996 and Roper, 1999), and the ability to model flow around moving surfaces using adaptation to capture body surfaces to within an arbitrary precision (Edwards and Roper, 1999) (e.g. pitching wing sections, ablating surfaces, flap deployment, multiple body flows, etc). Extensions into three dimensions are nearing completion.

Flow visualization and post processing is via custom coded X windows based routines or via external graphics packages, for example PvWave® and Fieldview®, all of which can be semi- or fully-automated.

The flowfields within the shock tube expansion device contain shock-shock interactions to provide locally very high temperatures and pressures. For all of the DRAMR computations performed for this work, the code was used in operator split mode with a Roe based Riemann solver (Roe, 1981) including the entropy fix of Harten (1994). For these computations refinement was flagged on the basis of density gradients (in excess of 20% of global maximum gradient), with refinement patches of 4x4.

The computational domain for the shock tube expansion device is given in Figure A.1. Here, the solution takes advantage of axial symmetry. The shock is located within the entrance tube to match the experimental data. An example of the grid adaption is presented in Figure A.2.
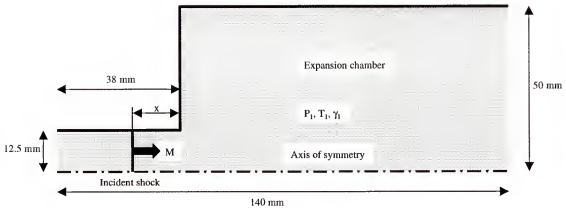

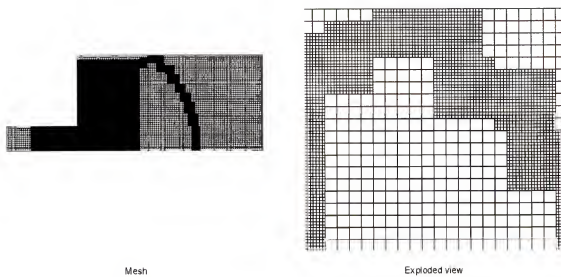Figure A.1 Computational domain of the DRAMR flow solutions

Mesh   Exploded view

Figure A.2 Example of grid adaptation for the DRAMR flow solutions

REFERENCES

Abe A and Takayama K (1990) Numerical simulation and density measurement of a shock wave discharged from the open end of a shock tube. JSME International Journal 33:216

Anderson CS (1995) Fringe visibility, irradiance, and accuracy in common path interferometers for visualization of phase disturbances. Applied Optics 34:7474-7485

Anderson RC and Taylor MW (1982) Phase constant flow visualization. Applied Optics 21:528:536

Anderson JD Jr (1990) Modern compressible flow. McGraw Hill Inc., New York

Anderson RC, Milton JE, and Anderson CS (1995) Common path interferometry for flow visualization: a review. AIAA paper 95-0481

Berger MJ (1982) Adaptive mesh refinement for hyperbolic partial differential equations. PhD Dissertation, Stanford University, Stanford

Bradley JN (1962) Shock waves in chemistry and physics. John Wiley and Sons Inc., New York

Chang KS and Kim JK (1995) Numerical investigation of inviscid shock wave dynamics in an expansion tube. Shock Waves 5:33

Chatterjee A (1999) Shock wave deformation in shock-vortex interactions. Shock Waves 9:95-105

Chisnell RF (1957) The motion of a shock wave in a channel, with applications to cylindrical and spherical shock waves. J Fluid Mechanics 2:286-298

Dillmann A, Wetzel T, and Soeller C (1998) Interferometric measurement and tomography of the density field of supersonic jets. Experiments in Fluids 25:375-387

Dosanjh DA and Weeks TM (1965) Interaction of a starting vortex as well as a vortex sheet with a traveling shock wave. AIAA J 3:216-223

Edwards JA (1999) private communication

Edwards JA and Roper JJ (1999) Adaptive moving body flow computations. AIAA paper 99-0393

Ellzey JL, Henneke MR, Picone JM, and Oran ES (1995) The interaction of a shock with a vortex: shock distortion and the production of acoustic waves. Phys Fluids 7:172-184

Fuller PWW (1997) Flow Visualization. In: Ray S (ed) High speed photography and photonics, Focal Press, Oxford, UK, pp 254-280

Gaydon AG, and Hurle IR (1963) The shock tube in high-temperature chemical physics. Reinhold Publishing Co., New York

Guichard L, Vervisch L, and Domingo P (1995) Two-dimensional weak shock-vortex interaction in a mixing zone. AIAA J 33:1797-1802

Harten A (1994) Adaptive multiresolution schemes for shock computations. J Computational Physics, 115:319-338

Holder DW and North RJ (1963) Schlieren methods. Notes on applied science 31. National Physical Laboratory, London

Honour J (1994) A new high speed electronic mulit-framing camera, Proc SPIE 2513:28-34

Jiang Z, Onodera O, and Takayama K (1999) Evolution of shock waves and the primary vortex loop discharged from a square cross-section tube. Shock Waves 9:1-10

Jiang Z, Takayama K, Babinsky H, and Meguro T (1997) Transient shock wave flows in tubes with a sudden change in cross section. Shock Waves 7:151-162

Jones DA, Sichel M, and Oran ES, (1995) Reignition of detonations by reflected shocks. Shock Waves 5:47-57

Kao CT, von Ellenrieder K, MacCormack RW, and Bershader D (1996) Physical analysis of the two-dimensional compressible vortex-shock interaction. AIAA paper 96-0044

Kleine H and Grönig H (1991) Color Schlieren methods in shock wave research. Shock Waves 1:51-63

Krishnamurty VS (1996) Effect of compressibility on the turbulence structure and its modeling. PhD Dissertation, University of Florida, Gainesville

Lee, JHS (1997) Shock vortex interaction: its role in compressible turbulence and detonation structure. Proceedings of the Second International Workshop of Shock Wave/Vortex Interaction, Sendai, pp 15-30

Lehr HF (1972) Experiments on shock induced combustion. Astronautica Acta 17:589-597

Liu JC, Liou JJ, Sichel M, Kauffman CW, and Nicholls JA (1986) Diffraction and transmission of a detonation layer into a bounding explosive layer. 21st Symposium (International) on Combustion, The Combustion Institute, Pittsburgh, pp 1639-1647

Loomis MP, Holt M, Chapman GT, and Coon M (1991) Applications of dark central ground interferometry. AIAA paper 91-0565

McKenzie RL, Hanson RK, and Eckbreth AC (1992) shedding new light on gas dynamics. Aerospace America 11:20-25

Merzkirch W (1974) Flow visualization. Academic Press, New York

Miyauchi T, Tanahashi M, Sasaki K, and Ozeki T (1995) Vortex flame interaction in diffusion flames. Proceedings of the 8th International Symposium on Transport Phenomena in Combustion, San Francisco

Oran ES, Boris JP, Jones DA, and Sichel M (1993) Ignition in a complex Mach structure. Prog Astro Aero 153:241-252

Pantow EG, Fischer M, and Kratzel Th (1996) Decoupling and recoupling of detonation waves associated with sudden expansion. Shock Waves 6:131

Quirk JJ (1991) An adaptive grid algorithm for computational shock hydrodynamics. PhD Dissertation, Cranfield University, Cranfield, UK

Riley JJ and McMurtry PA (1989) The use of direct numerical simulation in the study of turbulent, chemically-reacting flows. In Turbulent reactive flows. Springer-Verlag, New York

Roe PL (1981) Approximate Riemann solvers, parameter vectors, and difference schemes. J Computational Physics, 43:357-372

Roper JJ (1999) Turbulence modeling in an adaptive hierarchical environment. Defense Evaluation Research Agency report DERA/WSS/WS4/TR990403

Sarkar S, Erlebacher G, Hussaina MY, and Kreiss HO (1991) The analysis and modeling of dilatational terms in compressible turbulence. J Fluid Mechanics 227:473-493

Shafer HJ (1949) Physical optic analysis of image quality in Schlieren photography. J SMPE 53:524-544

Shyy W and Krishnamurty V (1997) Compressibility effect in modeling complex turbulent flows. Progress in Aerospace Sciences 33:587-645

Shyy W, Thakur S, Ouyang H, Liu J, and Blosch E, (1998) Computational techniques for complex transport phenomena. Cambridge University Press, Cambridge, England

Skews BW (1967a) The shape of a diffracting shock wave. J Fluid Mechanics 29:297-304

Skews BW (1967b) The perturbed region behind a diffracting shock wave. J Fluid Mechanics 29:705-719

Sloan SA and Nettleton MA (1975) A model for the axial decay of a shock wave in a large abrupt area change. J Fluid Mechanics 71:769-784

Sloan SA and Nettleton MA (1978) A model for the decay of a shock wave in a large abrupt area change. J Fluid Mechanics 88:259-272

Smartt RN and Steel WH (1974) Theory and application of point-diffraction interferometers. Proc ICO Conf Opt Methods in Sci and Ind Meas, Tokyo, Japan

Speak GS and Walters DJ (1950) Optical considerations and limitations of the Schlieren method. ARC No 13066

Stolzenburg WA (1965) The double knife-edge technique for improved Schlieren sensitivity in low-density hypersonic aerodynamic testing. J SMPTE 74:654-659

Sun M and Takayama K (1997) The formation of a secondary shock wave behind a shock wave diffracting at a convex corner. Shock Waves 7:287-295

Taylor HG and Waldram JM, (1933) Improvements in the Schlieren method. J Sc Inst 10:378-389

Teodorczyk A, Lee JHS, and Knystautas R (1989) Propagation mechanism of quasi-detonations. In 22nd Symposium (International) on Combustion, The Combustion Institute, Pittsburgh, pp 1723-1731

Toepler, A. (1866) Beobachtungen nach einer neuer optischen methode. Poggendorf. Ann Phys Chem 127:556

Toro EF (1989) TVD regions for the weighted average flux (WAF) method as applied to model hyperbolic conservation law. Cranfield University, UK, report COA-8907

Yu Q and Grönig H (1996) Shock waves from an open-ended shock tube with different shapes. Shock Waves 6:249-258

Valentino M, Kauffman CW, and Sichel M (1998) Experimental study of the mixing of reactive gases at their interface behind a shock wave. AIAA paper 98-2507

Watanabe M, Abe A, Casey RT, and Takayama K (1991) Holographic interferometric observation of shock wave phenomena. SPIE 1553:418-426

Williams FA (1985) Combustion theory. Second edition, Addison-Wesley, Reading, MA

Whitham GB (1956) A new approach to problems of shock dynamics Part I Two-dimensional problems. J Fluid Mechanics 2:145-171

Winchenbach GL (1997) Aerodynamic testing in a free-flight spark range. United States Air Force Wright Laboratory Technical Report, WL-TR-1997-7006, Eglin AFB, Florida

Yates LA (1992) Images constructed from computed flowfields. AIAA paper 92-4030

Zeman O (1990) Dilatation dissipation: The concept and application in modeling compressible mixing layers. Physics of Fluids A 2: 178-188

Zhang X (1996) Turbulent flow simulation using k-w model. Department of Aeronautics and Astronautics, Southampton University, UK

BIOGRAPHICAL SKETCH

Gregg was born February 2, 1964, in Newark, New Jersey. Gregg grew up in Union, New Jersey, and graduated from Union High School in 1982. Gregg attended the New Jersey Institute of Technology for one year before transferring to Embry-Riddle Aeronautical University, Daytona Beach, Florida where he earned a BS degree in aeronautical engineering in 1986. Upon graduation, Gregg was hired by the Air Force Armament Laboratory at Eglin Air Force Base, Florida, where Gregg worked in the Aerodynamics Branch. Gregg earned an MS degree in aerospace engineering from the University of Florida in 1989. Gregg is married to the former Toni Ann LaRocca of Bayside, New York. Gregg and Toni have three children: Sara, Amanda, and Nicholas.
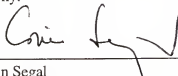
I certify that I have read this study and that in my opinion it conforms to acceptable standards of scholarly presentation and is fully adequate, in scope and quality, as a dissertation for the degree of Doctor of Philosophy.

Wei Shyy, Chairman
Professor of Aerospace Engineering,
Mechanics and Engineering Science

I certify that I have read this study and that in my opinion it conforms to acceptable standards of scholarly presentation and is fully adequate, in scope and quality, as a dissertation for the degree of Doctor of Philosophy.

David Mikolaitis
Associate Professor of Aerospace
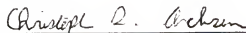Engineering, Mechanics and
Engineering Science

I certify that I have read this study and that in my opinion it conforms to acceptable standards of scholarly presentation and is fully adequate, in scope and quality, as a dissertation for the degree of Doctor of Philosophy.

Corin Segal
Associate Professor of Aerospace
Engineering, Mechanics and
Engineering Science

I certify that I have read this study and that in my opinion it conforms to acceptable standards of scholarly presentation and is fully adequate, in scope and quality, as a dissertation for the degree of Doctor of Philosophy.

Christopher Anderson
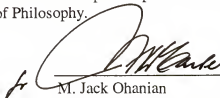Assistant Professor of Electrical and
Computer Engineering

I certify that I have read this study and that in my opinion it conforms to acceptable standards of scholarly presentation and is fully adequate, in scope and quality, as a dissertation for the degree of Doctor of Philosophy.

Davy Belk
Assistant Professor of Aerospace
  Engineering, Mechanics and
  Engineering Science

This dissertation was submitted to the Graduate Faculty of the College of Engineering and to the Graduate School and was accepted as partial fulfillment of the requirements for the degree of Doctor of Philosophy.

December, 1999

M. Jack Ohanian
Dean, College of Engineering

Winfred M. Phillips
Dean, Graduate School